

WAVE-EQUATION MIGRATION IN GENERALIZED  
COORDINATE SYSTEMS

A DISSERTATION  
SUBMITTED TO THE DEPARTMENT OF GEOPHYSICS  
AND THE COMMITTEE ON GRADUATE STUDIES  
OF STANFORD UNIVERSITY  
IN PARTIAL FULFILLMENT OF THE REQUIREMENTS  
FOR THE DEGREE OF  
DOCTOR OF PHILOSOPHY

Jeffrey Shragge

November 2009

© Copyright by Jeffrey Shragge 2009  
All Rights Reserved

I certify that I have read this dissertation and that, in my opinion, it is fully adequate in scope and quality as a dissertation for the degree of Doctor of Philosophy.

---

(Biondo Biondi) Principal Adviser

I certify that I have read this dissertation and that, in my opinion, it is fully adequate in scope and quality as a dissertation for the degree of Doctor of Philosophy.

---

(Jon F. Claerbout)

I certify that I have read this dissertation and that, in my opinion, it is fully adequate in scope and quality as a dissertation for the degree of Doctor of Philosophy.

---

(Jerry Harris)

Approved for the University Committee on Graduate Studies.



# Abstract

Wave-equation migration using one-way wavefield extrapolation operators is commonly used in industry to generate images of complex geologic structure from 3D seismic data. By design, most conventional wave-equation approaches restrict propagation to downward continuation, where wavefields are recursively extrapolated to depth on Cartesian meshes. In practice, this approach is limited in high-angle accuracy and is restricted to down-going waves, which precludes the use of some steep dip and all turning wave components important for imaging targets in such areas as steep salt body flanks.

This thesis discusses a strategy for improving wavefield extrapolation based on extending wavefield propagation to generalized coordinate system geometries that are more conformal to the wavefield propagation direction and permit imaging with turning waves. Wavefield propagation in non-Cartesian coordinates requires properly specifying the Laplacian operator in the governing Helmholtz equation. By employing differential geometry theory, I demonstrate how generalized a Riemannian wavefield extrapolation (RWE) procedure can be developed for any 3D non-orthogonal coordinate system, including those constructed by smoothing ray-based coordinate meshes formed from a suite of traced rays. I present 2D and 3D generalized RWE propagation examples illustrating the improved steep-dip propagation afforded by the coordinate transformation.

One consequence of using non-Cartesian coordinates, though, is that the corresponding 3D extrapolation operators have up to 10 non-stationary coefficients, which can lead to imposing (and limiting) computer memory constraints for realistic 3D

applications. To circumvent this difficulty, I apply the generalized RWE theory to analytic coordinate systems, rather than numerically generated meshes. Analytic coordinates offer the advantage of having straightforward analytic dispersion relationships and easy-to-implement extrapolation operators that add little computational overhead. In particular, I demonstrate that the dispersion relationship for 2D elliptical geometry introduces only an effective velocity model stretch, permitting the use of existing high-order Cartesian extrapolators. The results of elliptical coordinate shot-profile migration tests demonstrate the improvements in steep dip reflector imaging facilitated by the coordinate system transformation approach.

I extend the analytic coordinate system approach to 3D geometries using tilted elliptical-cylindrical (TEC) meshes. I demonstrate that propagation in a TEC coordinate system is equivalent to wavefield extrapolation in elliptically anisotropic media, which is easily handled by existing industry practice. TEC coordinates also allow steep dip propagation in both the inline and cross-line directions by virtue of the associated elliptical and tilting Cartesian geometries. Observing that a TEC coordinate system conforms closely to the shape of a line-source impulse response, I develop an TEC-coordinate, inline-delay-source migration strategy that enables the efficient migration of individual sail-line data. I argue that this strategy is more robust than 3D plane-wave migration because of the reduced migration aperture requirements and, commonly, a lower number of total migration runs. Synthetic imaging tests on a 3D wide-azimuth data set demonstrate the imaging advantages offered by the TEC coordinate transformation, especially in the cross-line direction. Field data tests on a Gulf of Mexico data set similarly indicate the advantage of TEC coordinates.

# Preface

The electronic version of this report<sup>1</sup> makes the included programs and applications available to the reader. The markings **ER**, **CR**, and **NR** are promises by the author about the reproducibility of each figure result. Reproducibility is a way of organizing computational research that allows both the author and the reader of a publication to verify the reported results. Reproducibility facilitates the transfer of knowledge within SEP and between SEP and its sponsors.

**ER** denotes Easily Reproducible and are the results of processing described in the paper. The author claims that you can reproduce such a figure from the programs, parameters, and makefiles included in the electronic document. The data must either be included in the electronic distribution, be easily available to all researchers (e.g., SEG-EAGE data sets), or be available in the SEP data library<sup>2</sup>. We assume you have a UNIX workstation with Fortran, Fortran90, C, X-Windows system and the software downloadable from our website (SEP makerules, SEPScons, SEPlib, and the SEP latex package), or other free software such as SU. Before the publication of the electronic document, someone other than the author tests the author's claim by destroying and rebuilding all ER figures. Some ER figures may not be reproducible by outsiders because they depend on data sets that are too large to distribute, or data that we do not have permission to redistribute but are in the SEP data library, or that the rules depend on commercial packages such as Matlab or Mathematica.

---

<sup>1</sup><http://sepwww.stanford.edu/private/docs/sep137>

<sup>2</sup><http://sepwww.stanford.edu/public/docs/sepdatilib/toc.html>

**CR** denotes Conditional Reproducibility. The author certifies that the commands are in place to reproduce the figure if certain resources are available. The primary reasons for the CR designation is that the processing requires 20 minutes or more.

**NR** denotes Non-Reproducible figures. SEP discourages authors from flagging their figures as NR except for figures that are used solely for motivation, comparison, or illustration of the theory, such as: artist drawings, scannings, or figures taken from SEP reports not by the authors or from non-SEP publications. Some 3D synthetic data examples associated with this report are classified as NR because they were generated externally to SEP and only the results were released by agreement.

Our testing is currently limited to LINUX 2.6 (using the Intel Fortran90 compiler) and the SEPlib-6.4.6 distribution, but the code should be portable to other architectures. Reader's suggestions are welcome. For more information on reproducing SEP's electronic documents, please visit <http://sepwww.stanford.edu/research/redoc/>.

# Acknowledgments

My years here at the Stanford Exploration Project and at Stanford in general have been a fantastic time in my life where I have been able to learn and grow on both a professional and personal level. I would like to acknowledge my advisor, Biondo Biondi, for his support over the years, for letting me to find my own path while exploring my thesis, and continually stressing the importance of the real 3D world. I thank Jon Claerbout for begin ahead of the curve in setting up the SEP consortium many years ago, and for setting the standard for the richness of the science and technology that continues to come out of SEP today. Bob Clapp has been a great resource for me, especially during my last few years at SEP when I became more computational. His consistently being a few steps ahead in the world of computational geophysics has greatly facilitated the completion of my 3D imaging result. I thank Diane Lau for her continual support and patience; even when bringing in buckets of receipts to her in various Slavic and Romance languages she managed to keep a smile on her face.

The majority of the time that I spent at SEP was with my fellow students, both senior and junior to me; it has been a blast. Entering into SEP and dealing with starting up research can be a daunting task, and I would like to recognize those SEPers that helped. My early interactions with Paul Sava and Antoine Guitton led to my thesis topic and I am grateful for all those discussions. I would like to thank those SEPers closer to my cohort, in particular Guojian Shan and Brad Artman, off whom I bounced many ideas. To those SEPers more junior than me: it has been fun working with you and helping you choose your research paths, and I wish you all the

best.

In addition to my SEP research, I have been fortunate enough to be involved in additional multi-disciplinary projects spanning the geosciences. I would like to thank Cameron Snow for the opportunity to study geochemical discrimination, and Charles Wilson for the time spent in teleseismic imaging. I also thank Kyle Spikes, Laura Chiaramonte and Brad Artman for the happy memories of various field camps and geo-archaeology imaging projects around the world. These were made possible by grants from the SEG Foundation, the Stanford School of Earth Sciences, and the Stanford Center for Latin American Studies, all of whom are deeply thanked.

I would like to generally acknowledge all the people in the Stanford community that have helped shaped my time here, and those with whom I have helped continue old traditions and start others anew. I have a lot of great memories and am looking forward to meeting up you at various times and locations around the world in the future. Thanks also to my housemates at Maddux over the years who have helped me hone my backyard mechanical engineering abilities. Finally, thanks to my family for supporting me through thick and thin all these years.

# Contents

Abstract	v
Preface	vii
Acknowledgments	ix
1 Introduction	1
2 RWE: Non-orthogonal coordinate systems	18
3 Shot-profile migration in elliptical coordinates	46
4 Generalized-coordinate ADCIGs	63
5 Delayed-shot migration in TEC coordinates	87
A Riemannian geometry overview	121
B Generalized phase-shift operators	123
C RWE wavenumber approximations	125

<b>D Elliptic coordinate systems</b>	<b>128</b>
<b>E ADCIG coordinate transform</b>	<b>130</b>

# List of Tables

2.1	Comparison of computational costs of the split-step Fourier and phase-shift subroutines for RWE and equivalent Cartesian implementations. Results computed for the 2D example shown in Figure 2.6. . . . .	42
2.2	Comparison between performing migration with stored or locally computed coordinate system geometry information for Cartesian (CC) and Elliptic Cylindrical (EC) coordinates. . . . .	44
5.1	Coefficients used in 3D implicit finite-difference wavefield extrapolation.	99
5.2	Parameters associated with the 3D synthetic data set. . . . .	104
5.3	Run-time comparisons for the delayed-shot migration and shot-profile styles in the tilted elliptical-cylindrical and Cartesian coordinate systems.	111
5.4	Approximate acquisition parameters associated with the 3D Gulf of Mexico field data set. . . . .	113

# List of Figures

1.1	Cartoon illustrating the problems associated with wave-equation migration using downward continuation. a) Propagation angles can become too steep in Cartesian coordinates (i.e. $\theta > \theta_{max}$ ) causing the true reflector location (black) to be inaccurately imaged (gray). b) Turning waves cannot be imaged by design in Cartesian coordinates. <b>NR</b> . . . . .	3
1.2	Comparisons between four different acoustic wave-propagation techniques through the BP velocity model. a) Two-way finite-difference modeling. b) Cartesian one-way wavefield extrapolation. c) Ray-coordinate-based one-way Riemannian wavefield extrapolation. d) Analytic coordinate one-way Riemannian wavefield extrapolation. <b>CR</b> . . . . .	5
1.3	Cartoon illustrating how making the migration geometry more conformal to the wave-propagation direction can lead to imaging improvements. a) Propagating wavefields on meshes more conformal to ray-path direction reduces the relative extrapolation angle. b) Improved coordinate system designs enable turning-wave propagation with one-way wave-equations. <b>NR</b> . . . . .	6

1.4	Cartoon illustrating the problems associated with imaging substructure using wavefields with conflicting dips. a) Coordinate system where the right-hand structure can be imaged using one-way extrapolation, but the left-hand reflector cannot. b) Example where a coordinate enables imaging of part, but not all, subsurface structure. <b>NR</b> . . . . .	7
1.5	Cartoon illustrating the four-step procedure for migrating with multiple coordinate systems and decomposed data sets. a) Decide on the data-domain decomposition and migration domains to be used. b) Decompose data and set up migration domains. c) Generate partial images using data subsets and individual migration domains. d) Combine individual images into final volume. <b>NR</b> . . . . .	8
1.6	Illustration of the RWE approach using Green's functions calculated on ray-coordinate meshes through the BP velocity model. a) Velocity model with a smooth coordinate mesh overlain. b) Velocity model in a) interpolated into ray coordinates. c) Point-source Green's function in ray coordinates at four time steps. d) Wavefield in c) interpolated to Cartesian. Note the steep, vertical and overturning waves, illustrating RWE's imaging potential. <b>ER</b> . . . . .	11
2.1	Illustration of problems with partially orthogonal RWE computational grids. a) Singularities in a coordinate system generated by ray-tracing that lead to zero-division in RWE. b) Grid bunching for a topographically conformal coordinate system that causes significant lateral variation in each extrapolation step. <b>NR</b> . . . . .	21
2.2	Sheared Cartesian coordinate system test. a) Coordinate system shear angle and velocity are $\theta = 25^\circ$ and $1500 \text{ ms}^{-1}$ , respectively. b) Zero-offset data consist of four flat plane-wave impulses at $t=0.2, 0.4, 0.6,$ and $0.8 \text{ s}$ that are correctly imaged at depths $z=300, 600, 900,$ and $1200 \text{ m}$ . <b>ER</b> . . . . .	28

2.3	Stretched polar coordinate system test example. a) Velocity function $v(x_3) = 1500 + 0.35x_3$ overlain by a stretched polar coordinate system defined by parameter $a = 1 + 0.2\xi_3 - 0.05\xi_3^2$ . b) Velocity model mapped in the RWE domain. c) Imaged reflectors in RWE domain. d) RWE domain image mapped to a Cartesian mesh. <b>ER</b> . . . . .	31
2.4	Example of singularity-free mesh generation. a) Velocity model with three Gaussian velocity perturbations. Overlain is a coordinate mesh generated from ray-tracing. Note the triplication to either side of the shot-point, as well as the spreading beneath the shot point. b) Velocity model overlain by isochrons of an Eikonal equation solution for same shot-point. c) Singularity-free, but weakly non-orthogonal, computational mesh generated by Eikonal mesh smoothing. <b>NR</b> . . . . .	34
2.5	Example of wave-equation-generated Green's functions on structured non-orthogonal mesh for a slice through the SEG-EAGE salt velocity model. a) Salt model in physical space with an overlain ray-coordinate mesh. b) Velocity model in the transform domain. c) Wavefield propagated in ray coordinates through velocity model shown in b). d) Wavefield in c) interpolated back to Cartesian space. <b>ER</b> . . . . .	36
2.6	Comparison between three different extrapolation methods. a) Two-way finite-difference modeling. b) Riemannian wavefield extrapolation. c) Cartesian wavefield extrapolation. <b>CR</b> . . . . .	37
2.7	Constant surfaces of the elliptic-cylindrical coordinate system Cartesian coordinate axes are given to a) Five constant $\xi_3$ surfaces forming confocal elliptic cylindrical shells. This represents the direction of extrapolation direction. b) Five constant $\xi_2$ surfaces representing folded hyperbolic planes. c) Five constant $\xi_1$ surfaces representing 2D elliptic meshes. <b>NR</b> . . . . .	40

2.8	Green’s function computation test in the 3D elliptical-cylindrical analytic coordinate system for a set of five flat plane waves at time 1.0, 1.5, 2.0, 2.5, and 3.0 s. Top: Elliptical-cylindrical coordinate imaging result. Bottom: Cartesian coordinate imaging result. <b>CR</b> . . . . .	41
3.1	Illustrating the elliptical coordinate system. a) Constant-velocity imaging experiment with point source and receiver wavefields (dashed lines) from locations marked $S$ and $R$ , respectively. The corresponding image is an elliptical isochron surface derived by cross-correlating the source and receiver wavefields (solid line). b) Grid rotation angles for the elliptical coordinate system with respect to the vertical Cartesian depth axis. <b>NR</b> . . . . .	51
3.2	Post-stack turning-wave data generated by two-way time-domain finite-difference modeling from all salt body edges of the velocity model in Figure 4.3a. <b>ER</b> . . . . .	55
3.3	Post-stack turning-wave model. a) Velocity model used to generate turning wave data in Figure 4.2 with coordinate system overlain. b) Effective slowness model $s_{eff}$ in elliptical coordinates. <b>ER</b> . . . . .	56
3.4	Post-stack turning-wave migration results. a) Monochromatic Cartesian image with overlain elliptical coordinates showing the wave-propagation paths. b) Monochromatic elliptical coordinate image. c) Broadband Cartesian image. d) Broadband elliptical coordinate image. <b>CR</b> . . .	57
3.5	Prestack migration test in elliptical coordinates. a) Benchmark synthetic velocity model with the elliptical coordinate system overlain. b) Effective slowness model in the transformed elliptical coordinate system. <b>NR</b> . . . . .	59
3.6	Synthetic migration results. a) Elliptical-coordinate migration result using finite-difference propagators. b) Cartesian migration result generated by finite-difference extrapolators of equivalent accuracy. <b>CR</b> .	60

4.1	Cartoon illustrating the geometry of the ADCIG calculation. Parameter $\gamma$ is the reflection opening angle, $\alpha$ is geologic dip. a) Cartesian geometry using coordinates $x_1, x_3$ and $h_{x_1}$ . b) Generalized geometry using coordinates $\xi_1, \xi_3$ and $h_{\xi_1}$ . Adapted from ?. <b>NR</b> . . . . .	67
4.2	Prestack migration test in elliptical coordinates. a) Benchmark synthetic velocity model with an overlying elliptical coordinate system. b) Effective slowness model in the transformed elliptical coordinate system in a). c) Benchmark synthetic velocity model with a different overlying elliptical coordinate system. d) Effective elliptical coordinate slowness model for the coordinate system in c). <b>NR</b> . . . . .	69
4.3	Canonical coordinate system examples. a) Tilted Cartesian coordinates. b) Polar coordinates. c) elliptical coordinates. <b>NR</b> . . . . .	72
4.4	Theoretical results for an elliptical isochron for four travel times in a constant velocity medium. The elliptical surfaces are color-coded according to reflection opening angle. <b>NR</b> . . . . .	76
4.5	Elliptical reflector comparison tests between analytically (black bullets) and numerically generated ADCIG volumes. Panels a-d are computed in elliptical coordinates (EC), while panels e-h are in Cartesian coordinates (CC). a) EC image extracted at the $-24^\circ$ reflection angle. b) EC angle gather at -1.5 km. c) EC gather at 0.75 km. d) EC gather at 0.0 km. e) CC image extracted at the $-24^\circ$ reflection angle. f) CC angle gather at -1.5 km. g) CC gather at 0.75 km. h) CC gather at 0.0 km. <b>ER</b> . . . . .	77

4.6	Elliptical reflector comparison tests between analytically (black bullets) and numerically generated ADCIG volumes using a velocity scaled by factor 0.95. Panels a-d are computed in elliptical coordinates (EC), while panels e-h are in Cartesian coordinates (CC). a) EC image extracted at the $-24^\circ$ reflection angle. b) EC angle gather at -1.5 km. c) EC gather at 0.75 km. d) EC gather at 0.0 km. e) CC image extracted at the $-24^\circ$ reflection angle. f) CC angle gather at -1.5 km. g) CC gather at 0.75 km. h) CC gather at 0.0 km. <b>ER</b> . . . . .	78
4.7	Vertical elliptical and Cartesian ADCIGs slices using the correct migration velocity model. a) elliptical coordinate image with three vertical lines showing the locations of ADCIG gathers from left to right in panels b-d. e) Cartesian coordinate image with three vertical lines showing the locations of ADCIG gathers from left to right in panels f-h. <b>CR</b> . . . . .	80
4.8	Horizontal elliptical and Cartesian ADCIGs slices using the correct migration velocity model. a) elliptical coordinate image with three horizontal lines showing the locations of horizontal ADCIG gathers from top to bottom in panels b-d. e) Cartesian coordinate image with three horizontal lines showing the locations of horizontal ADCIG gathers from top to bottom in panels f-h. <b>CR</b> . . . . .	82
4.9	Vertical elliptical and Cartesian ADCIGs slices using an incorrect migration velocity model. a) elliptical coordinate image with three vertical lines showing the locations of vertical ADCIG gathers from left to right in panels b-d. e) Cartesian coordinate image with three vertical lines showing the locations of vertical ADCIG gathers from left to right in panels f-h. <b>CR</b> . . . . .	83

4.10	Horizontal elliptical and Cartesian ADCIGs slices using an incorrect migration velocity model. a) elliptical coordinate image with three horizontal lines showing the locations of horizontal ADCIG gathers from top to bottom in panels b-d. e) Cartesian coordinate image with three horizontal lines showing the locations of horizontal ADCIG gathers from top to bottom in panels f-h. <b>CR</b> . . . . .	84
5.1	Constant surfaces of the elliptical-cylindrical coordinate system (with zero inline tilt). Cartesian coordinate axes are given by the vector diagram. a) constant $\xi_3$ surfaces forming confocal elliptical-cylindrical shells that represent the direction of extrapolation direction. b) constant $\xi_2$ surfaces representing folded hyperbolic planes. c) constant $\xi_1$ surfaces representing 2D elliptical meshes. <b>NR</b> . . . . .	96
5.2	Four extrapolation steps in $\xi_3$ of an TEC coordinate system, where the $\xi_1$ and $\xi_2$ coordinate axes are oriented in the inline and crossline directions, respectively. a) $0^\circ$ tilt angle. b) $25^\circ$ tilt angle. <b>NR</b> . . . . .	97
5.3	Elliptical-cylindrical-coordinate impulse-response tests. a) Inline section. b) Crossline section. <b>CR</b> . . . . .	101
5.4	Elliptical-cylindrical impulse response at 1300 m depth. Note the circular symmetry of the impulse response indicating little-to-no numerical anisotropy. <b>CR</b> . . . . .	102
5.5	Depth section and inline crossline sections of the Gulf of Mexico velocity model through complex 3D salt bodies. Top: 3900 m depth slice. Middle: 33000 m inline section. Top: 16000 m crossline section. <b>ER</b> .	103
5.6	Sections for the 24500 m sail line at the 15400m crossline coordinate. Top: Elliptical-cylindrical coordinate image. Bottom: Cartesian coordinate image. <b>NR</b> . . . . .	105

5.7	Crossline sections through the velocity model and full image volumes at inline coordinate 33700 m. Top panel: Elliptical-cylindrical coordinate image. Bottom panel: Cartesian coordinate image. The imaging improvements for the left-hand salt flank are denoted by the oval marked A. The oval marked B illustrates a more continuous and correctly placed reflector in the TEC coordinate system. <b>NR</b> . . . . .	106
5.8	Crossline sections through the velocity model and full image volumes at inline coordinate 15100 m. Top panel: Elliptical-cylindrical coordinate image. Bottom panel: Cartesian coordinate image. The oval marked A indicates the location of the vertical salt flank that is better imaged in TEC coordinates. <b>NR</b> . . . . .	107
5.9	Inline sections through the velocity model and full image volumes at crossline coordinate 21750 m. Top panel: Velocity section. Middle panel: Elliptical-cylindrical coordinate image. Bottom panel: Cartesian coordinate image. The left-hand salt flank, shown in oval A, is more accurately positioned in the TEC coordinate image, while the right-hand flank, marked by oval B, is similarly more accurately positioned and continuous. <b>NR</b> . . . . .	109
5.10	Depth slices through the velocity model and image volumes at 6150 m depth. Top panel: Elliptical-cylindrical coordinate image. Bottom panel: Cartesian coordinate image. Oval A illustrates the improved TEC image for the vertical salt flank shown in Figure 5.8. Oval B demarcates a region where some of the smaller-scale fractures are well imaged in both images. Oval C shows the region where the near-vertical flank shown in TEC coordinate image in Figure 5.7 is better imaged. <b>NR</b> . . . . .	110
5.11	Velocity model example for Gulf of Mexico field data set. <b>ER</b> . . . . .	112
5.12	Chosen source distribution for the field data set. <b>CR</b> . . . . .	114

5.13	Chosen receiver distribution for the field data set. The missing data between offsets $\pm 2500$ -2750 m is due to a corrupted data tape. <b>CR</b> . . . . .	114
5.14	Inline sections through the migration images taken at the 8750 m crossline coordinate location. Top: TEC coordinate migration results. Bottom: Cartesian coordinate migration results. Oval A shows the imaging improvements in TEC coordinates for the left-hand flank. <b>CR</b> . . . . .	116
5.15	Crossline sections through the migration images taken at the 7100 m crossline coordinate location. Top: TEC coordinate migration results. Bottom: Cartesian coordinate migration results. Oval A shows an example of an area where the TEC coordinate image is better than the Cartesian image. <b>CR</b> . . . . .	117
5.16	Migration results for the 3D Gulf of Mexico field data set through the sedimentary section. Top: TEC coordinate migration results. Bottom: Cartesian coordinate migration results. Oval A shows an example of an area where the TEC image is better than that generated in Cartesian, including two parts of the right-hand salt flank. Oval B shows the TEC coordinate image improvements in the crossline direction. <b>CR</b> . . . . .	118

# Chapter 1

## Introduction

The world's remaining petroleum reservoirs will be discovered using information obtained by interpreting 3D seismic images. Because petroleum explorationists have purportedly located, and are currently producing, the majority of the world's 'easy oil' - i.e. nearer to surface, in simple geologic settings, and accessible to public companies - future reservoir discoveries will be located increasingly in frontier areas characterized by more complex geology. Accordingly, the search for new hydrocarbon reserves continuously motivates the development of new, and the refinement of existing, 3D seismic imaging techniques able to better image complex subsurface structure.

The first 3D acoustic seismic imaging algorithms implemented in production settings were Kirchhoff approaches (???), which model the wave-equation using paraxial approximations. Although these techniques have been (and still are) applied successfully to seismic data from locations around the world, Kirchhoff migration routinely proves inadequate for areas of complex geology (?). Its main problems are inherited from the underlying ray-theoretic approximation: an inability to model all multipathed wavefield phases, and a difficulty in handling boundaries of strong velocity contrast. Both of these issues commonly occur at, say, salt-sediment interfaces. Generating more accurate images that facilitate 3D seismic interpretation thus requires introducing higher fidelity migration algorithms.

Full wave-equation (FWE) methods are another class of seismic imaging techniques that circumvent many problems associated with Kirchhoff migration. There are two key differences between WE and Kirchhoff approaches. First, FWE methods employ operators derived from the full acoustic wave equation - not asymptotic approximations of it - and are thus finite-frequency approaches. Second, FWE methods extrapolate seismic wavefields throughout the migration domain, not just along an incomplete set of rays. These two factors combine to ensure that FWE methods better handle multi-pathed wavefield arrivals and strong velocity contrasts.

The most accurate FWE method is reverse-time migration (??), which propagates and images individual shot-profiles using operators derived from the full acoustic wave equation. Although this approach generates the highest-quality FWE migration results, the computational cost, I/O throughput, and memory requirements for performing reverse-time migration on typical industry-sized 3D data sets are still too onerous for all but the most powerful computer clusters. Thus, one must turn to approximate FWE methods that retain much of the accuracy of reverse-time migration, but are less computationally demanding and have lower I/O and memory requirements.

One-way wave equations are some of the more commonly used approximations that realize these objectives (??). Conventional migration methods based on one-way equations recursively extrapolate surface-recorded wavefields step-wise in depth. Images are generated at each level by evaluating a physical imaging condition. Relative to reverse-time migration, the computational costs of one-way extrapolation approaches are significantly lower [i.e. approximately 30-50 times (?)], which affords efficient migration of industry-sized 3D data sets on relatively modest clusters.

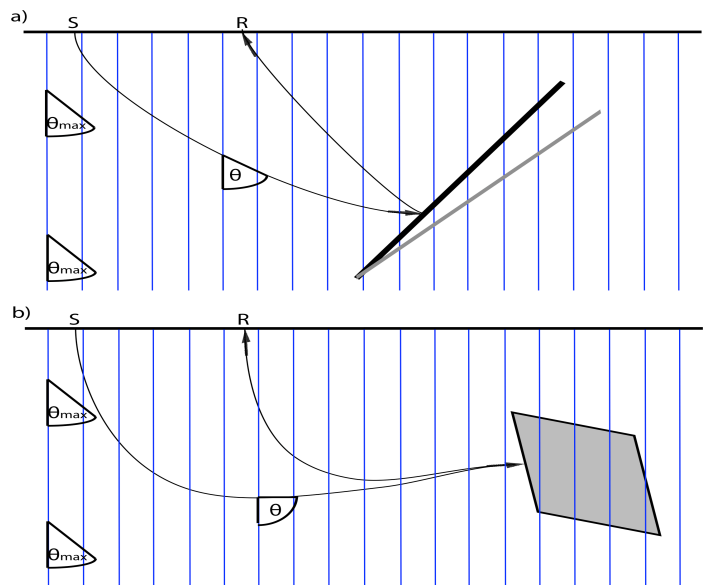
Wave-equation migration using one-way extrapolation operators, though, has some significant implementation and conceptual limitations. Figure 1.1 introduces two of these problems. The first issue is that one-way wavefield extrapolation in laterally varying media becomes inaccurate at steep propagation angles (i.e. where  $\theta > \theta_{max}$  in Figure 1.1a). The angular limit of accurate propagation, with respect to a vertical extrapolation axis, is usually given between  $\theta_{max} \approx 45^\circ$  to  $\theta_{max} \approx 85^\circ$ , depending on

the particular implementation. For cases exhibiting nearly horizontal geology, this assumption seldom greatly affects the seismic imaging result. However, inaccurately propagating energy originating from steeply dipping or discontinuous structure (e.g. faults, salt flanks) can generate erroneous subsurface images that may lead to incorrect geologic interpretations. Figure 1.1a depicts this problem by showing a second gray reflector imaged at the incorrect location.

A second conceptual issue is that downward continuation cannot propagate the upgoing paths of turning waves by design because the extrapolation direction is always oriented downward (see Figure 1.1b). Thus, conventional migration in Cartesian geometry precludes imaging complex structure with turning wavefield components, which can be detrimental to imaging and interpretation in areas of otherwise poor illumination [though two-pass migration approaches (?) somewhat obviate these concerns]. Figure 1.2 illustrates these two problems by exhibiting propagation differences

Figure 1.1: Cartoon illustrating the problems associated with wave-equation migration using downward continuation. a) Propagation angles can become too steep in Cartesian coordinates (i.e.  $\theta > \theta_{max}$ ) causing the true reflector location (black) to be inaccurately imaged (gray). b) Turning waves cannot be imaged by design in Cartesian coordinates.

NR Intro/. Problem1



between two-way finite-difference modeling (panel 1.2a) and one-way Cartesian wavefield extrapolation (panel 1.2b). The two panels show the wavefield after propagation

through the BP velocity model at the 1, 2, 3 and 4s time steps. The Cartesian wavefield is similar in many respects to the two-way modeling, suggesting that it is sufficient for correctly imaging most of the seismic wavefield. However, the two-way modeling in panel 1.2a contains many additional upward-propagating events not present in the Cartesian one-way panel. The Cartesian wavefields also become inaccurate at steep propagation angles, in particular through the salt body to the right-hand-side. These Cartesian one-way propagation errors will generate incorrectly positioned (or absent) reflectors and lead to increased interpretation uncertainty. Hence, overcoming the problems of inaccurate high-angle and turning-wave propagation - while maintaining the computational advantages of one-way wave equations - is an important seismic imaging research goal, and motivates most of the work (i.e. generating the more accurate propagation physics in Figures 1.2c and d) reported in this thesis.

## IMPROVING ONE-WAY EXTRAPOLATION

Much geophysical research in the past few decades has been devoted to mitigating problems associated with inaccurate one-way steep- and turning-angle propagation. Because most issues with one-way equations arise where assuming depth-oriented extrapolation axes, many authors have directly (or indirectly) reevaluated whether or not to use Cartesian coordinates as the geometric basis for FWE migration.

Consider again the ray paths in the Cartesian reference frames in Figure 1.1. In both cases, the angle between the ray and the vertical extrapolation axis increases beyond the maximum extrapolation angle, leading to inaccurate downward continuation. Defining wavefield extrapolation on coordinate meshes more conformal to the ray paths (Figure 1.3) would eliminate this problem because the effective extrapolation angle always obeys  $\theta < \theta_{max}$ . Hence, one central concept involved with extrapolating wavefields on non-Cartesian geometry is to find coordinate systems that lower the relative angle between the propagation direction and extrapolation axis orientation.

One important caveat is that the migration geometry in Figure 1.3 is optimized

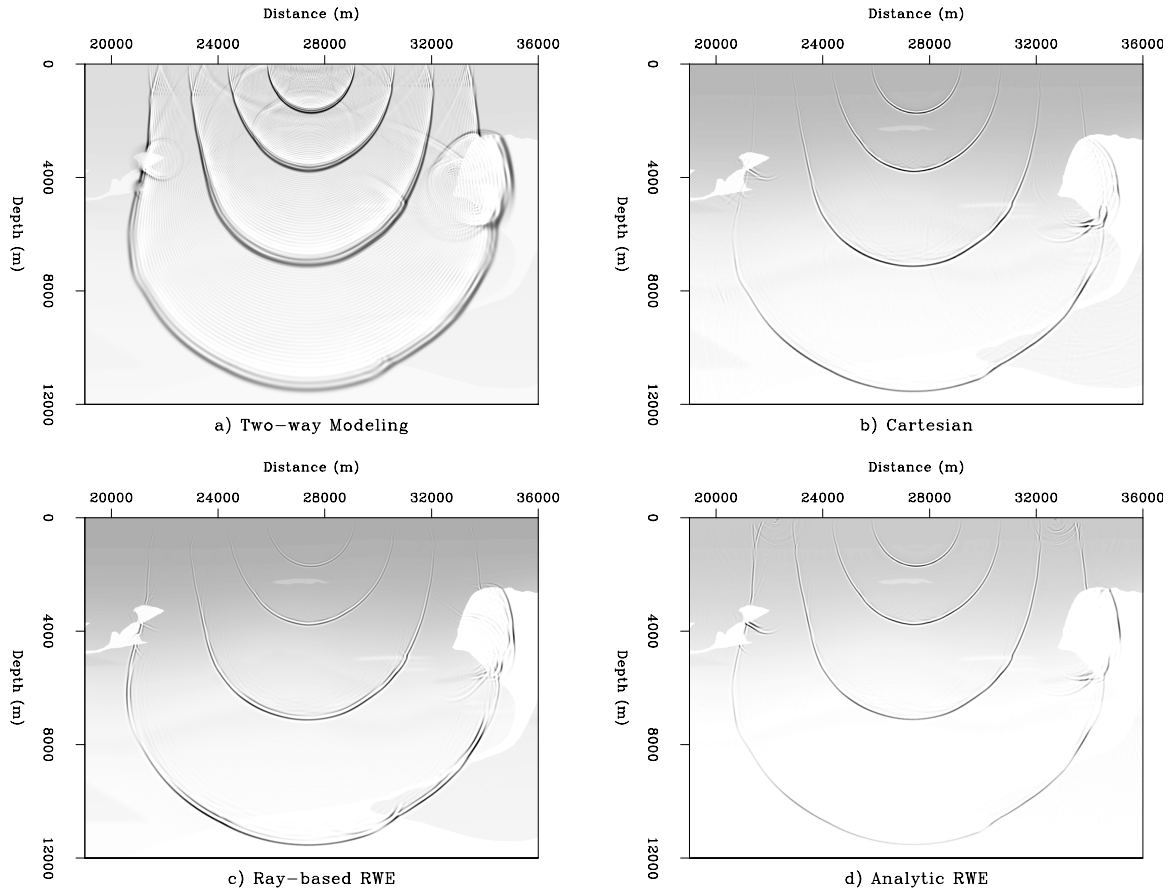
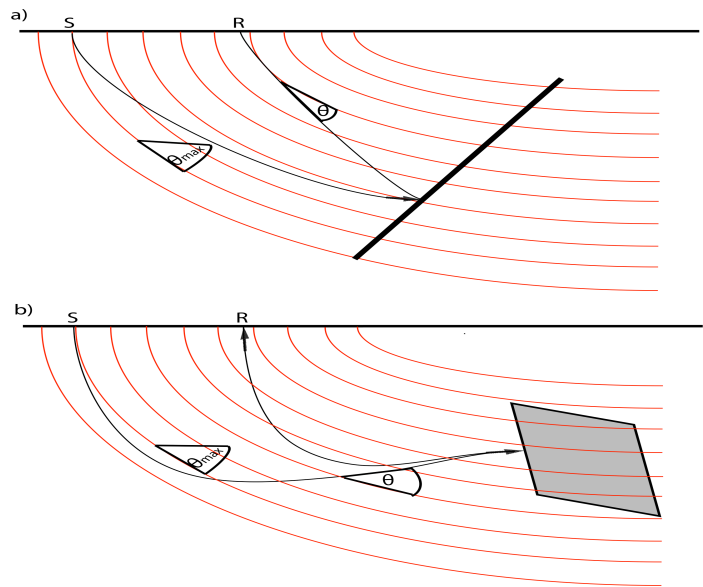


Figure 1.2: Comparisons between four different acoustic wave-propagation techniques through the BP velocity model. a) Two-way finite-difference modeling. b) Cartesian one-way wavefield extrapolation. c) Ray-coordinate-based one-way Riemannian wavefield extrapolation. d) Analytic coordinate one-way Riemannian wavefield extrapolation. **CR** Intro/. MCOMP

Figure 1.3: Cartoon illustrating how making the migration geometry more conformal to the wave-propagation direction can lead to imaging improvements. a) Propagating wavefields on meshes more conformal to ray-path direction reduces the relative extrapolation angle. b) Improved coordinate system designs enable turning-wave propagation with one-way wave-equations. **NR**

Intro/. Solution1



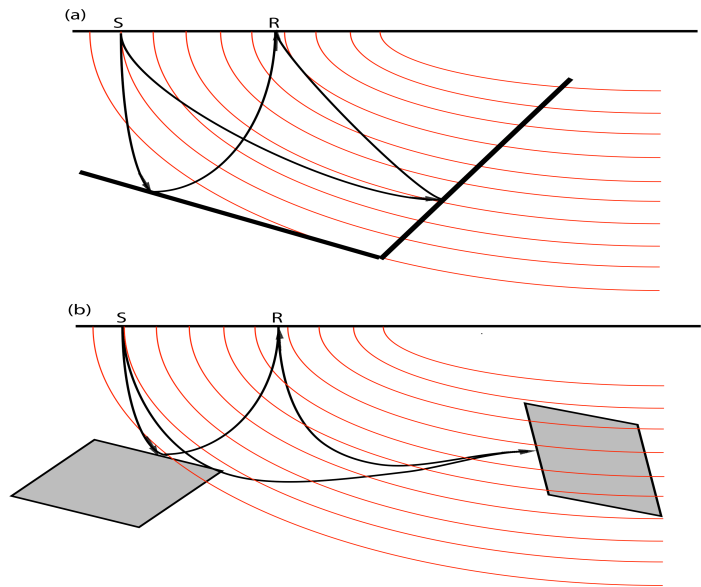
only for individual ray paths. One obvious question is, thus, how can this approach be extended to cases where multiple ray paths interrogate subsurface structures of opposing dip? Figure 1.4 illustrates this for the steep dip and the turning-wave imaging problems. Evidently, alternate coordinate systems are not, alone, a panacea to the problems of one-way wavefield extrapolation.

One effective way to resolve to this question involves decomposing the total data volume into subsets on the basis of wavefield dips or some other data localization scheme. These partial data volumes then can be extrapolated on separate coordinate systems designed to be more conformal to the wave-propagation direction of the individual data subset.

Figure 1.5 illustrates the four steps associated with this approach. The first step is deciding which data decomposition scheme and coordinate mesh are optimally matched for the particular imaging task. The next step is performing the data decomposition and setting up the different coordinate meshes. Third, individual migration images are computed on the different coordinate systems. These images are stacked into the final image in the last step. Accordingly, imaging in non-Cartesian geometry requires coordinating two important concepts: wavefield decomposition and

Figure 1.4: Cartoon illustrating the problems associated with imaging substructure using wavefields with conflicting dips. a) Coordinate system where the right-hand structure can be imaged using one-way extrapolation, but the left-hand reflector cannot. b) Example where a coordinate enables imaging of part, but not all, subsurface structure. **NR**

Intro/. Problem2



coordinate systems conformal to propagation directions.

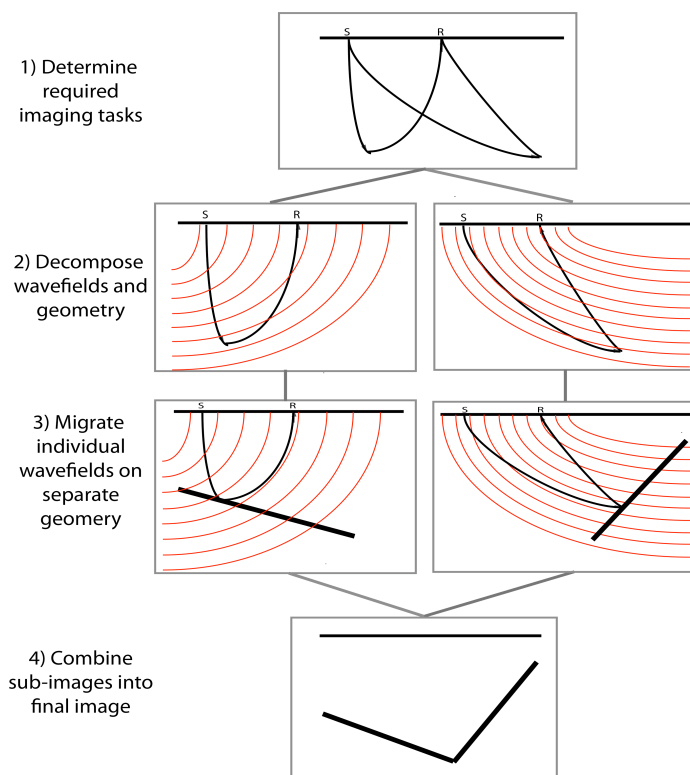
## Established migration strategies

A number of established migration methods follow these two basic concepts: directional depth migration (?), turning-wave migration (?), Gaussian beam migration (??), coherent states (?), beam waves (?), plane-wave migration in tilted coordinates (?), and Riemannian wavefield extrapolation (??). Although these approaches share many commonalities, they differ in a number of respects:

- Data domain decomposition - numerous ways of data decomposition exist, including beams, shot profiles, and synthesized plane-wave sections;
- Mesh generation technique - coordinate systems can be generated in a variety of ways, ranging from ray tracing to specifying analytic grids; and
- Extrapolation localization - propagation domains vary greatly in size, ranging from narrow beams to alternate full migration domains.

Figure 1.5: Cartoon illustrating the four-step procedure for migrating with multiple coordinate systems and decomposed data sets. a) Decide on the data-domain decomposition and migration domains to be used. b) Decompose data and set up migration domains. c) Generate partial images using data subsets and individual migration domains. d) Combine individual images into final volume. **NR**

Intro/. Solution2



Two common examples of this approach are Gaussian beams and plane-wave migration in tilted coordinates. Gaussian beam migration is a hybridization of ray and wavefield methods. Generally, beam migrations use ray tracing to generate a skeleton mesh for a suite of take-off angles at each point. The corresponding wave-packets are propagated and imaged along domains defined by a narrow beam-waist around each traced ray. Final images are generated by superposing individual beam images. These powerful approaches have the advantage of coupling ray methods with wavefield techniques that inherently produce multi-pathing and other band-limited properties. Beams also can be propagated to steep and overturning angles. Some disadvantages include leaving model space shadow zones, not handling diffractions from sharp velocity model features due to localized beam domains, and introducing beam superposition artifacts such as beam boundary effects.

Another successful approach is plane-wave migration in tilted coordinates (?). This method exploits the fact that full 3D data volumes can be synthesized into

plane-wave sections. The resulting number of plane-wave sections for migration is significantly fewer than the corresponding number of shot profiles, leading to improved computational efficiency. Because a plane wave is defined by a single take-off ray parameter, Cartesian meshes easily can be rotated to that orientation to be more conformal to the propagation direction. Individual plane-wave migration images are computed separately on the different rotated Cartesian meshes, and interpolated/s-tacked to form the final Cartesian image volume. Advantages of this approach include accurate large-angle propagation and a significant reduction in the number of required migrations. Some disadvantages are that the aperture for 3D plane-wave migration can be substantial and impose a significant memory burden, and that the image quality degrades as plane-wave sampling becomes increasingly sparse. An additional concern is that common acquisition geometries do not lend themselves well to this approach - in particular where the number of acquired sail lines exceeds the number of plane waves required in the cross-line direction to achieve a non-aliased image.

## RIEMANNIAN WAVEFIELD EXTRAPOLATION

Riemannian wavefield extrapolation (RWE) is another method for propagating wavefields on generalized coordinate meshes (?). As before, the key idea is to globally transform the computational domain from Cartesian to a geometry where the extrapolation axis conforms to the bulk wavefield propagation direction. The main difference in RWE, though, is that the transformation is global and not confined to narrow propagation domains like beams. Changing the migration geometry requires properly formulating one-way wave equations in the transformed domain. ? and ? demonstrate how this can be done by writing the governing 3D Helmholtz equation on general Riemannian manifolds (?), and generating corresponding extrapolation wavenumbers using conventional one-way wave-equation approximations (?).

An instructive RWE example is generating a 2D point-source Green's function using a coordinate system formed by a suite of rays traced through a velocity model. Figure 1.6 presents a RWE-generated Green's function example. The upper (lower)

panels represent the velocity (image) domains, while the left (right) panels show the Cartesian (Riemannian) domains. The first procedural step is to generate the smooth ray-coordinate mesh (Figure 1.6a) using Huygens' wavefront tracing (?) on a smoothed BP synthetic velocity model (?). Figure 1.6b shows the mesh transformed into the ray-coordinate domain overlying the interpolated velocity model. The extrapolation axis in this reference frame is parameterized by travel time along a ray, while the orthogonal axis is shooting angle.

Generating a point-source Green's function in Cartesian coordinates requires introducing an impulsive wavefield at the first extrapolation step. The corresponding wavefield state in the first step of the ray-coordinate system is a plane wave, which is equivalent to outwardly extrapolating equal energy at all shooting angles. The wavefield is then propagated through the velocity model to generate the ray-coordinate wavefield (Figure 1.6c) at four different travel times, which are then interpolated back to Cartesian (Figure 1.6d) using the known and invertible mapping relationship between two grids. The resulting Cartesian wavefield has energy at steep, vertical and overturning angles, which illustrates the potential for RWE to improve upon the conventional limits of wide-angle and turning-wave propagation by one-way extrapolation.

Figures 1.2 show the RWE wavefield extrapolation improvements, relative to that in a Cartesian coordinate system and the two-way finite difference modeling benchmark. Note the improved accuracy at large propagation angles of ray-based RWE extrapolation (panel 1.2c), especially within the right-hand salt body, relative to Cartesian extrapolation (panel 1.2b).

## Challenges with existing RWE implementations

Although the RWE naturally adapts to propagation in 2D ray-coordinate systems, the approach described by ? has numerous numerical implementation and conceptual challenges that need to be resolved before RWE can be applied successfully in 3D

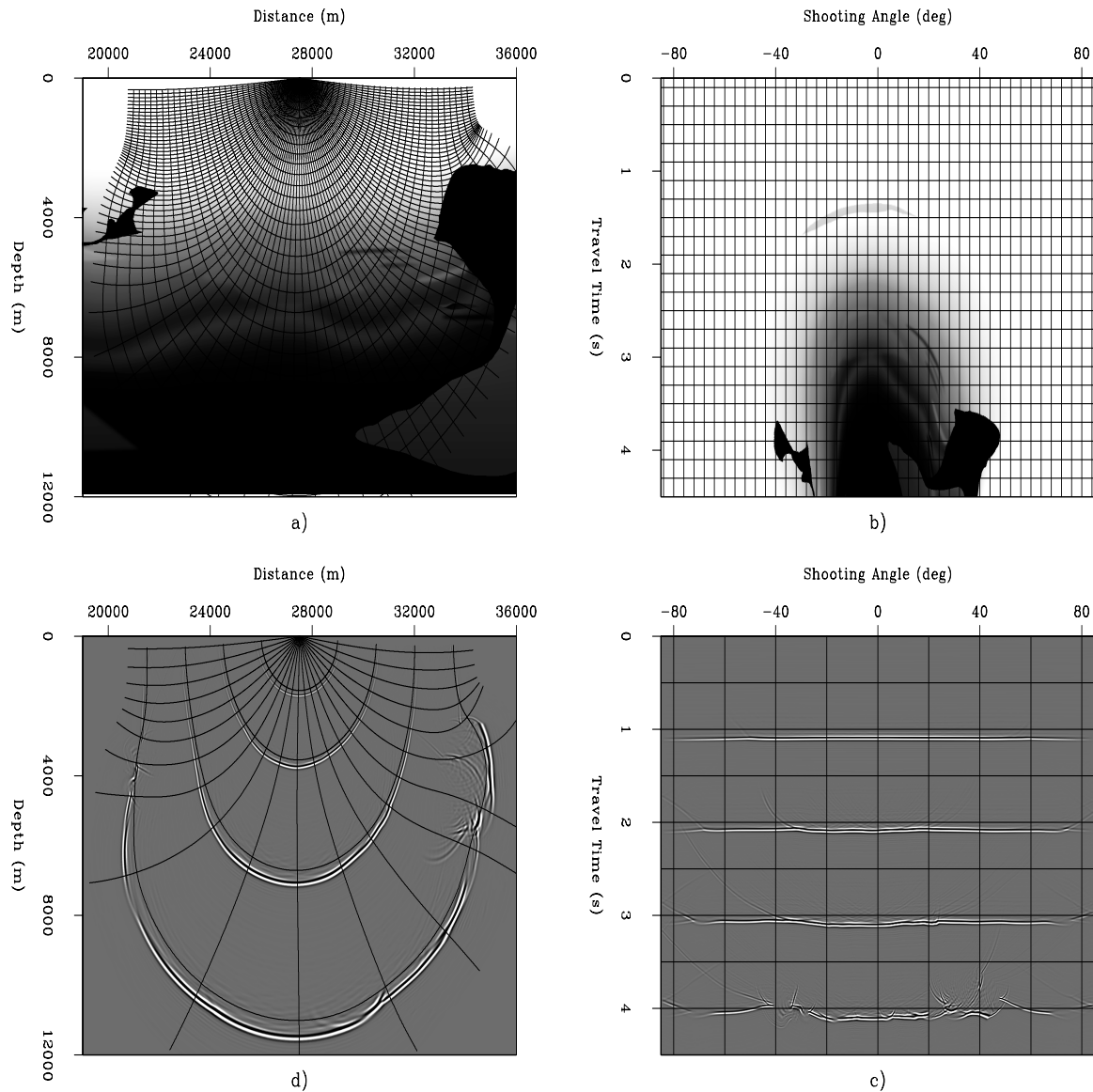


Figure 1.6: Illustration of the RWE approach using Green's functions calculated on ray-coordinate meshes through the BP velocity model. a) Velocity model with a smooth coordinate mesh overlain. b) Velocity model in a) interpolated into ray coordinates. c) Point-source Green's function in ray coordinates at four time steps. d) Wavefield in c) interpolated to Cartesian. Note the step, vertical and overturning waves, illustrating RWE's imaging potential. **ER** `Intro/. RWEexample`

prestack migration scenarios. One major implementation issue is how to handle ray-coordinate triplications. Standard ray theory predicts infinite amplitudes in the limit where distances between neighboring rays goes to zero. Similarly, RWE generates unstable amplitudes at triplications because the formulation effectively normalizes amplitudes by a measure related to the inter-ray distance. A related issue is that significant ray-coordinate bunching or spreading can occur, even where meshes are triplication-free, which generate spurious grid reflection noise that degrades wavefield extrapolation quality.

A second implementation issue is that meshes generated through 2D ray-tracing are orthogonal grids, because the extrapolation direction is always orthogonal to the other (shooting-angle) axis. Similarly, meshes formed by 3D ray-tracing are limited to partial orthogonality because the extrapolation direction is orthogonal to the two other, not necessarily mutually orthogonal (shooting angle) axes. The assumption of (partial) orthogonality is unnecessarily restrictive as it precludes using smoother, non-orthogonal, triplication-free meshes.

Two additional conceptual challenges have made it difficult to apply RWE effectively and efficiently in more general prestack migration settings. (Herein, I will be assuming a shot-profile migration style unless otherwise specified.) First, the receiver wavefields used in shot-profile migration are usually broadband in plane-wave dip spectrum and cannot be easily represented by a single coordinate system. (That is, reflections from opposing dips propagate in opposing directions, as illustrated in Figure 1.4.) A second issue is that the coordinate systems optimal for point source and receiver wavefields seldom share a common geometry. For example, polar (spherical) coordinate systems are well-suited for propagating 2D (3D) point source wavefields, while elliptic (ellipsoidal) meshes are more appropriate for 2D (3D) receiver wavefields. This factor is detrimental to algorithmic efficiency where images are generated by correlating source and receiver wavefields: by existing on different grids they must both be interpolated to a common Cartesian reference frame prior to imaging. This leads to a significant number of interpolations, which renders the algorithm computationally unattractive, except in target-oriented imaging situations.

Establishing RWE-based migration as a viable seismic imaging technique will require resolving these implementation and conceptual challenges. Overcoming these problems represents the main contributions of this thesis.

## THESIS CONTRIBUTIONS

The central goal of this thesis is to demonstrate that RWE-based migration is a viable 3D seismic imaging technique. A second goal is to prove that RWE-based approaches afford significant imaging improvements over conventional one-way extrapolation-based techniques at modest additional (and sometimes a reduced) computational cost.

The first major contribution is a new RWE formulation, more general than that of ?, that opens up new approaches for coordinate system design including non-orthogonal meshes. This extension leads to a more explicit connection of coordinate geometry in one-way wave equations, and helps define analytical extrapolation wavenumbers that improve the accuracy of RWE operator implementations. I also explore more wavefield-centric coordinate design approaches derived from ray-tracing algorithms. Propagation on these coordinate systems leads to extrapolated wavefields more accurate than those calculated in Cartesian coordinates, though of lower accuracy than analytic coordinate approaches. Both the analytic and ray-derived mesh generation techniques discussed herein avoid the problems associated with triplicating coordinate systems discussed in ?. Overall, I argue that analytic coordinates represent a more optimal trade-off between the competing constraints of extrapolation axes conforming to wavefield propagation directions, and the numerical accuracy and computational efficiency of the extrapolation operator implementation. This assertion is illustrated in Figure 1.2d, which shows the potential accuracy increases afforded by wavefield extrapolation in analytic coordinates relative to Cartesian and ray-traced coordinates in panels 1.2b and 1.2c, respectively.

The second contribution is extending the RWE approach to prestack migration,

which was rendered conceptually challenging by the issues discussed in the above section. For 2D examples I show that elliptic coordinate systems have useful geometric properties, and are an appropriate geometry for propagating both the source and receiver wavefields. I demonstrate that elliptic-coordinate migration is an example where the trade-off between the competing constraints of large-angle accuracy, ease of numerical implementation, and computational cost overhead is excellent, if not optimal. Tests on the BP velocity synthetic data set demonstrate that elliptic-coordinate migration results offer significant imaging improvements over conventional Cartesian WE migration algorithms.

Next, I examine whether angle-domain common-image gather (ADCIG) theory remains valid in generalized 2D coordinate systems. I demonstrate that ADCIGs can be calculated directly using Fourier-based methods for a particular class of coordinate system that include elliptic meshes. I show that computing ADCIGs in elliptic coordinates offers imaging advantages over doing so in Cartesian grids. In particular, I argue that the spatially varying extrapolation axis leads to more accurate large-angle propagation while minimizing the insensitivity of the ADCIG calculation to steep structural dips commonly observed in conventional implementations.

Finally, I examine what combination of coordinate system geometry and wavefield decomposition provides an optimal match for 3D prestack migration. I argue that an inline delayed-shot migration strategy is an effective strategy for situations where the sources are well-sampled inline, but have a limited number of sail lines or the sail-line sampling is too coarse. Using line sources, though, leads to impulse responses with more conical-like geometries that remain more linear in one direction, and more cylindrical in the other. Extending the analytic approach above to 3D, I detail a RWE migration strategy for performing inline delayed-shot migration using tilted elliptical-cylindrical (TEC) meshes that conform fairly well to the shape of a general linear-source impulse response. This approach retains the efficiency of plane-wave migration, while affording the migration of most steep-dip and turning-wave components to all azimuths. I present wide-azimuth migration results to validate the theory for a wide-azimuth synthetic 3D data set computed from a realistic Gulf of Mexico geologic

model. The imaging results indicate that migration in TEC geometry offers imaging improvements over Cartesian meshes, especially for steeply dipping geologic structures such as salt flanks, at a reduced computational cost. The approach is applied to a 3D narrow-azimuth Gulf of Mexico data set to demonstrate the imaging advantages in a field data test.

## THESIS OVERVIEW

**Chapter 2: RWE: Non-orthogonal coordinate systems** - I demonstrate how the RWE approach can be extended to include modeling one-way wave propagation on generalized coordinate meshes. The RWE implementation of ? assumes that coordinate systems are defined by either orthogonal or semi-orthogonal geometry. This restriction leads to situations where coordinate meshes suffer from problematic bunching and singularities. I develop a procedure for avoiding many of these problems by posing wavefield extrapolation on smooth, generally non-orthogonal, but singularity-free, coordinate meshes. The resulting extrapolation operators include additional terms that describe non-orthogonal propagation effects. These extra degrees of complexity, however, are offset by smoother coefficients that are more accurately implemented in one-way extrapolation operators. I validate my theory of non-orthogonal propagation with two analytic coordinate system examples, and present a method for eliminating any remaining singularities from coordinate systems. I demonstrate non-orthogonal RWE through numerical calculation of 2D and 3D Green's functions for cylindrical and near-spherical geometry. Results from 2D benchmark testing suggest that the computational overhead associated a mixed space- and Fourier-domain RWE implementation is roughly 35% greater than Cartesian-based extrapolation. However, I show that the computational overhead in analytic coordinate systems, even in 3D applications, is likely to be less than 6% greater than the corresponding cost in Cartesian coordinates. Results from this chapter have been published as ?.

**Chapter 3: Shot-profile migration in elliptic coordinates** - I extend the Riemannian wavefield extrapolation (RWE) formulation of Chapter 2 to 2D prestack

migration using analytically defined elliptic-coordinate systems. I show that the corresponding 2D elliptic extrapolation wavenumber introduces only an isotropic slowness model stretch to the single-square-root operator. This enables the use of existing Cartesian finite-difference extrapolators for propagating wavefields on elliptic meshes. A post-stack migration example illustrates the ability of elliptic coordinate migration to image with turning waves. A 2D imaging test using a velocity benchmark data set demonstrates that the RWE prestack migration algorithm generates high-quality migration images that are more accurate than those generated by Cartesian operators of the equivalent accuracy. I note that even in situations where RWE geometries are employed, a high-order implementation of the one-way extrapolator operator is required for accurate propagation and imaging. Results from this chapter have been published as ?.

**Chapter 4: Generalized coordinate ADCIGs** - Chapter 4 extends the theory of 2D angle-domain common-image gathers (ADCIGs) to migrations performed in generalized coordinate systems. I develop an expression linking the definition of reflection opening angle to various geometric factors. I demonstrate that generalized coordinate ADCIGs can be calculated directly using Fourier-based offset-to-angle approaches for locally isotropic coordinate systems. Tilted Cartesian, polar and elliptic coordinate examples are provided to help illustrate theory. I validate the ADCIG theory by comparing analytically and numerically generated image volume results for a set of elliptically shaped reflectors. Experiments with the BP velocity synthetic data set demonstrate that elliptic-coordinate ADCIGs better-resolve steeply dipping structure relative to Cartesian ADCIGs. Results from this chapter have been accepted for publication as ?.

**Chapter 5: Inline delayed-shot migration in TEC coordinates** - Chapter 5 extends the 2D analytic RWE approach of Chapter 3 to 3D coordinate systems. I show how to perform inline delay-shot migration in tilted elliptical-cylindrical (TEC) coordinate systems. The elliptic geometry is oriented in the cross-line direction, which naturally allows the inline oriented linear source to propagate to steep angles and overturn as necessary. When inline coordinate tilt angles are well-matched

to the inline plane-wave ray parameters, the TEC coordinate extension affords accurate propagation of most steep-dip and turning-wave components of inline-source phase-encoded wavefields to all azimuths. I show that wavefield extrapolation in TEC coordinates is no more complicated than propagation in elliptically anisotropic media. Impulse response tests using  $80^\circ$  finite-difference operators illustrate the implementation's large-angle accuracy and lack of numerical anisotropy. I apply this approach to a 3D wide-azimuth synthetic and a 3D narrow-azimuth Gulf of Mexico data set to demonstrate the imaging advantages made possible through 3D RWE implementations.

## Chapter 2

# RWE: Non-orthogonal coordinate systems

This chapter shows how Riemannian wavefield extrapolation (RWE) can be used to model one-way wave propagation on generalized coordinate meshes. Previous RWE implementations assume that coordinate systems are defined by either orthogonal or partially orthogonal geometry. This restriction leads to situations where coordinate meshes suffer from problematic bunching and singularities. I develop a procedure to avoid these problems by posing wavefield extrapolation on smooth, but generally non-orthogonal and singularity-free, coordinate meshes. The resulting extrapolation operators include additional terms that describe non-orthogonal propagation. These extra degrees of complexity, however, are offset by smoother coefficients that are more accurately implemented in one-way extrapolation operators. I validate my theory of non-orthogonal propagation with two analytic coordinate system examples, and I present a method for eliminating any remaining coordinate singularities. I demonstrate the accuracy of the non-orthogonal RWE approach by numerical calculation of 2D Green's functions. Testing results in 3D analytic coordinates are performed using an elliptic cylindrical coordinate system. Results from 2-D benchmark testing suggest that the computational overhead associated with this wavefield extrapolation implementation on numerically generated coordinates using mixed space and

Fourier-domain extrapolation operators is roughly 35% greater than the equivalent Cartesian-based implementation. Wavefield propagation in 2D and 3D analytic coordinate systems, though, does not require storing the coordinate geometry in memory, resulting in significantly more efficient extrapolation operators. The main results from this chapter have been published as ?.

## INTRODUCTION

A persistent goal of wave-equation migration research is to improve seismic imaging capabilities in complex geologic settings. Although ubiquitous velocity model uncertainty and uneven illumination can contribute greatly to image interpretation ambiguity in these contexts, extrapolation operator inaccuracy remains a significant problem. The central issues with conventional one-way wave-equation extrapolation operators are well documented: while naturally handling wavefield multi-pathing in the presence of lateral velocity variation, they are of limited large-angle accuracy and cannot propagate turning waves by design [though extensions like two-pass migration (??) address some of these concerns]. Propagation errors are subsequently manifest in migration images as defocused or misplaced reflectors or even by a complete absence of interpretable reflectivity. Accordingly, minimizing these deleterious effects should improve image quality and any subsequent interpretation based thereon.

One strategy for reducing extrapolation operator inaccuracy is to decompose the complete computational grid into subdomains oriented in the wave propagation direction. Examples of this approach include Gaussian beams (?), coherent states (?), beam-waves (?) or tilted Cartesian meshes (?). The key concept in each of these approaches is that a judicious choice of reference frame lowers the effective local propagation angle, reducing the need for expensive global extrapolation operators and enabling imaging with turning waves. ? followed this approach in developing Riemannian wavefield extrapolation (RWE), a theory of one-way wavefield propagation for 3D numerically generated, partially-orthogonal meshes. This formulation

specifies the wave-equation operators appropriate for wavefield extrapolation on generalized computational meshes. One important ramification is that the user is free to specify the degree to which the wave-propagation direction is aligned with the computational mesh. However, finding the optimal trade-off between computational mesh simplicity, how well the mesh conforms to the wavefield propagation direction, and the computational cost is not a straightforward task.

? initially implemented RWE to model high-quality Green’s functions. This process involved extrapolating wavefields on a point-source coordinate mesh comprised of a suite of rays traced beforehand through a smoothed version of the migration velocity model. Hence, RWE computational meshes explicitly were asserted to exhibit ray-field characteristics: partially orthogonal geometry with an extrapolation direction (i.e. travel-time along a ray) orthogonal to the two other axes (i.e. shooting angles) that are not necessarily mutually orthogonal. This geometric restriction leads to wave-equation dispersion relationships that contain a number of mixed spatial and wavenumber domain terms (i.e. a simultaneous dependence on  $\mathbf{x}$  and  $\mathbf{k}_x$ ) that encode coordinate system geometry. In most examples, modeled Green’s function estimates interpolated into the Cartesian domain are highly accurate at large propagation angles; however, accuracy is compromised in certain situations exhibiting unfavorable characteristics such as extensive mesh compression/extension or in the presence of singularities.

Partial orthogonal geometry, though, can be an overly restrictive assertion. One problematic example is illustrated by the coordinate system singularities observed in Figure 2.1a. These situations arise wherever a mesh is generated from a rayfield that includes a crossing set of rays, which generates spatial singularities and singular Jacobians that lead to zero-division during wavefield extrapolation. Although ray-coordinate singularities can be avoided by iterative velocity model smoothing, this less-than-ideal solution counters the goal of having a coordinate system conformal to the wavefield propagation direction. A second example of restrictive partially orthogonal geometry is illustrated in ?, who formulate a wave-equation migration from topography strategy that poses wavefield extrapolation directly in locally orthogonal

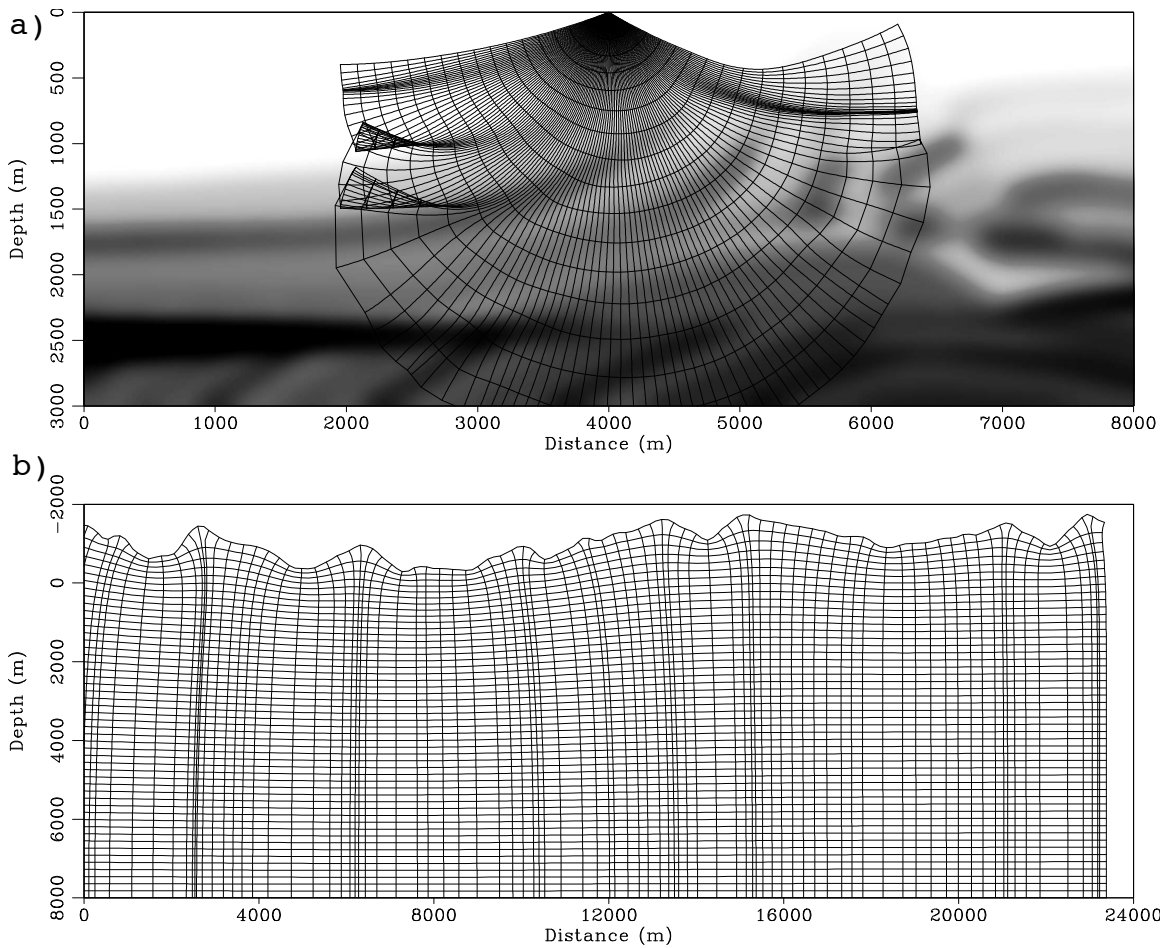


Figure 2.1: Illustration of problems with partially orthogonal RWE computational grids. a) Singularities in a coordinate system generated by ray-tracing that lead to zero-division in RWE. b) Grid bunching for a topographically conformal coordinate system that causes significant lateral variation in each extrapolation step. **NR** geono/. Fig1

meshes conformal to the acquisition surface (see Figure 2.1b). This approach successfully generates subsurface images beneath areas exhibiting longer wavelength and lower amplitude relief; however, imaging results in situations involving more rugged acquisition topography degrade due to the grid compression/extension demanded by partially orthogonal geometry.

In this chapter, I argue that generalizing RWE to non-orthogonal geometries resolves many of the issues associated with partially orthogonal meshes, affords the use of smoother computational meshes, and leads to a procedure for removing all coordinate singularities. To these ends, I develop and implement a one-way wave-equation extrapolation operator appropriate for RWE in 3D non-orthogonal coordinates. A second goal is to specify a procedure for generating unconditionally singularity-free computational meshes. My development follows that of ?; however, I recast the theory in a more compact notation that allows for a closer analytic connection of the generalized computation geometry with the underlying Cartesian grid. I begin with the formulation of the 3D Riemannian acoustic wave-equation and the corresponding non-orthogonal one-way wavefield extrapolation wavenumber. Appendix A presents an overview of the required differential geometry theory, while the split-step Fourier extrapolation operator used to compute this chapter’s examples is derived in Appendix B. Two analytic 2D non-orthogonal coordinate system examples are then provided to validate the theory. The final sections detail a procedure for generating singularity-free coordinate systems, present 2D and 3D Green’s functions estimates modeled in cylindrical and elliptical-cylindrical coordinates, respectively, and discuss the relative computational cost and memory overhead of the RWE method.

## ACOUSTIC WAVE EQUATION IN 3D GENERALIZED RIEMANNIAN SPACES

To specify the acoustic wave-equation in a 3D Riemannian space, the physics of wave-propagation must be formulated in a generalized coordinate system framework. By definition, generalized Riemannian coordinates are related to the underlying Cartesian

mesh by unique transformations (i.e. singularity-free and one-to-one). I use a notation where a generalized coordinate system  $\boldsymbol{\xi} = \{\xi_1, \xi_2, \xi_3\}$  is related to a Cartesian grid  $\boldsymbol{x} = \{x_1, x_2, x_3\}$  through transformation  $x_j(\xi_k) = f_j$ , where  $j, k = 1, 2, 3$ . Provided these conditions are met, the monochromatic wave-equation for an acoustic wavefield,  $U$ , in a generalized Riemannian space is,

$$\nabla_{\boldsymbol{\xi}}^2 U = -\omega^2 s^2 U, \quad (2.1)$$

where  $\nabla_{\boldsymbol{\xi}}^2$  is the Laplacian operator applied in coordinates  $\boldsymbol{\xi}$ ,  $\omega$  is frequency, and  $s$  is the propagation slowness.

A correct formulation of the wave-equation in the  $\boldsymbol{\xi}$ -coordinate system requires that Laplacian operator  $\nabla_{\boldsymbol{\xi}}^2$  be specified by differential geometry relationships. (Appendix A provides an overview of necessary differential geometry theory.) The Laplacian operator in generalized coordinates is (?),

$$\nabla_{\boldsymbol{\xi}}^2 U = \frac{1}{\sqrt{|\mathbf{g}|}} \frac{\partial}{\partial \xi_j} \left( m^{jk} \frac{\partial U}{\partial \xi_k} \right), \quad j, k = 1, 2, 3, \quad (2.2)$$

where  $|\mathbf{g}|$  is the metric tensor discriminant with elements  $g^{jk}$ , and  $m^{jk} = \sqrt{|\mathbf{g}|} g^{jk}$  is weighted metric tensor element that enables a more compact notation. Unless otherwise stated, summation over all repeated indicies (i.e.  $j, k = 1, 2, 3$ ) is assumed throughout. Note also that convention where superscript indicies (e.g.  $m^{jk}$ ) on matrices indicates a contravariant tensor, while subscript indicies (e.g.  $g_{jk}$ ) on matrices denotes covariant tensors (?).

Substituting equation 2.2 into 2.1 leads to the Helmholtz equation appropriate for propagating waves through a 3D Riemannian space (?),

$$\frac{1}{\sqrt{|\mathbf{g}|}} \frac{\partial}{\partial \xi_j} \left( m^{jk} \frac{\partial U}{\partial \xi_k} \right) = -\omega^2 s^2 U. \quad (2.3)$$

The first step in developing a generalized RWE wave-equation dispersion relationship is to expand the derivative terms in equation 2.3 and multiply through by  $\sqrt{|\mathbf{g}|}$  to

obtain,

$$\frac{\partial m^{jk}}{\partial \xi_j} \frac{\partial U}{\partial \xi_k} + m^{jk} \frac{\partial^2 U}{\partial \xi_j \partial \xi_k} = -\sqrt{|\mathbf{g}|} \omega^2 s^2 U. \quad (2.4)$$

The derivation of the 3D RWE acoustic wave equation deviates here from that found in ?, who represent the metric tensor with only four independent coefficients. The remaining two independent coefficients are explicitly set to zero in order to satisfy the partially orthogonality restriction. In this development, I follow a more general approach that represents the metric tensor with the full six independent coefficients. This is the key extension developed herein that leads to the greater flexibility in coordinate system design discussed below.

The spatial derivative of the weighted metric tensor in the first term of equation 2.4 is written concisely using the following substitution,

$$n^j = \frac{\partial m^{jk}}{\partial \xi_k} = \frac{\partial m^{j1}}{\partial \xi_1} + \frac{\partial m^{j2}}{\partial \xi_2} + \frac{\partial m^{j3}}{\partial \xi_3}. \quad (2.5)$$

Scalar fields  $n^j$  are interpreted as measures of the rates by which space expands, compresses and/or shears in the  $j^{\text{th}}$  direction and can be non-zero even for orthogonal coordinate systems. Using this substitution, equation 2.4 is rewritten,

$$n^j \frac{\partial U}{\partial \xi_j} + m^{jk} \frac{\partial^2 U}{\partial \xi_j \partial \xi_k} = -\sqrt{|\mathbf{g}|} \omega^2 s^2 U. \quad (2.6)$$

A wave-equation dispersion relation is developed by replacing the partial differential operators acting on wavefield  $U$  with their Fourier domain wavenumber duals (?),

$$(m^{jk} k_{\xi_k} - i n^j) k_{\xi_j} = \sqrt{|\mathbf{g}|} \omega^2 s^2, \quad (2.7)$$

where  $-ik_{\xi_j}$  is the Fourier domain dual of differential operator  $\frac{\partial}{\partial \xi_j}$ . Note that the use of these dual operators is strictly accurate only for the case of constant coefficients. Situations where  $s, m^{jk}, |\mathbf{g}|$ , or  $n^j$  spatially vary lead to a simultaneous spatial and Fourier wavenumber dependence. However, as discussed below, I handle this through multi-coefficient extensions of standard approximations.

Equation 2.7 represents the dispersion relationship required to propagate a wavefield through a generalized 3D Riemannian space. Quantity  $m^{jk}$  in the first term,  $m^{jk}k_{\xi_j}k_{\xi_k}$ , is a measure of the dot product between wavenumber vectors in the  $k_{\xi_j}$  and  $k_{\xi_k}$  directions (i.e. orthogonal wavenumbers will have coefficients  $m^{jk} = 0$  for  $j \neq k$ ). Fields  $n^j$  in the second term,  $in^jk_{\xi_j}$ , represent a scaling of wavenumber  $k_{\xi_j}$  caused by local expansion, contraction and/or shearing of the coordinate system in the  $j^{\text{th}}$  direction.

Note that the expression in equation 2.7 reduces to the more familiar Cartesian expression when introducing  $n^j = 0$  and  $m^{jk} = \delta^{jk}$ :

$$k_{\xi_j}k_{\xi_j} = k_{\xi_1}^2 + k_{\xi_2}^2 + k_{\xi_3}^2 = \omega^2 s^2. \quad (2.8)$$

## Extrapolation wavenumber isolation

Specifying a one-way extrapolation operator requires isolating one of the wavenumbers in equation 2.7. I associate the extrapolation direction with coordinate  $\xi_3$ . Expanding equation 2.7 and evaluating a complete-the-square transform yields an expression for the wavenumber  $k_{\xi_3}$

$$k_{\xi_3} = -a_1k_{\xi_1} - a_2k_{\xi_2} + ia_3 \pm \left[ a_4\omega^2 - a_5^2k_{\xi_1}^2 - a_6^2k_{\xi_2}^2 - a_7k_{\xi_1}k_{\xi_2} + ia_8k_{\xi_1} + ia_9k_{\xi_2} - a_{10}^2 \right]^{\frac{1}{2}}, \quad (2.9)$$

where the non-stationary coefficients,  $a_j$  in equation 2.9, are presented in vector  $\mathbf{a}$ ,

$$\mathbf{a} = \begin{bmatrix} \frac{m^{13}}{m^{33}} & \frac{m^{23}}{m^{33}} & \frac{n^3}{2m^{33}} & \sqrt{\frac{|\mathbf{g}|s}{m^{33}}} & \sqrt{\frac{m^{11}}{m^{33}} - \left(\frac{m^{13}}{m^{33}}\right)^2} & \sqrt{\frac{m^{22}}{m^{33}} - \left(\frac{m^{23}}{m^{33}}\right)^2} & \dots \\ \dots & \left[ \frac{2m^{12}}{m^{33}} - \frac{2m^{13}m^{23}}{(m^{33})^2} \right] & \left[ \frac{n^1}{m^{33}} - \frac{m^{13}n^3}{(m^{33})^2} \right] & \left[ \frac{n^2}{m^{33}} - \frac{m^{23}n^3}{(m^{33})^2} \right] & \frac{n^3}{2m^{33}} \end{bmatrix}^{\mathbf{T}}. \quad (2.10)$$

Note that the coefficients contain globally positive terms  $a_4, a_5, a_6$  and  $a_{10}$  that are squared.

The special Cartesian case is again recovered from the two equations above by

substituting  $n^j = 0$  and  $m^{jk} = \delta^{jk}$  for the coefficients of equation 2.10

$$k_{\xi_3} = [s^2 \omega^2 - k_{\xi_1}^2 - k_{\xi_2}^2]^{\frac{1}{2}}. \quad (2.11)$$

The dispersion relationship specified by equations 2.9 and 2.10 contains ten coefficients that represent mixed-domain fields. For situations where all ten coefficients are constant, for example in Cartesian wavefield extrapolation through homogeneous media, a constant-coefficient Fourier-domain  $(\omega - \mathbf{k}_\xi)$  phase-shift extrapolation scheme can be developed to recursively advance a wavefield from level  $\xi_3$  to level  $\xi_3 + \Delta\xi_3$  (?),

$$U(\xi_3 + \Delta\xi_3, k_{\xi_1}, k_{\xi_2} | \omega) = U(\xi_3, k_{\xi_1}, k_{\xi_2} | \omega) e^{ik_{\xi_3} \Delta\xi_3}. \quad (2.12)$$

If  $U$  represents a post-stack wavefield, an image  $I(\boldsymbol{\xi})$  can be produced from the propagated wavefield by evaluating an imaging condition (?),

$$I(\xi_3, \xi_1, \xi_2) = \sum_{\omega} U(\xi_3, \xi_1, \xi_2 | \omega). \quad (2.13)$$

Situations where coefficients vary across an extrapolation step, though, require further approximations. One straightforward approach is a multi-coefficient split-step Fourier (SSF) method (?). This method uses Taylor expansions of the dispersion relation about a set of reference parameters to form a bulk phase-shift operator in the Fourier domain  $(\omega - \mathbf{k}_\xi)$ . Differences between the reference and true parameters then form a correction term applied in the mixed  $\omega - \boldsymbol{\xi}$  domain. For non-orthogonal coordinate systems described by equations 2.9 and 2.10, I modify the SSF approach of ? as detailed in Appendix B.

The accuracy of the multi-coefficient SSF approach is directly related to the degree to which coefficients in equation 2.10 vary at each propagation step. At a first glance, one might expect that far too many expansions are required to make a PSPI approach practical. (For example, three reference expansions for each of the ten terms would seemingly require  $3^{10} = 59\,049$  separate wavefield extrapolations.) However, three factors combine to greatly reduce the total number of required reference coefficient

sets.

First, the  $a_j$  coefficients in equation 2.9 are highly correlated because they are composed of similar metric tensor elements  $m^{jk}$ . Thus, the central issue is how accurately can we characterize these vector coefficient fields. Coincidentally, this problem is similar to the quantization problem in computer graphics: What is the fewest number of colors by which an image can be represented given a maximum allowable error? To address this issue, I calculate reference coefficients using a multi-dimensional Lloyd's algorithm (?). This iterative procedure represents the multi-dimensional histogram of the coefficients with the sparsest number of points within a specified error tolerance. For further information and examples the reader is directed to ?.

Second, numerous situations exist where some coefficients are zero or otherwise negligible. One approximation is to set all terms containing imaginary numbers to zero, which largely affects only wavefield amplitudes. This kinematic approximation can lead to a mixed-domain fields for a 3D weakly non-orthogonal coordinate system that contains only four coefficients. A second approximation is to zero coefficients that are relatively small. For example, in practice I use the following relationship to determine where non-orthogonal coefficients may be zeroed at any extrapolation step:

$$\hat{m}^{jk} = \begin{cases} 0, & m^{jk} < 0.01 |\min\{m^{11}, m^{22}, m^{33}\}| \\ m^{jk} & \text{otherwise} \end{cases} \quad (2.14)$$

where the circumflex accent  $\hat{g}^{jk}$  denotes approximation. Appendix C details situations where additional approximations are appropriate. Third, one may apply algorithms that locally smooth the coordinate system mesh, which reduces the spatial variability of the coefficients and allows a more reliable representation of wavenumber  $k_{\xi_3}$ .

## NUMERICAL MODELING EXAMPLES

This section presents numerical modeling examples that help validate the above RWE theory. I begin with the two basic 2D analytic examples of sheared Cartesian and polar-ellipsoidal coordinates. I then present a method for generating singularity-free coordinate meshes and illustrate this approach with 2D and 3D Green's function modeling.

### Sheared 2D Cartesian coordinates

An instructive analytic coordinate system to examine is a sheared 2D Cartesian grid formed by a uniform shearing action on a Cartesian mesh (see Figure 2.2a). This

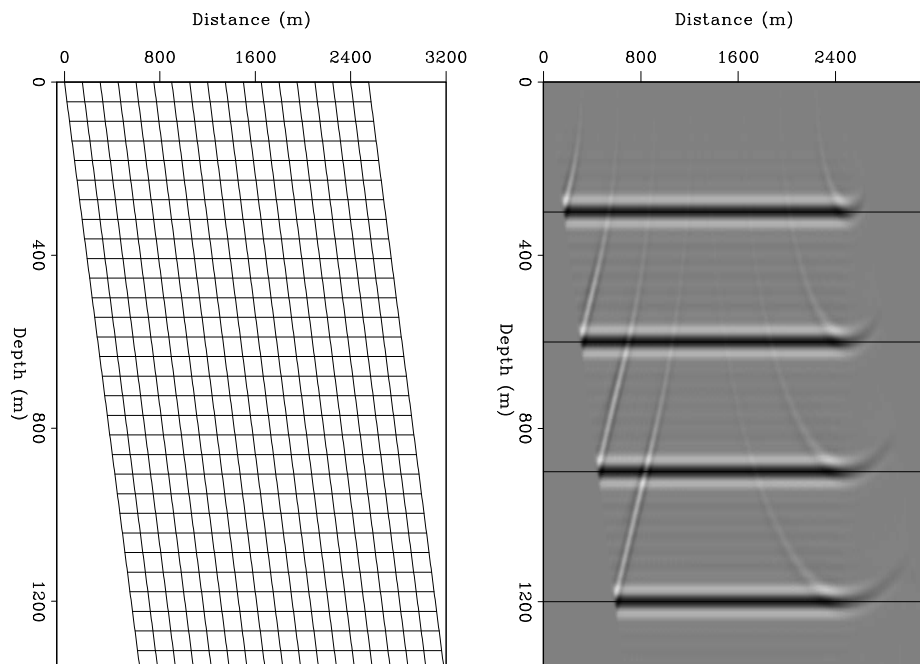


Figure 2.2: Sheared Cartesian coordinate system test. a) Coordinate system shear angle and velocity are  $\theta = 25^\circ$  and  $1500 \text{ ms}^{-1}$ , respectively. b) Zero-offset data consist of four flat plane-wave impulses at  $t=0.2, 0.4, 0.6,$  and  $0.8$  s that are correctly imaged at depths  $z=300, 600, 900,$  and  $1200$  m. **ER** geono/. Fig2

coordinate system is uniquely specified by one additional degree of freedom and is

related to an underlying Cartesian mesh through

$$\begin{bmatrix} x_1 \\ x_3 \end{bmatrix} = \begin{bmatrix} 1 & \sin \theta \\ 0 & \cos \theta \end{bmatrix} \begin{bmatrix} \xi_1 \\ \xi_3 \end{bmatrix}, \quad (2.15)$$

where  $\theta$  is the shear angle of the coordinate system ( $\theta = 0^\circ$  is Cartesian). The metric tensor of this transformation is,

$$[g_{jk}] = \begin{bmatrix} \frac{\partial x_k}{\partial \xi_1} \frac{\partial x_k}{\partial \xi_1} & \frac{\partial x_k}{\partial \xi_1} \frac{\partial x_k}{\partial \xi_3} \\ \frac{\partial x_k}{\partial \xi_1} \frac{\partial x_k}{\partial \xi_3} & \frac{\partial x_k}{\partial \xi_3} \frac{\partial x_k}{\partial \xi_3} \end{bmatrix} = \begin{bmatrix} g_{11} & g_{13} \\ g_{13} & g_{33} \end{bmatrix} = \begin{bmatrix} 1 & \sin \theta \\ \sin \theta & 1 \end{bmatrix}, \quad (2.16)$$

and has a discriminant  $|\mathbf{g}| = \cos^2 \theta$  and a weighted associated metric tensor  $m^{jk}$  given by,

$$[m^{jk}] = \begin{bmatrix} 1 & -\sin \theta \\ -\sin \theta & 1 \end{bmatrix}. \quad (2.17)$$

Because the tensor in equation 2.17 is coordinate invariant, equation 2.6 simplifies to,

$$m^{jk} \frac{\partial^2 U}{\partial \xi_j \partial \xi_k} = -\sqrt{|\mathbf{g}|} \omega^2 s^2 U, \quad (2.18)$$

which generates the following dispersion relation,

$$m^{jk} k_{\xi_j} k_{\xi_k} = \sqrt{|\mathbf{g}|} \omega^2 s^2. \quad (2.19)$$

Expanding out these terms leads to an expression for wavenumber  $k_{\xi_3}$ ,

$$k_{\xi_3} = -\frac{m^{13}}{m^{33}} k_{\xi_1} \pm \sqrt{\frac{|\mathbf{g}| s^2 \omega^2}{m^{33}} - \left( \frac{m^{11}}{m^{33}} - \left( \frac{m^{13}}{m^{33}} \right)^2 \right) k_{\xi_1}^2}. \quad (2.20)$$

Substituting the values of the associated metric tensor in equation 2.17 into equation 2.20 yields,

$$k_{\xi_3} = \sin \theta k_{\xi_1} \pm \cos \theta \sqrt{s^2 \omega^2 - k_{\xi_1}^2}, \quad (2.21)$$

which is appropriate for performing RWE on the sheared 2D Cartesian coordinate system shown in Figure 2.2a.

Figure 2.2b shows the results of extrapolating plane waves in a Cartesian coordinate system sheared at  $\theta = 25^\circ$ . The background velocity model is  $1500 \text{ ms}^{-1}$  and the zero-offset data consist of four flat plane-waves at times  $t=0.2, 0.4, 0.6,$  and  $0.8 \text{ s}$ . Zero-offset migration results generated by equation 2.13 show migrated reflectors at the expected depths of  $x_3=300, 600, 900,$  and  $1200 \text{ m}$ . The propagation generates explainable boundary artifacts. Those on the left are caused by the common edge effect of waves reflecting off the boundary at non-normal incidence. Hyperbolic diffractions on the right arise from propagating truncated plane waves and are independent of the coordinate system. Mitigating these types of artifacts is not difficult, though, because existing techniques in Cartesian wavefield extrapolation craft still apply (e.g. cosine tapers).

## Stretched Polar coordinates

A second example is a stretched polar coordinate system (see Figure 2.3a) appropriate for migrating with turning waves. A stretched polar coordinate system is specified by

$$\begin{bmatrix} x_1 \\ x_3 \end{bmatrix} = \begin{bmatrix} a(\xi_3) \xi_1 \cos \xi_3 \\ a(\xi_3) \xi_1 \sin \xi_3 \end{bmatrix}, \quad (2.22)$$

where coordinate  $\xi_1$  is the radius from the center focus,  $\xi_3$  is polar angle, and  $a = a(\xi_3)$  is a smooth function controlling coordinate system stretch that has curvature parameters  $b = \frac{da}{d\xi_3}$  and  $c = \frac{d^2a}{d\xi_3^2}$ . The metric tensor  $g_{jk}$  for the stretched polar coordinate system defined in equation 2.22 is,

$$[g_{jk}] = \begin{bmatrix} a^2 & \xi_1 a b \\ \xi_1 a b & \xi_1^2 (b^2 + a^2) \end{bmatrix}, \quad (2.23)$$

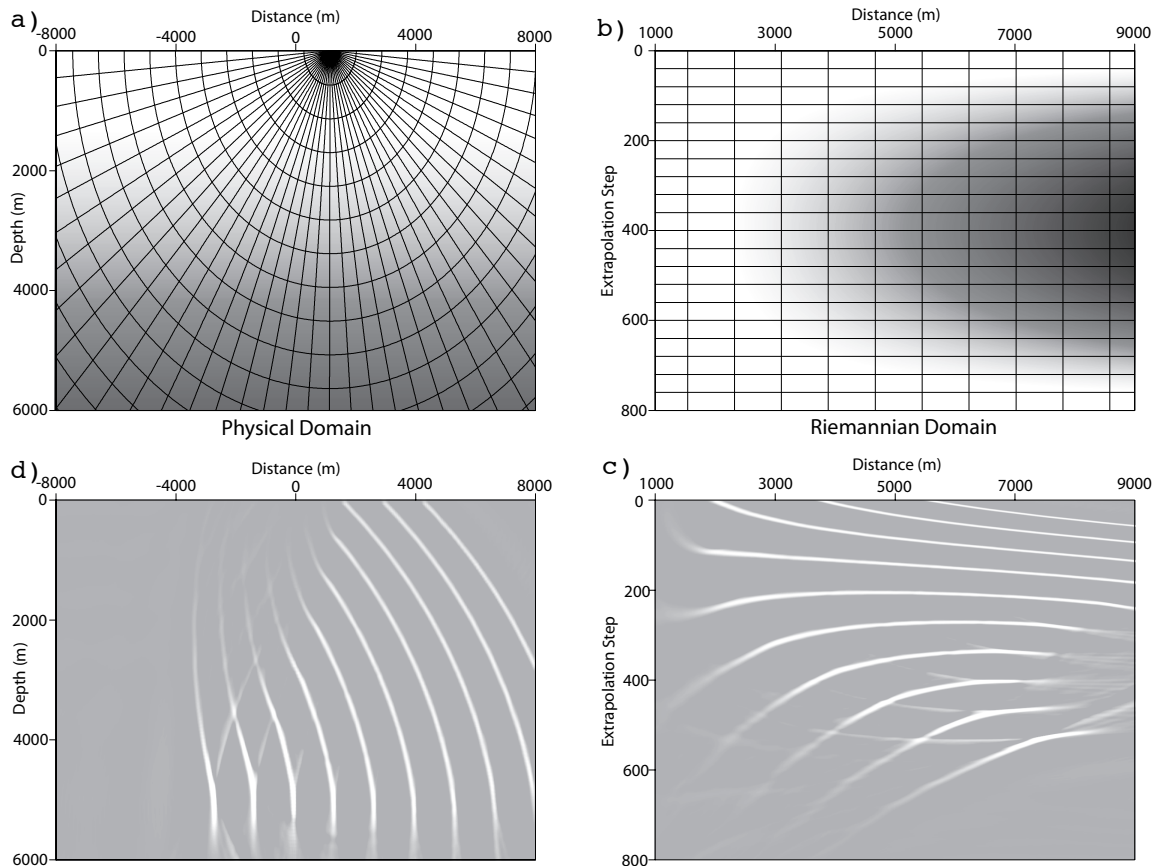


Figure 2.3: Stretched polar coordinate system test example. a) Velocity function  $v(x_3) = 1500 + 0.35x_3$  overlain by a stretched polar coordinate system defined by parameter  $a = 1 + 0.2\xi_3 - 0.05\xi_3^2$ . b) Velocity model mapped in the RWE domain. c) Imaged reflectors in RWE domain. d) RWE domain image mapped to a Cartesian mesh. **ER** geono/. Fig3

and has a metric discriminant given by  $|\mathbf{g}| = a^4 \xi_1^2$ . The weighted associated metric tensor is given by,

$$[m^{jk}] = \begin{bmatrix} \frac{\xi_1(b^2+a^2)}{a^2} & -\frac{b}{a} \\ -\frac{b}{a} & \frac{1}{\xi_1} \end{bmatrix}. \quad (2.24)$$

Tensor  $m^{jk}$  is used to form the extrapolation wavenumber appropriate for one-way wavefield propagation on a 2D polar ellipsoidal mesh. However, because the computational mesh is non-stationary, we must also compute the  $n^j$  fields:  $n^1 = \frac{a^2+2b^2-ac}{a^2}$  and  $n^3 = 0$ . Inserting these values leads to the following extrapolation wavenumber expression (see equations C.7 and C.8),

$$k_{\xi_3} = \frac{\xi_1 b}{a} k_{\xi_1} \pm \sqrt{a^2 \xi_1^2 s^2 \omega^2 - \xi_1^2 k_{\xi_1}^2 - i k_{\xi_1} \xi_1 \left( \frac{a^2 + 2b^2 - ac}{a^2} \right)}. \quad (2.25)$$

The kinematic approximation of equation 2.25 (see equations C.9 and C.10) is

$$\hat{k}_{\xi_3} = \xi_1 \left[ \frac{b}{a} k_{\xi_1} \pm \sqrt{a^2 s^2 \omega^2 - k_{\xi_1}^2} \right], \quad (2.26)$$

and further restricting to the orthogonal polar case that is a circular geometry, where  $a = 1$  and  $b = 0$  (see equations C.13 and C.14), yields,

$$\hat{k}_{\xi_3} = \pm \xi_1 \sqrt{s^2 \omega^2 - k_{\xi_1}^2}, \quad (2.27)$$

which is examined in ?.

Figure 2.3 shows a wavefield extrapolation example for an polar-ellipsoidal coordinate system in equation 2.22 defined by stretch parameter  $a(\xi_3) = 1 + 0.2 \xi_3 - 0.05 \xi_3^2$ . The upper and lower panels of Figure 2.3 correspond to velocity/coordinate and wavefield domains, respectively. Similarly, the left and right panels represent the Cartesian and Riemannian domains. Note that wavefield interpolation between the latter two domains is possible because of the established mapping relationships. Figure 2.3a shows the stretched polar coordinate system mesh overlying a linear  $v(x_3) = 1500 + 0.35x_3 \text{ ms}^{-1}$  velocity function. Figure 2.3b presents the velocity model

mapped into the RWE domain under the transformations defined in equation 2.22.

The test data consist of ten plane waves defined on the surface between 1000 m and 9000 m by ray parameter  $p_x = -0.5 \text{ skm}^{-1}$ . The waves, propagated to greater depths, are no longer planar and pass through a turning point before moving upward to the left (panels 2.3c-d). The wave tops, though, travel through slower material and have not yet overturned. One observation is that if propagating wavepaths can be well represented by a single stretch parameter  $a = a(\xi_3)$ , then a stretched polar mesh could form an effective coordinate basis for plane-wave migration.

## GENERATING SINGULARITY-FREE COORDINATE MESHES

A computational mesh design challenge is generating a RWE coordinate system fairly conformal to the wavefield propagation direction yet unconditionally singularity-free. Panel 2.4a shows a  $v(x_3)$  velocity model with three Gaussian anomaly inclusions overlain by a ray-coordinate system calculated by Huygens' ray-front tracing (?). These anomalies cause both mesh singularities to the left and right of the model as well as a grid rarefaction directly beneath the shot-point.

Panel 2.4b shows the single-valued isochrons of the first-arrival Eikonal equation solution for the same shot-point presented in the top panel. Note that isochrons generally conform to the propagation direction and can be used to construct the extrapolation steps of a RWE computational mesh. The first step in the mesh generation procedure is to extract the initial and final isochron surfaces from the Eikonal equation solution to form the inner and outer mesh boundaries. The mesh domain is then enclosed by interpolating between the edges of the inner and outer bounding surfaces. The interior mesh can then be formed through bi-linear interpolation methods, such as blending functions (??).

Panel 2.4c presents the corresponding singularity-free, but weakly non-orthogonal mesh. The grid is regularly spaced on the outer isochron and has dimples at the

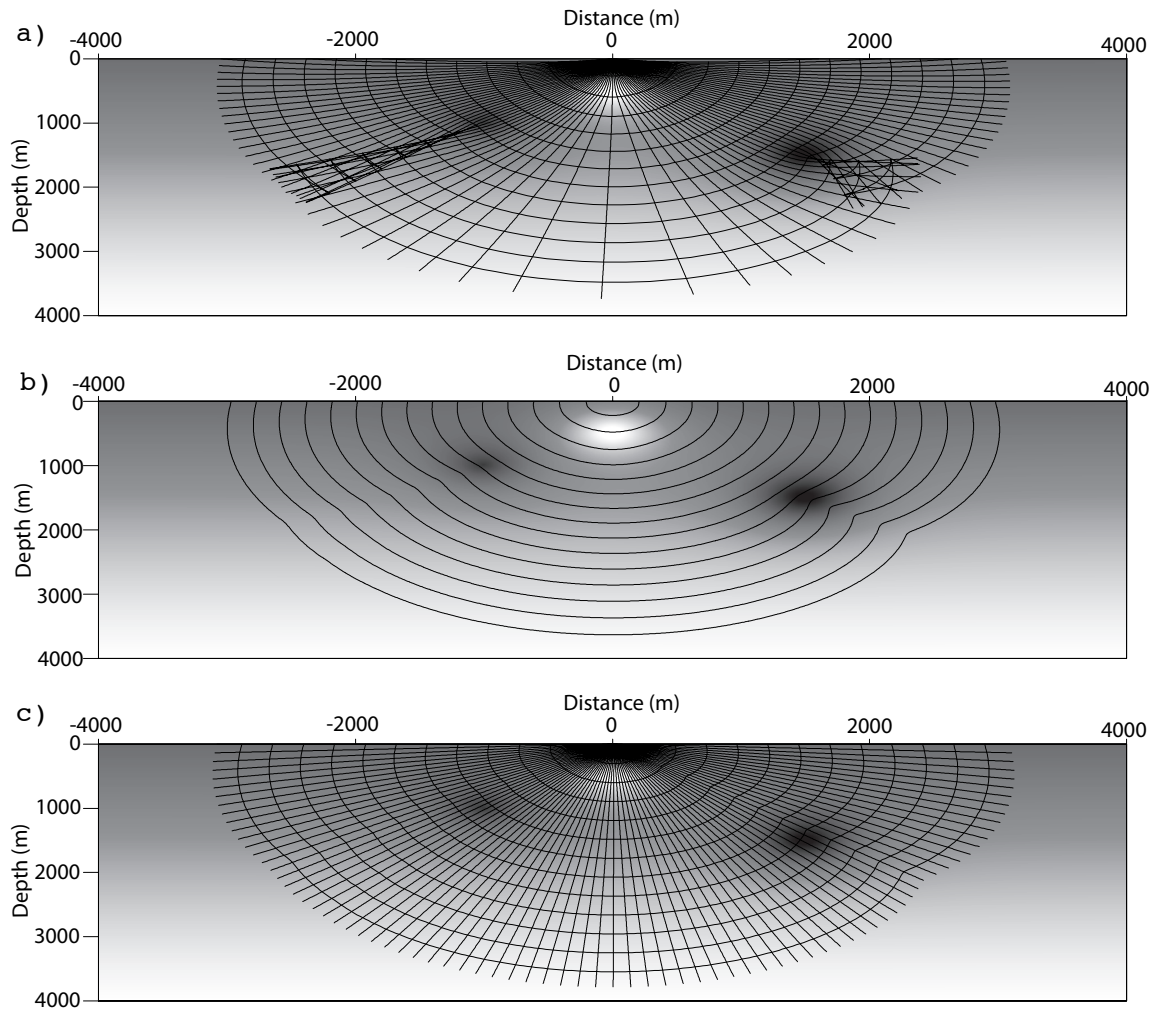


Figure 2.4: Example of singularity-free mesh generation. a) Velocity model with three Gaussian velocity perturbations. Overlain is a coordinate mesh generated from ray-tracing. Note the triplication to either side of the shot-point, as well as the spreading beneath the shot point. b) Velocity model overlain by isochrons of an Eikonal equation solution for same shot-point. c) Singularity-free, but weakly non-orthogonal, computational mesh generated by Eikonal mesh smoothing. NR geono/. Fig4

locations of the removed singularities. These discontinuities have been reduced by applying a smoothing operator to the Eikonal equation solution before calculating the mesh. Importantly, coordinate smoothing usually does not affect propagation accuracy because the coordinate system mesh forms only the skeleton on which wavefield extrapolation occurs. However, for meshes exhibiting rough and/or discontinuous boundaries, even excessive local smoothing cannot generate coefficients that are smooth enough to be accurately represented with standard extrapolation techniques.

## 2D Green's function generation

The third test uses RWE to model 2D Green's functions on coordinate systems constructed by the smoothed Eikonal meshing approach. Figure 2.5 presents a slice through the SEG-EAGE salt velocity model used for the test. Importantly, the contrast between the salt body and sediment velocities leads to complex wavefield propagation including triplication and multi-pathing. Panel 2.5a shows the velocity model with an overlain coordinate system generated by the smoothed Eikonal meshing procedure. The velocity model in the RWE domain is illustrated in panel 2.5b.

Panel 2.5c shows the impulse response tests in the RWE domain. The impulses conform fairly well to the travel-time steps, except where they enter the salt body in the lower left of the image. The migration results mapped back to Cartesian space are shown in panel 2.5d. The complex wavefield to the left of the shot point advances through the salt body and subsequently refracts upward. Note also the presence of wide-angle reflections from the top-salt/sediment interface.

Figure 2.6 presents a comparison test between two-way finite-difference modeling, RWE and Cartesian extrapolation. The three wavefields are fairly similar beneath and to the right of the shot-point except for a  $90^\circ$  phase-change associated with differences between modeling the finite difference and Cartesian point-source in panels 2.6a and 2.6c versus the RWE plane-wave in panel 2.6b. [See ? for a complete explanation of the phase differences associated with line- versus point-source modeling]. These phase-changes were also observed in the polar coordinate examples of ?.

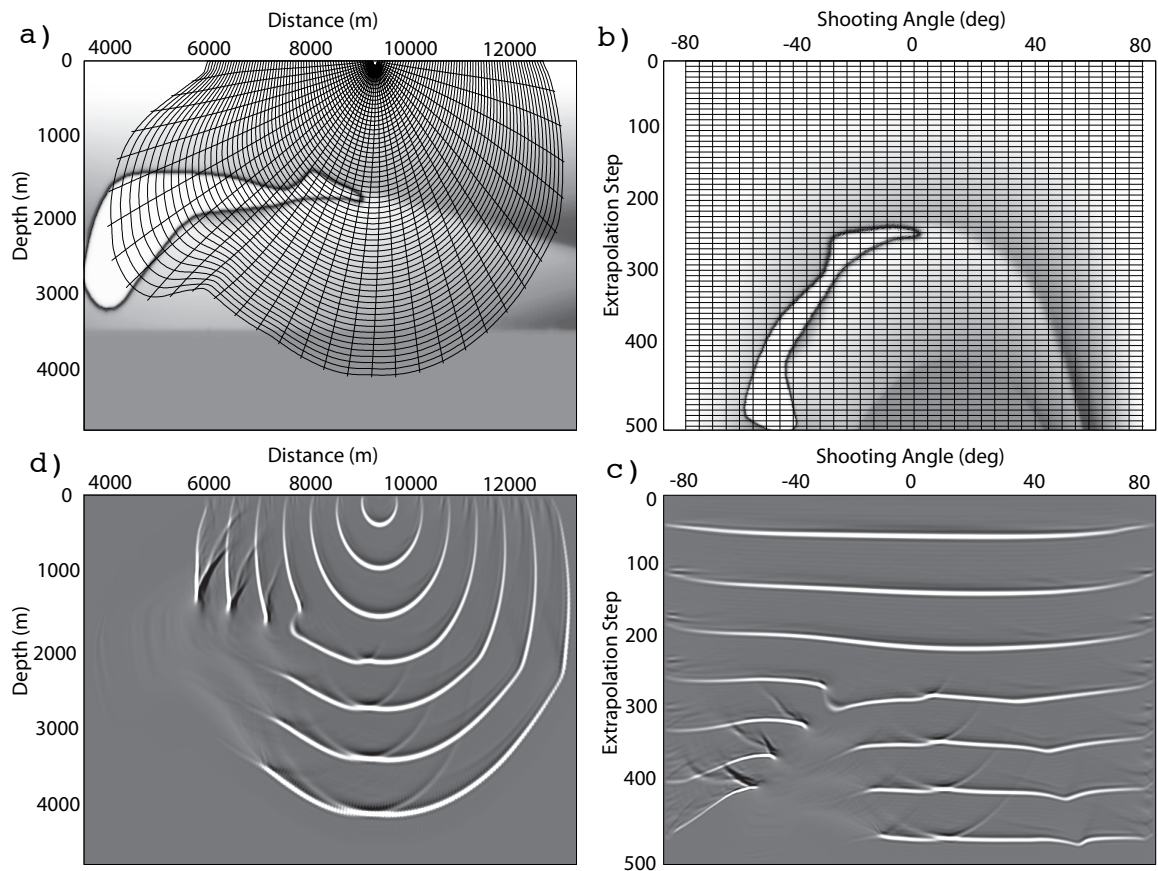


Figure 2.5: Example of wave-equation-generated Green's functions on structured non-orthogonal mesh for a slice through the SEG-EAGE salt velocity model. a) Salt model in physical space with an overlain ray-coordinate mesh. b) Velocity model in the transform domain. c) Wavefield propagated in ray coordinates through velocity model shown in b). d) Wavefield in c) interpolated back to Cartesian space. **ER** `geono/. Fig5`

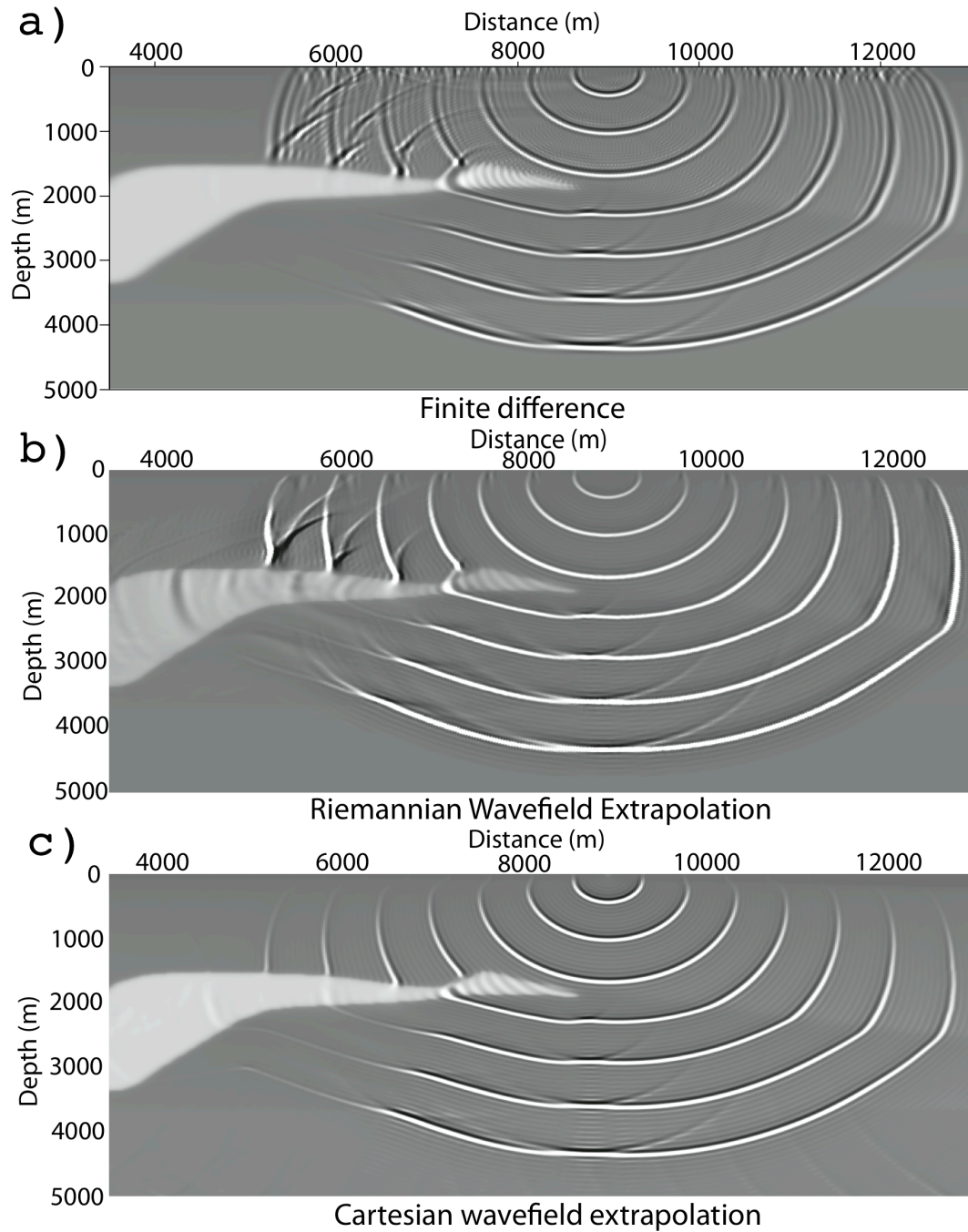


Figure 2.6: Comparison between three different extrapolation methods. a) Two-way finite-difference modeling. b) Riemannian wavefield extrapolation. c) Cartesian wavefield extrapolation. **CR** [geono/. Fig6](#)

However, significant differences are noted to the left of the shot-point. Panels 2.6a-b contain strong reflections from the salt-sediment that are fairly well matched in location. Cartesian-based extrapolation, though, propagates wavefields laterally neither with the same accuracy nor upward at all. Hence, this energy is absent from the propagating wavefield in the lower panel.

Differences in the modeled amplitudes at and above the salt interface in the upper two panels are attributed to differences between the finite-difference modeling and one-way wavefield extrapolation implementations. Finite-difference propagation better models amplitudes in the presence of velocity gradients in the propagation direction. Thus, incident energy is more accurately partitioned at the top sediment-salt interface leading to the lower (and more correct) amplitudes of sub-salt multi-pathed arrivals. The RWE approach underestimates the reflection contribution and allows significantly more energy to be transmitted into and through the salt body. This modeling inaccuracy leads to the more pronounced multi-pathing below the salt body and the more complicated wavefield behavior relative to the Cartesian wavefield example. Incorporating higher-order terms (?) into the RWE formalism, though, would likely diminish the differences between the finite-difference modeling and RWE results.

### 3D analytic coordinates

There are a number of analytic coordinate systems that can be used in various 3D RWE applications (i.e. cylindrical polar, elliptic cylindrical, ellipsoidal coordinates). The optimal choice of coordinate system generally depends on the acquisition geometry of the wavefield to be propagated. For example, line-sources are more conformal in either cylindrical polar or elliptical cylindrical coordinates, while point sources are better matched to ellipsoidal coordinates.

To provide a 3D RWE example, I examine wavefield extrapolation in elliptical-cylindrical coordinates (ECC) (see figure 5.1). This computational mesh forms the basis of the inline delayed-shot migration algorithm detailed in Chapter 5. I set up the extrapolation geometry of the elliptical-cylindrical mesh as follows:

- $\xi_3 \in [0, \infty]$  is the extrapolation direction, where surfaces of constant  $\xi_3$  form concentric elliptic cylinders, shown in Figure 5.1a;
- $\xi_2 \in [0, 2\pi)$  is the cross-line direction, where surfaces of constant  $\xi_2$  are folded hyperbolic planes, shown in Figure 5.1b; and
- $\xi_1 \in [-\infty, \infty]$  is the inline direction, where surfaces of constant  $\xi_1$  are 2D elliptic coordinate meshes, shown in Figure 5.1c.

The mapping relationship between the two coordinate systems is ?

$$\begin{bmatrix} x_1 \\ x_2 \\ x_3 \end{bmatrix} = \begin{bmatrix} \xi_1 \\ a \cosh \xi_3 \cos \xi_2 \\ a \sinh \xi_3 \sin \xi_2 \end{bmatrix}, \quad (2.28)$$

where parameter  $a$  controls the coordinate system breadth.

I conducted elliptic coordinate imaging test results using a 3D Gulf of Mexico velocity model consisting of typical  $v(x_3)$  velocity gradients and a salt body. The source wavefield consisted of five line sources of zero inline dip at times 1.0, 1.5, 2.0, 2.5 and 3.0s. Figure 2.8 presents the ECC and CC imaging test results superposed over the a velocity model with the inline (crossline) axis in the front (side) panel. The ECC image (panel 2.8a) has energy that propagates at steep angles through the salt body in the crossline section, and even overturns to the right-hand side. The CC image (panel 2.8b) contains similar propagation in most locations; however, the high-angle and turning-wave features present in the ECC wavefield are absent because of one-way propagation limitations.

## IMPLEMENTATION COSTS

The introduction of additional mixed-domain coefficients into generally non-orthogonal Riemannian dispersion relationship leads to both increased computation costs and memory requirements. To give an example of the cost overhead of the RWE approach,

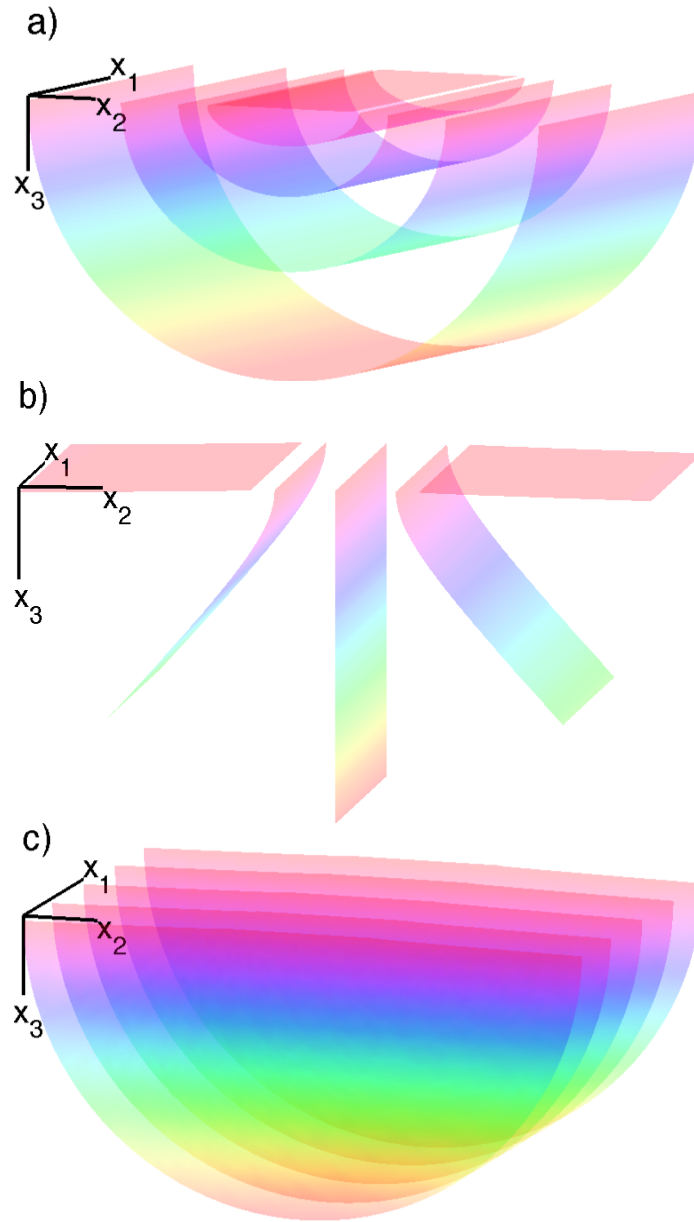


Figure 2.7: Constant surfaces of the elliptic-cylindrical coordinate system Cartesian coordinate axes are given to a) Five constant  $\xi_3$  surfaces forming confocal elliptic cylindrical shells. This represents the direction of extrapolation direction. b) Five constant  $\xi_2$  surfaces representing folded hyperbolic planes. c) Five constant  $\xi_1$  surfaces representing 2D elliptic meshes. **NR** geono/. TECgeom

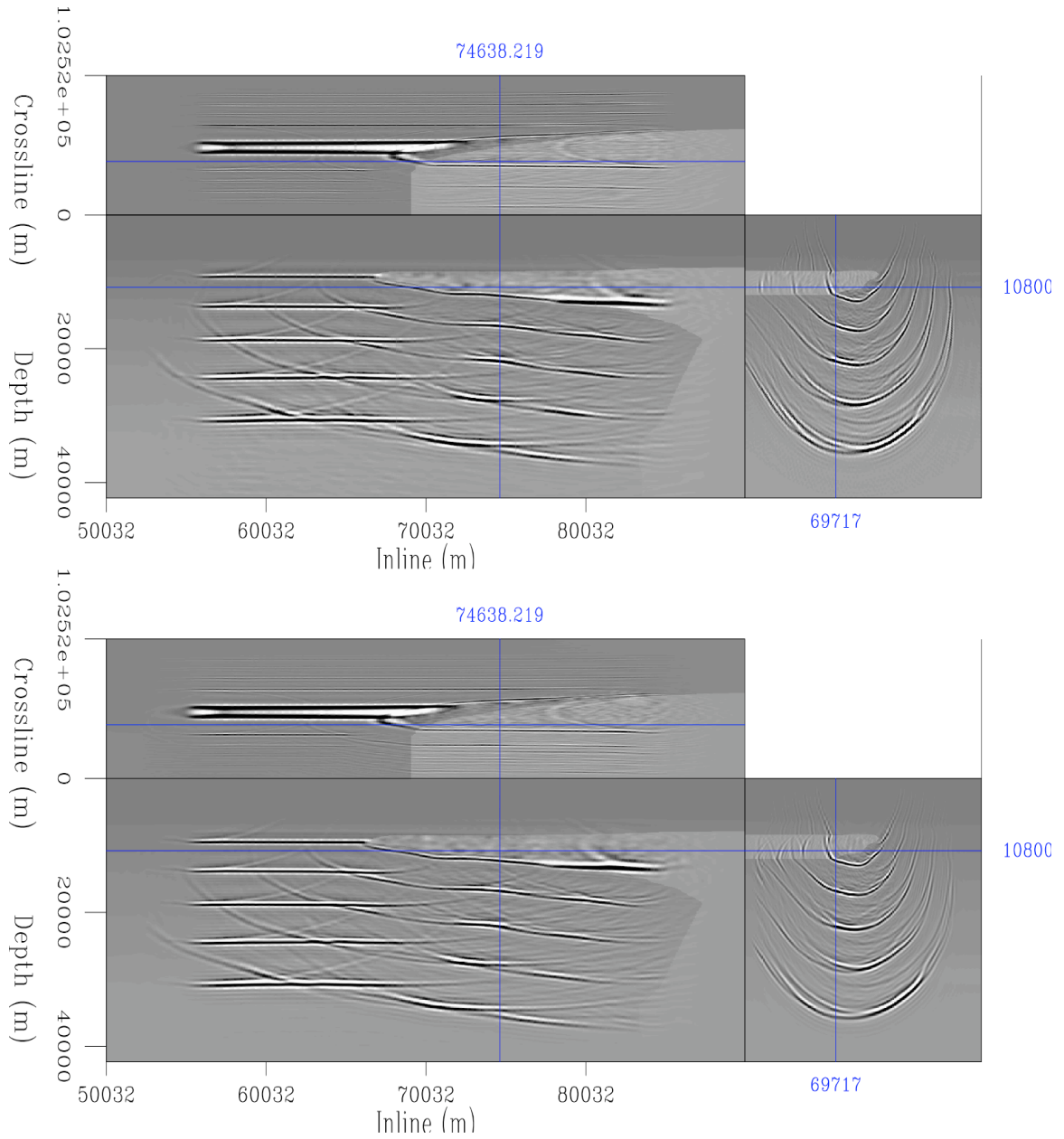


Figure 2.8: Green’s function computation test in the 3D elliptical-cylindrical analytic coordinate system for a set of five flat plane waves at time 1.0 1.5, 2.0, 2.5, and 3.0 s. Top: Elliptical-cylindrical coordinate imaging result. Bottom: Cartesian coordinate imaging result. **CR** `geono/. NewPoint`

Extrapolation Type	Operation	Number of Calls	Total Time (s)	Time per Call (s)
RWE	Frequency Loop	82	55.4	0.676
RWE	Split-step Fourier	41 092	4.2	0.051
RWE	Phase-shift	112 996	17.1	0.209
RWE	Interpolation	112 996	4.6	0.056
Cart	Frequency Loop	82	40.9	0.499
Cart	Split-step Fourier	41 092	2.1	0.026
Cart	Phase-shift	112 996	7.6	0.093
Cart	Interpolation	112 996	4.4	0.054

Table 2.1: Comparison of computational costs of the split-step Fourier and phase-shift subroutines for RWE and equivalent Cartesian implementations. Results computed for the 2D example shown in Figure 2.6.

relative to Cartesian, I benchmarked the algorithm on the 2D computational grid (512x512 samples) used to generate Figure 2.6. Tests were conducted on two codes that differed only in the phase-shift and split-step Fourier subroutines. The RWE code implemented the 2D non-orthogonal extrapolation operator in equation C.9, while the Cartesian implementation used the regular expression (i.e.  $m^{33} = m^{11} = 1$  and  $m^{13} = n^3 = 0$  in equation C.9).

Table 2.1 presents the results of the benchmark testing. A total of 82 frequencies were propagated a total of 511 extrapolation steps requiring 41 092 calls to the SSF operator. The tests involved 112 996 calls to the phase-shift routine, or almost three per extrapolation step as this number varied according to velocity model complexity. The most significant observation is that the RWE algorithm is roughly 1.35x slower than the equivalent Cartesian code. Most of the overhead occurs in the phase-shift and SSF subroutines that are roughly 2.25 and 2.0 times slower, respectively. Whether these costs may be reduced by implementing look-up tables remains an unresolved question. An additional computational overhead is the time required to calculate the geometrical factors  $a_j$  in equation 2.9. This cost, though, can usually be spread over the total number of shots for stationary geometries. Furthermore, the extra cost of

non-orthogonal propagation, relative to that on partially orthogonal mesh, is  $<5\%$  since this affects only phase-shift operation and occurs outside of the more costly square-root calculation.

A second major implementation issue is the memory required to store the non-stationary  $a_j$  coefficients. Holding each additional coefficient in core requires allocating memory equivalent to that of the velocity model, which can become the limiting issue for large 3D models. (For example, a 3D non-orthogonal grid requires an additional 20% memory to store coefficients relative to a partially orthogonal mesh.) Unfortunately, the alternatives to allocating memory, recalculating the  $a_j$  coefficients locally each time or reading them from disk, are inefficient.

## Analytical Coordinates

An alternate approach, discussed in greater detail in Chapters 3-5, is to consider analytic coordinate systems similar to those illustrated in Figures 2.2, 2.3 and 2.8. The main advantage of these coordinate systems that they result in analytically defined extrapolation operators that avoid most problems associated with additional computational and memory overhead costs. The key reason is that all geometric factors can be calculated locally knowing just the local coordinate position using just a few floating point operations. To illustrate this point, I computed four different 3D analytical coordinate migration volumes: one Cartesian and one elliptic cylindrical coordinate image where rays are pre-computed and stored in memory, and one Cartesian and elliptical cylindrical coordinate image where the geometry is computed at run time. The migration geometries were all of the mesh size dimensions: 400x300x500 grid points.

Table 2.2 summarizes the results of the analytic coordinate test migration runs. Overall, the Cartesian coordinate migrations using geometry stored in memory were the fastest. The Cartesian test run using a migration code where the geometry was explicitly recalculated each time ran about 2% slower, but used only 78% of the memory. The elliptical-cylindrical geometry migrations overall ran a little bit slower (2%

Mig. Type	Geometry	Run Time (s)	Relative Run Time	Max Memory Usage (Gb)	Relative Memory Usage
CC	Stored	1304	1.00	3.3	1.000
CC	Calculated	1333	1.022	2.6	0.788
EC	Stored	1330	1.020	3.4	1.030
EC	Calculated	1380	1.058	2.7	0.812

Table 2.2: Comparison between performing migration with stored or locally computed coordinate system geometry information for Cartesian (CC) and Elliptic Cylindrical (EC) coordinates.

and 6% for stored and recalculated geometries, respectively). However, the migrations used little extra memory relative to the Cartesian geometry runs. Overall, the test results illustrate the significant implementation advantages afforded by analytic coordinate systems with respect to run time and memory requirements. In the following chapters, I will build upon these advantages to help implement 2D and 3D prestack migration algorithms.

## CONCLUSIONS

This chapter addresses existing issues with Riemannian wavefield extrapolation theory by extending RWE to smoother, but non-orthogonal, coordinate systems. I demonstrate that acoustic wave equations can be generated in general 3D Riemannian spaces, and that the corresponding extrapolation wavenumber decouples from the other wavenumbers. Using extensions to the PSPI and SSF approximation techniques, I incorporate this wavenumber into a one-way extrapolation operator appropriate for propagating wavefields. I present a method for generating computational meshes that are unconditionally singularity-free, which is used to generate examples illustrating wavefield propagation on non-orthogonal coordinate meshes using RWE operators. Finally, I argue that analytic coordinate systems afford the possibility of more accurate extrapolation operators implementations, which opens up a range of

imaging possibilities including shot-profile migration in elliptic coordinates (Chapter 3), the calculation of angle-domain common-image gathers in generalized coordinates (Chapter 4) and inline delayed-shot migration in tilted elliptical-cylindrical coordinates (Chapter 5).

## ACKNOWLEDGMENTS

I acknowledge the contributions of Paul Sava and Sergey Fomel in laying the groundwork for the current theory and for ongoing RWE conversations, and I thank Biondo Biondi, Bob Clapp, Brad Artman, Paul Fowler, Tom Dickens, and Peter Traynin for enlightening discussions. I also acknowledge the reviewers of the Geophysics manuscript and thank them for their helpful comments.

## Chapter 3

# Shot-profile migration in elliptical coordinates

This chapter extends the Riemannian wavefield extrapolation (RWE) approach developed in Chapter 2 to 2D prestack migration using elliptical coordinate systems. I show that the corresponding 2D elliptical extrapolation wavenumber introduces only an isotropic slowness model stretch to the single-square-root operator. This enables the use of existing Cartesian finite-difference extrapolators for propagating wavefields on elliptical meshes. A post-stack migration example illustrates the advantages of elliptical coordinates for imaging with turning waves. A 2D imaging test using a velocity benchmark data set demonstrates that the RWE prestack migration algorithm generates high-quality migration images that are more accurate than those generated by Cartesian operators of the equivalent accuracy. I note that even in situations where RWE geometries are employed, a high-order implementation of the one-way extrapolator operator is required for accurate propagation and imaging. The results of this chapter are published as ?.

## INTRODUCTION

Wave-equation migration techniques based on one-way extrapolators are often used for accurate imaging of complex geologic structures. Most conventional downward continuation approaches, though, are unable to handle the steeply propagating or turning-wave components often important for imaging areas of interest. A number of novel imaging approaches address these issues through a judicious decomposition of recorded wavefields [e.g. plane-wave migration (?)], partial and complete propagation-domain decomposition [e.g. Gaussian beam migration (?) and Riemannian wavefield extrapolation (??), respectively], or a combination thereof [e.g. plane-wave migration in tilted coordinates (?)]. These techniques have overcome many, though not all, issues in the practical application of one-way extrapolation operators.

Riemannian wavefield extrapolation (RWE) is a method for propagating wavefields on generalized coordinate meshes. The central idea of RWE is to transform the computational domain from Cartesian to a geometry where the extrapolation axis is oriented along the general wavefield propagation direction. Ideally, solving the corresponding one-way extrapolation equations in the transform domain leads to the bulk of wavefield energy being propagated at angles relatively near to the extrapolation axis, thus improving the global extrapolation accuracy. One obvious application is generating high-quality Green's functions for point-sources in a dynamic coordinate system, where a suite of rays is first traced through a velocity model and then used as the skeleton on which to propagate wavefields (see Chapter 1).

Although the full-domain decomposition approach naturally adapts to propagation in a point-source ray-coordinate system, two unresolved issues make it difficult to apply RWE efficiently in prestack shot-profile migration algorithms. First, receiver wavefields in shot-profile migration are usually broadband in plane-wave dip spectrum and cannot be easily represented by a single coordinate system (i.e. reflections from opposing dips propagate in opposing directions). Second, the optimal meshes for the source and receiver wavefields usually do not share a common geometry. For example, a polar coordinate system is well-suited for propagating source wavefields, while

elliptical meshes are more appropriate for receiver wavefields. This factor is detrimental to algorithmic efficiency where images are generated by correlating source and receiver wavefields: by existing on different grids they must both be interpolated to a common Cartesian reference frame prior to imaging. This leads to a significant number of interpolations, which leaves the algorithm computationally unattractive, except in target-oriented imaging situations.

The main goal of this chapter is to specify a single coordinate system that enables the accurate propagation of large-angle and turning-wave components of both the source and receiver wavefields. I demonstrate that an elliptical coordinate system forms a natural computational grid for prestack shot-profile migration and has useful geometric properties that facilitate numerical implementation. An elliptical coordinate system originates on the horizontal acquisition surface and steps outward as a series of ellipses. Thus, the coordinate system expands in a radial-like manner appropriate for computing accurate point-source Green's functions while allowing the dipping plane-wave components in the receiver wavefield to propagate at large angles to either side of the acquisition surface. One consequence of using a 2D elliptical coordinate system is that the corresponding extrapolation operator must be modified; however, I show that elliptical geometry introduces only an isotropic velocity model stretch. Existing high-order implicit Cartesian finite-difference extrapolation operators with accuracy up to  $80^\circ$  from the extrapolation axis (?) can be used to propagate wavefields, readily enabling accurate imaging of large-angle and turning waves at a cost competitive with that of Cartesian downward continuation.

This chapter begins with a discussion of why elliptical meshes are a natural coordinate system choice for shot-profile prestack depth migration (PSDM). I develop an extrapolation wavenumber appropriate for wavefield propagation on 2D elliptical coordinate systems. I then present post-stack and prestack migration examples that illustrate the scheme's ability to image steep structure using turning waves. The chapter concludes with a discussion on the advantages of analytic coordinate systems relative to more dynamically generated meshes.

## ELLIPTIC COORDINATE EXTRAPOLATION

Generating an effective RWE coordinate system for prestack migration requires appropriately linking mesh geometry with wavefield propagation kinematics. Figure 4.1 illustrates this concept for an idealized shot-profile imaging experiment through a medium of constant slowness  $s$ . Here, I specify source and receiver wavefields ( $S$  and  $R$ ) as impulses at source position and time  $[\mathbf{x}_s, \tau_s = 0]$  and at receiver position and time  $[\mathbf{x}_r, \tau_r = \tau]$ , where  $\tau$  is an arbitrary time lag. The wavefields expand outward as spherical wavefronts (dashed lines) according to

$$S(\mathbf{x}_s, \mathbf{x}|t) = \delta(t - s \|\mathbf{x} - \mathbf{x}_s\|) \quad \text{and} \quad R(\mathbf{x}_r, \mathbf{x}|t) = \delta(t - \tau + s \|\mathbf{x} - \mathbf{x}_r\|), \quad (3.1)$$

where  $\|\mathbf{x}\|$  is the Euclidean norm of the vector  $\mathbf{x}$  and  $s$  is slowness. An image  $I(\mathbf{x})$  can be generated by applying a correlation imaging condition at  $t = 0$  (?),

$$I(\mathbf{x}) = \delta(\tau - s(\|\mathbf{x} - \mathbf{x}_r\| + \|\mathbf{x} - \mathbf{x}_s\|)), \quad (3.2)$$

which is the equation of an ellipse (solid line).

This suggests a natural correspondence between an elliptical coordinate system and the prestack migration isochrons for a constant velocity model. One can observe this in Figure 4.1a by how well the isochron image conforms to the underlying coordinate mesh. In this example, I intentionally did not fix the locations of the elliptical mesh foci relative to  $\mathbf{x}_s$  and  $\mathbf{x}_r$ . Adjusting these points will alter both the elliptical mesh and how well it conforms to the isochrons. These parameters represent two degrees of freedom that allow better tuning of mesh geometry to the bulk propagation direction.

## The Helmholtz equation in elliptical coordinates

As demonstrated in Chapter 2, propagating a wavefield  $U$  in generalized coordinates requires encoding the mesh geometry directly into the one-way extrapolation equations (??). Hence, deriving an elliptical-coordinate extrapolation operator requires introducing elliptical geometry into the Laplacian operator  $\nabla^2$  of the Helmholtz equation,

$$\nabla^2 U + \omega^2 s^2 U = 0. \quad (3.3)$$

where  $U$  is either a source or receiver wavefield. I begin with the definition of the analytic transformation between the elliptical and Cartesian coordinate systems (?),

$$\begin{bmatrix} x_1 \\ x_3 \end{bmatrix} = \begin{bmatrix} a \cosh \xi_3 \cos \xi_1 \\ a \sinh \xi_3 \sin \xi_1 \end{bmatrix}, \quad (3.4)$$

where  $\mathbf{x} = [x_1, x_3]$  are the underlying Cartesian coordinate variables,  $\boldsymbol{\xi} = [\xi_1, \xi_3]$  are the RWE elliptical coordinates defined on the intervals  $\xi_1 \in [0, \pi)$ , and  $\xi_3 \in [0, \infty]$ , and  $a$  is a stretch parameter controlling coordinate system breadth. Herein,  $x_2 = \xi_2 = 0$  are assumed. As illustrated in Figure 4.1, lines of constant  $\xi_3$  represent ellipses, while those of constant  $\xi_1$  form hyperbolas. Figure 4.1 illustrates the angle convention used herein, where  $\theta(\boldsymbol{\xi})$  represents the angle between the elliptical extrapolation direction and the vertical axis of the Cartesian coordinate system. Additional information on the physical interpretation of elliptical coordinates is presented in Appendix D.

The metric tensor ( $g_{jk} = \frac{\partial x_l}{\partial \xi_j} \frac{\partial x_l}{\partial \xi_k}$  with an implicit sum over index  $l$ ) describing elliptical coordinates is

$$[g_{jk}] = \begin{bmatrix} A^2 & 0 \\ 0 & A^2 \end{bmatrix}, \quad (3.5)$$

where  $A = a\sqrt{\sinh^2 \xi_3 + \sin^2 \xi_1}$ . The metric tensor determinant,  $|\mathbf{g}| = A^4$ , is required to specify the weighted metric tensor,  $m^{jk}$ ,

$$[m^{jk}] = \begin{bmatrix} 1 & 0 \\ 0 & 1 \end{bmatrix}. \quad (3.6)$$

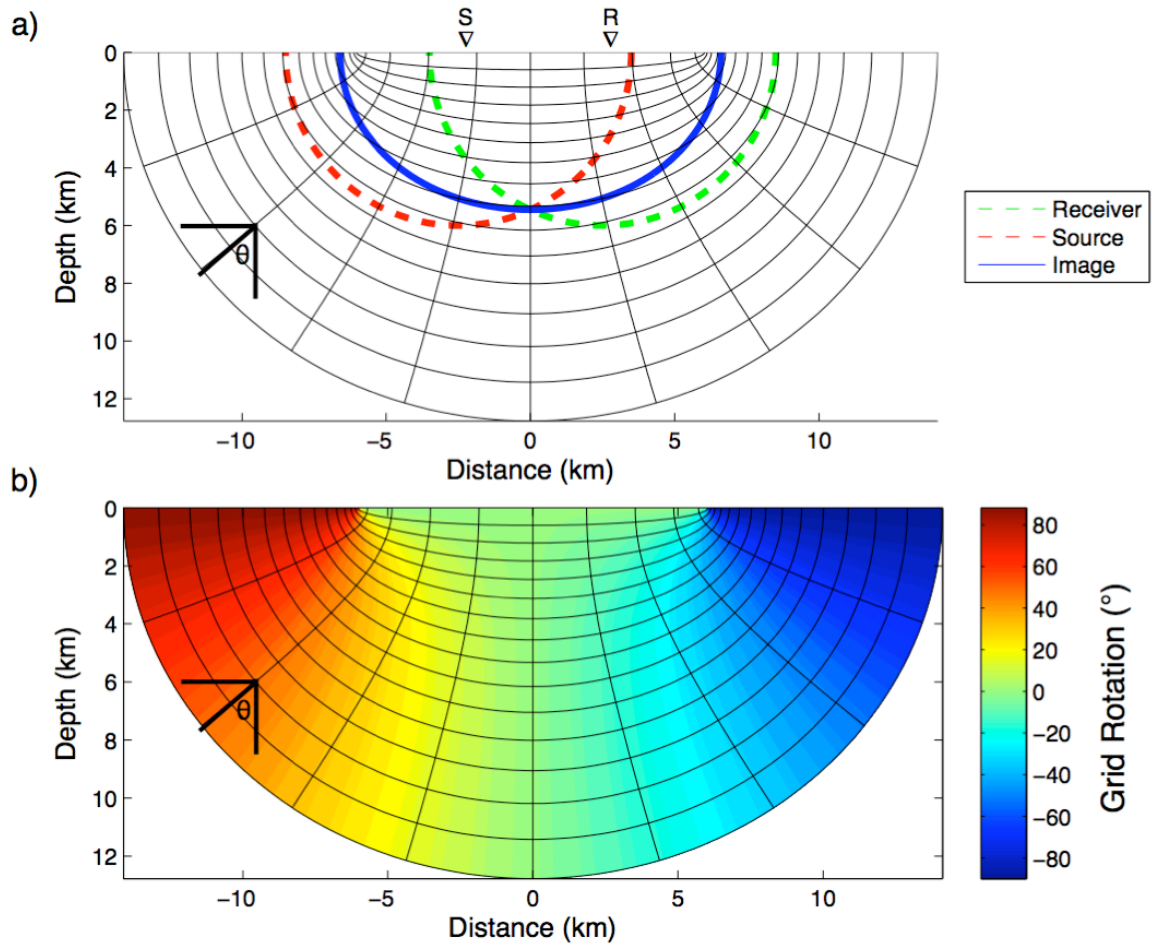


Figure 3.1: Illustrating the elliptical coordinate system. a) Constant-velocity imaging experiment with point source and receiver wavefields (dashed lines) from locations marked  $S$  and  $R$ , respectively. The corresponding image is an elliptical isochron surface derived by cross-correlating the source and receiver wavefields (solid line). b) Grid rotation angles for the elliptical coordinate system with respect to the vertical Cartesian depth axis. NR georwe/. Figure1

Importantly, the weighted metric tensor  $m^{jk}$  in equation 3.6 is an identity matrix, indicating that the transformation in equation 3.4 causes space to contract or dilate isotropically.

Following the development in Chapter 2, I insert the tensor components in equations 3.6 into the standard expression for the Laplacian operator (?),

$$\nabla^2 = \frac{1}{\sqrt{|\mathbf{g}|}} \frac{\partial}{\partial \xi_j} \left( m^{jk} \frac{\partial}{\partial \xi_k} \right), \quad (3.7)$$

which leads to the elliptical coordinate Laplacian operator,

$$\nabla^2 = \frac{1}{A^2} \left( \frac{\partial^2}{\partial \xi_1^2} + \frac{\partial^2}{\partial \xi_3^2} \right). \quad (3.8)$$

The elliptical coordinate Helmholtz equation is derived by introducing equation 3.8 into equation 3.3 and rearranging terms to yield

$$\left[ \frac{\partial^2}{\partial \xi_1^2} + \frac{\partial^2}{\partial \xi_3^2} \right] U + A^2 \omega^2 s^2 U = 0. \quad (3.9)$$

Defining an effective slowness field  $s_{eff} = As$  changes the above to

$$\left[ \frac{\partial^2}{\partial \xi_1^2} + \frac{\partial^2}{\partial \xi_3^2} \right] U + \omega^2 s_{eff}^2 U = 0. \quad (3.10)$$

Equation 3.10 is the most important result in Chapter 2: elliptical coordinates introduce only an isotropic slowness model stretch in the Helmholtz equation.

## Dispersion relation in elliptical coordinates

Deriving an elliptical-coordinate dispersion relation from equation 3.10 proceeds in the usual manner (?). The following 2D development uses a convention where  $\xi_3$  and  $\xi_1$  are the extrapolation direction and orthogonal coordinate, respectively. Replacing

the partial differential operators with their Fourier domain duals, gives

$$k_{\xi_1}^2 + k_{\xi_3}^2 = \omega^2 s_{eff}^2, \quad (3.11)$$

and isolating the  $k_{\xi_3}$  wavenumber contributions leads to a wavefield extrapolation operator for recursive outward stepping in concentric ellipses in the  $\xi_3$  direction,

$$U(\xi_3 + \Delta\xi_3, k_{\xi_1} | \omega) = U(\xi_3, k_{\xi_1} | \omega) e^{\pm i \Delta\xi_3 k_{\xi_3}} = U(\xi_3, k_{\xi_1} | \omega) e^{\pm i \Delta\xi_3 \sqrt{\omega^2 s_{eff}^2 - k_{\xi_1}^2}}, \quad (3.12)$$

where  $\Delta\xi_3$  is the extrapolation step size, and  $\pm$  determines whether a wavefield is propagating causally or acausally (i.e. source and receiver wavefields, respectively).

The dispersion relation in equation 3.12 will not be an exact expression in general because  $s_{eff}$  varies spatially. This situation is similar to that in Cartesian wavefield extrapolation in laterally varying media, and equation 3.12 can be easily implemented with existing Cartesian extrapolation schemes (e.g. finite differences, PSPI) using an effective slowness model  $s_{eff} = As$ .

An additional question worth addressing is to which angle is propagation in elliptical coordinates accurate? Because the geometric effects of elliptical coordinates can be incorporated into an effective slowness model,  $s_{eff}$ , the local angular accuracy for finite-difference propagation is equivalent to that of the Cartesian-domain implementation. Globally, though, the maximum propagation angle for a given extrapolation accuracy depends on the orientation of the local extrapolation axis. Figure 4.1b illustrates how the angle of the extrapolation axis,  $\theta = \theta(\boldsymbol{\xi})$ , locally changes in elliptical coordinates with respect to the Cartesian depth axis. The following examples were generated with  $\pm 80^\circ$  finite-difference propagators (?), and will have a maximum extrapolation angle equal to  $\theta(\boldsymbol{\xi}) \pm 80^\circ$ .

## Prestack migration algorithm

The expression in equation 3.12 can be extended to prestack migration. An initial step is defining the foci locations of the elliptical coordinate system. Unfortunately,

choosing the optimal location, relative to the acquisition geometry (i.e. the source and farthest-offset receiver locations), is not straightforward. For example, situating foci too close together pulls the wavefields towards the focus because the local extrapolation axis angle rapidly becomes steep (c.f. Figure 4.1b). In contrast, placing foci too distant from each other leads to a near-rectilinear coordinate system that affords little improvement over Cartesian extrapolation. I determined heuristically that optimal foci locations are an additional 10–20% (of the aperture length) beyond the source point and farthest receiver offset.

The remaining prestack migration algorithmic steps are:

1. Specify a shot-specific elliptical coordinate system for source location  $s_l$ , and interpolate the Cartesian velocity model to this mesh;
2. Generate the shot-specific image,  $I(\boldsymbol{\xi}|s_l)$ , in the elliptical coordinate system at step  $\xi_3$  from the source,  $S$ , and receiver,  $R$ , wavefields

$$I(\boldsymbol{\xi}|s_l) = \sum_{\omega} \Re [S^*(\boldsymbol{\xi}|\omega, s_l)R(\boldsymbol{\xi}|\omega, s_l)]; \quad (3.13)$$

3. Propagate source and receiver wavefields (for all frequencies) by a step  $\Delta\xi_3$

$$\begin{aligned} S(\xi_3 + \Delta\xi_3, k_{\xi_1}|\omega, s_l) &= S(\xi_3, k_{\xi_1}|\omega, s_l) e^{+i\Delta\xi_3 k_{\xi_3}}, \\ R(\xi_3 + \Delta\xi_3, k_{\xi_1}|\omega, s_l) &= R(\xi_3, k_{\xi_1}|\omega, s_l) e^{-i\Delta\xi_3 k_{\xi_3}}; \end{aligned} \quad (3.14)$$

4. Repeat steps 2-3 until reaching the end of the elliptical coordinate mesh;
5. Interpolate the single-shot, elliptical-coordinate image  $I(\boldsymbol{\xi}|s_l)$  to Cartesian coordinates and update the global Cartesian image  $I(\mathbf{x})$ ; and
6. Repeat steps 1-5 for all shot locations.

## 2D MIGRATION TESTS

This section presents 2D test results for a post-stack turning-wave and the prestack velocity benchmark (?) data sets. I propagate all wavefields with the one-way extrapolators described in ? on an elliptical coordinate system defined by equation 3.4 assuming effective slowness fields  $s_{eff} = As$ . Imaging results are generated using post-stack and shot-profile migration algorithms employing the recursive extrapolation relations in equations 3.12 and 3.14, respectively. Image volumes in elliptical coordinates are transformed back to the Cartesian domain using sinc interpolation. The extra computational cost of generating the RWE migration results, relative to those in Cartesian imaging, is roughly two additional interpolations per shot: one for the Cartesian velocity model to the elliptical mesh, and another for the elliptical image to the Cartesian grid.

### Post-stack migration example

The first elliptical coordinate migration example uses the post-stack data set shown in Figure 4.2. The data were generated from an adapted Sigsbee model, shown in

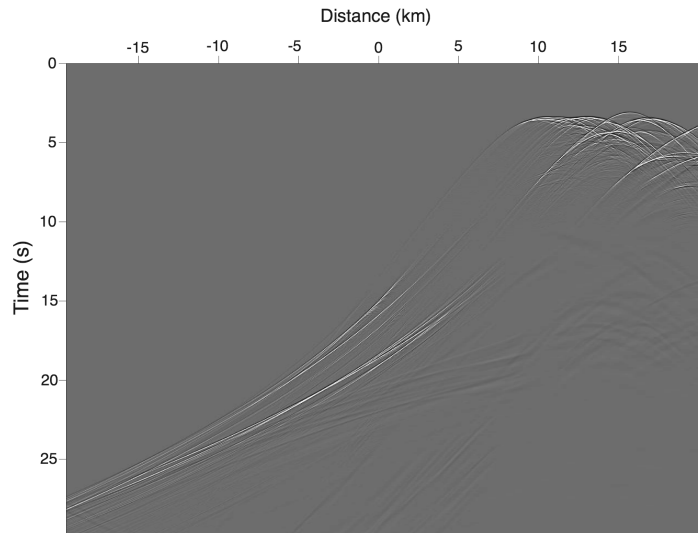


Figure 3.2: Post-stack turning-wave data generated by two-way time-domain finite-difference modeling from all salt body edges of the velocity model in Figure 4.3a. **ER** georwe/. Figure2

Figure 4.3a, using exploding reflector (two-way time-domain FD) modeling from all

salt body edges (?). The imaging test involved only the turning components of the wavefield shown in Figure 4.2. Figure 4.3a also presents the experimental geometry for

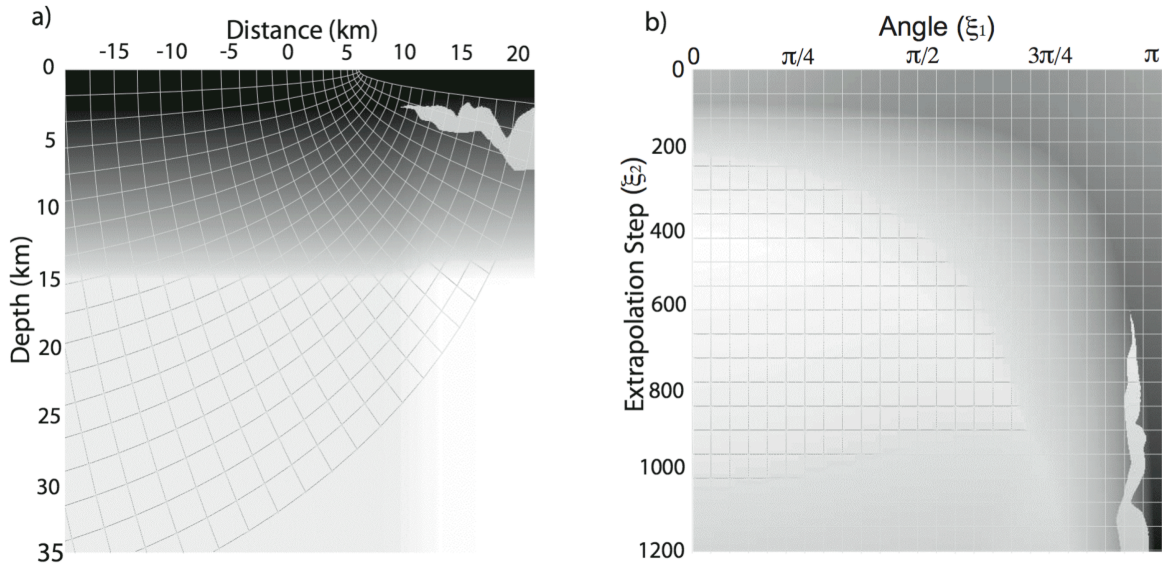


Figure 3.3: Post-stack turning-wave model. a) Velocity model used to generate turning wave data in Figure 4.2 with coordinate system overlain. b) Effective slowness model  $s_{eff}$  in elliptical coordinates. **ER** georwe/. Figure3

the coordinate system with foci situated at -90 km (not shown) and 5 km. Because the wavefield propagation directions are largely known, I chose foci locations that ensured a conformal grid. (I recognize that this example is a special case where the dip field is oriented largely in one direction.) Figure 4.3b shows the effective slowness model,  $s_{eff}$ , in the transformed coordinate system parameterized by extrapolation step and surface take-off position axes.

Figure 4.4 presents the results for migration in the chosen RWE elliptical coordinates. Panel 4.4a shows the monochromatic post-stack migration result with the elliptical coordinate system overlain. Note that the monochromatic wavefields illustrate that the propagation paths of wavefield energy are fairly conformal to the elliptical coordinate mesh. This demonstrates that post-stack migration in elliptical coordinates can successfully propagate turning waves, which, in this case, arrive at normal incidence to the salt flank as expected for exploding-reflector modeling. Panel 4.4b

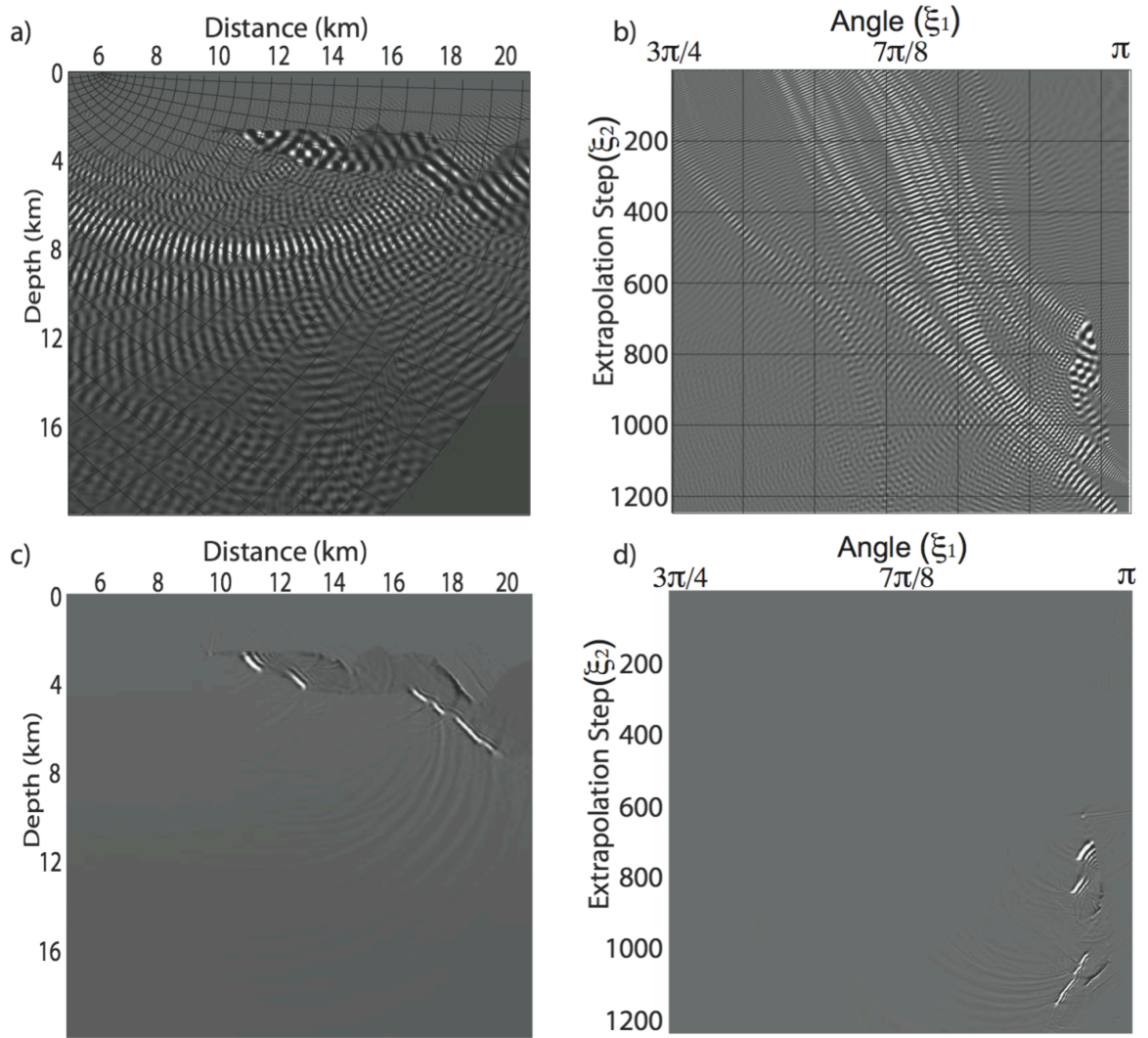


Figure 3.4: Post-stack turning-wave migration results. a) Monochromatic Cartesian image with overlain elliptical coordinates showing the wave-propagation paths. b) Monochromatic elliptical coordinate image. c) Broadband Cartesian image. d) Broadband elliptical coordinate image. **CR** georwe/. Figure4

shows the elliptical-coordinate version of the image in panel 4.4a at successive extrapolation steps, and illustrates that wavefield energy propagates at large angles relative to the extrapolation axis. Panels 4.4c and 4.4d show the broadband images for Cartesian and elliptical coordinate systems, respectively. The salt flanks beneath the salt nose are accurately positioned, demonstrating the potential for imaging with turning waves in elliptical coordinates using large-angle extrapolation operators.

### Prestack migration example

I performed a prestack elliptical coordinate migration test using a velocity benchmark model (Figure 4.5a). Full data offsets were not used for each shot; rather, I used a 10 km initial migration aperture to enable more accurate propagation of turning waves within the propagation domain. I located the foci for each migrated shot an additional 15% (of the 10 km acquisition aperture) beyond the shot point and the farthest receiver offset. Panel 4.5b shows the effective slowness model,  $s_{eff}$ , in the elliptical coordinate system. The elliptical mesh is again parameterized by extrapolation step and surface take-off position axes. Importantly, the steep salt body structure to the right becomes relatively low angle under this coordinate transformation, and should be better imaged in elliptical coordinates.

Figure 4.6 presents the prestack migration results for the elliptical coordinate system. Panel 4.6a shows the RWE shot-profile migration result in elliptical coordinates, while panel 4.6b presents the corresponding Cartesian image generated by finite-difference operators of equivalent accuracy. (Note that slightly different source wavelets were used leading to a phase rotation between the two images.) The salt body to the left is well-imaged in most areas in both images, though is improved, for example, in the circled location in elliptical coordinates. The salt body flanks to the right (circled locations), illuminated largely by turning and prismatic waves, are better imaged in elliptical coordinates.

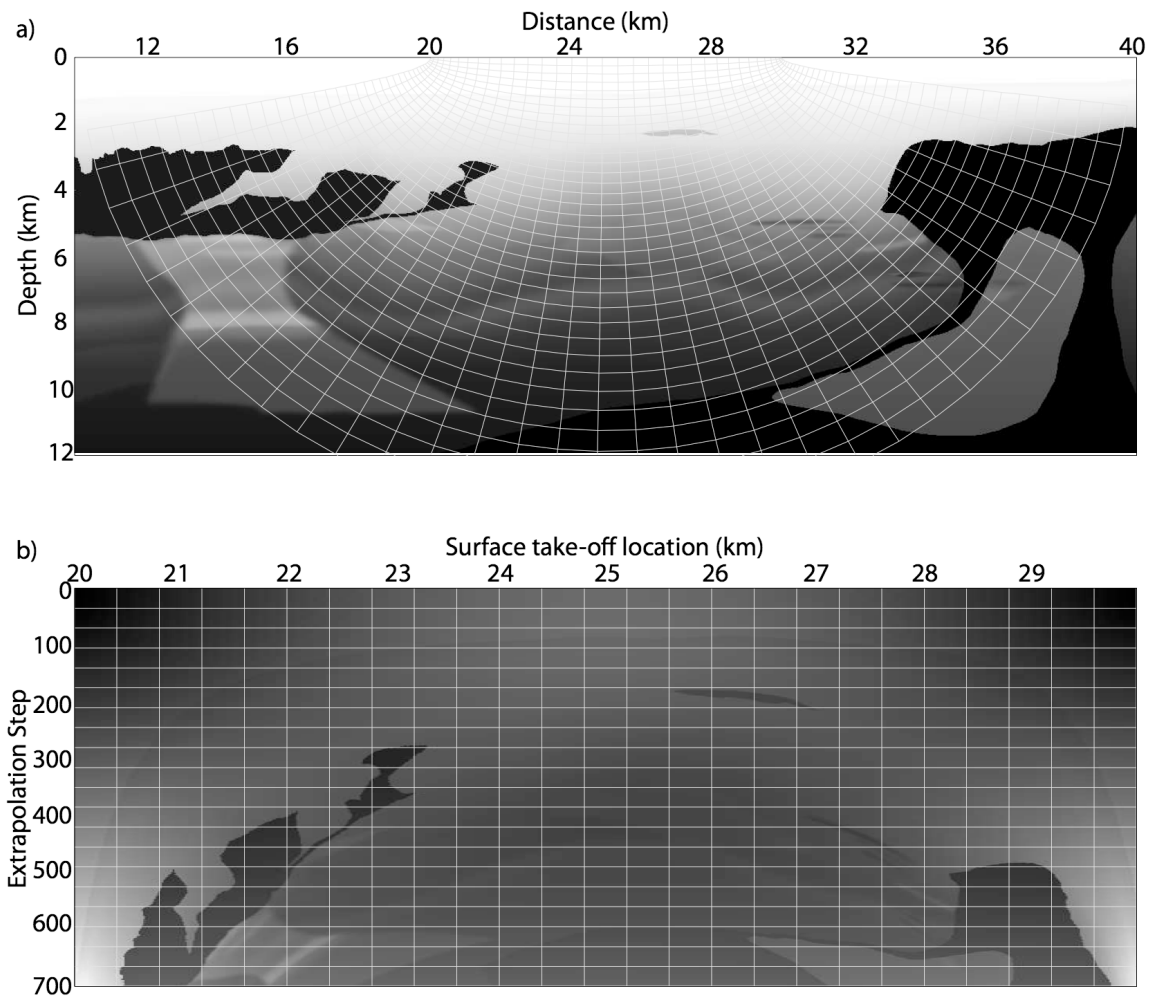


Figure 3.5: Prestack migration test in elliptical coordinates. a) Benchmark synthetic velocity model with the elliptical coordinate system overlain. b) Effective slowness model in the transformed elliptical coordinate system. **NR** georwe/. Figure5

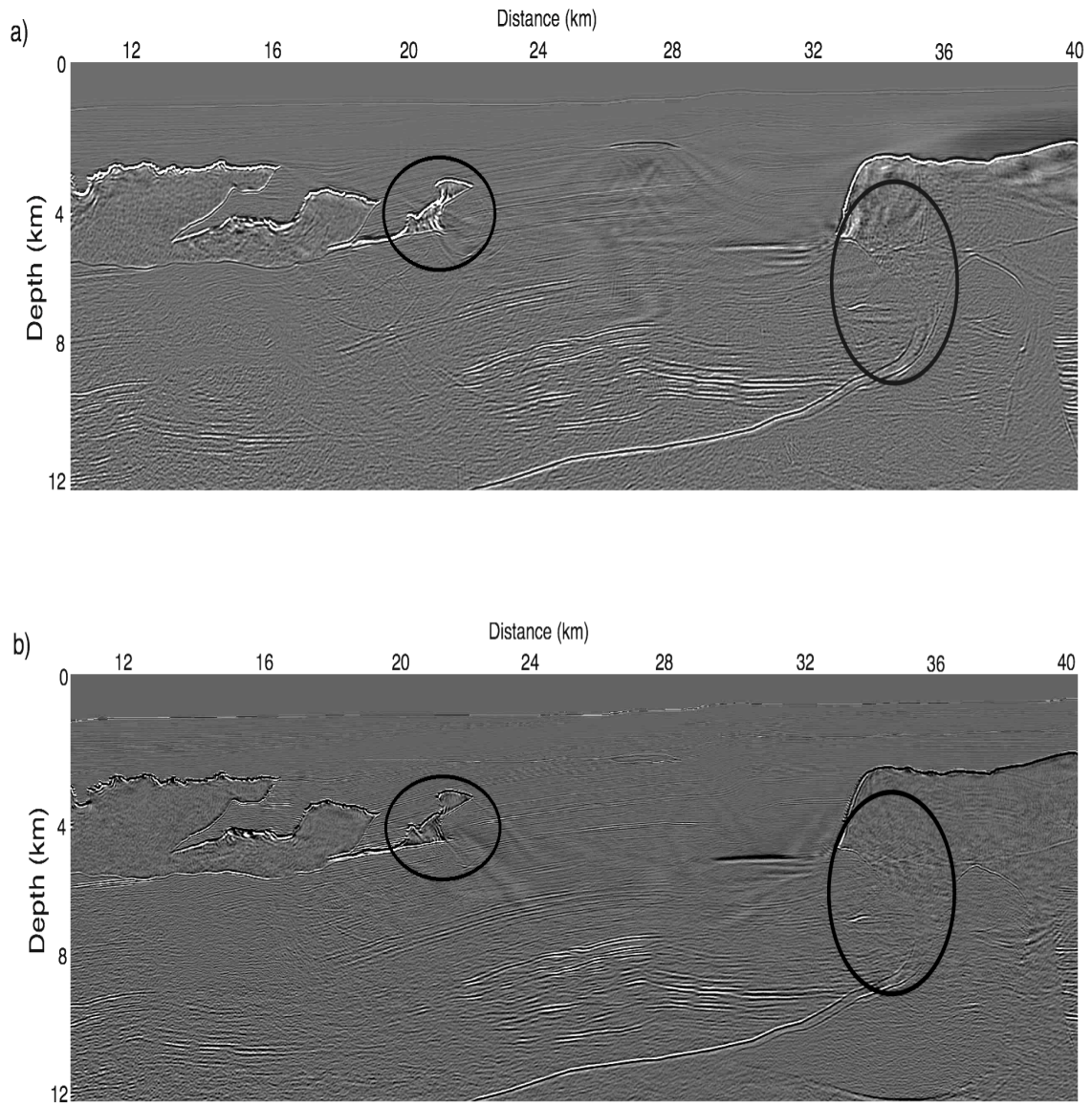


Figure 3.6: Synthetic migration results. a) Elliptical-coordinate migration result using finite-difference propagators. b) Cartesian migration result generated by finite-difference extrapolators of equivalent accuracy. **CR** georwe/. Figure6

## Discussion

One question naturally arising when using RWE propagation in a prestack migration algorithm is how does one obtain the optimal trade-off between using i) low-order extrapolators on more dynamic coordinate systems (e.g. ray coordinates); and ii) high-order extrapolators on analytic meshes less conformal to the wavefield propagation direction. Based on experience, I argue that a parametric coordinate system (such as a tilted Cartesian or an elliptical mesh) offers the advantage of developing analytic extrapolation operators that readily lend themselves to high-order finite-difference schemes. While coordinate systems based on ray tracing better conform to the wavefield propagation direction, numerically generated meshes do not lend themselves as easily to high-order extrapolators because of the greater number, and spatially variability, of corresponding mixed-domain coefficients. In addition, analytic coordinates allow the user to specify a coordinate system adequate for propagating both the source and receiver wavefields, rather than optimizing for one or the other. One caveat, however, is that higher-order extrapolators are usually required for analytic coordinate systems because, though they are more optimal for global propagation, they are less conformal to the local extrapolation direction.

## CONCLUSIONS

This chapter applies the Riemannian wavefield extrapolation on approach of Chapter 2 to 2D prestack shot-profile migration. I choose an elliptical coordinate system that generally conforms to the wave-propagation direction and enables large-angle extrapolation of both source and receiver wavefields. Post-stack migration results of a turning-wave data set validate the approach, while the 2D prestack imaging results show that the RWE migration algorithm generates images more accurate than the corresponding Cartesian algorithms. The cost difference between the elliptical and Cartesian imaging algorithms is only two additional interpolations per migrated shot profile. I argue that parametric coordinate systems are a good trade-off between the competing constraints of meshes conformal to the wavefield propagation direction and

coordinate system simplicity because one can readily develop analytic wavenumbers and more accurate high-order extrapolation implementations. Finally, I examine 2D elliptical-coordinate angle-domain common-image gathers in Chapter 4, and provide a 3D prestack migration extension of the analytic coordinate approach in Chapter 5.

## ACKNOWLEDGMENTS

I thank Guojian Shan, Biondo Biondi, Ben Witten, Brad Artman, and Ken Larner for enlightening discussions. I acknowledge BP for the synthetic velocity data set. I also acknowledge the reviewers of the Geophysics manuscript and thank them for their helpful comments. Guojian Shan is a second author on the Geophysics paper.

# Chapter 4

## Generalized-coordinate ADCIGs

The theory of angle-domain common-image gathers (ADCIGs) is extended to migrations performed in generalized 2D coordinate systems. I develop an expression linking the definition of reflection opening angle to differential traveltime operators and spatially varying weights derived from the non-Cartesian geometry. I demonstrate that generalized coordinate ADCIGs can be calculated directly using Radon-based offset-to-angle approaches for coordinate systems behaving locally isotropic. The canonical examples of tilted Cartesian, polar, and elliptic coordinates are used to illustrate the ADCIG theory. I compare analytically and numerically generated image volumes for a set of elliptically shaped reflectors. Experiments with a synthetic data set illustrate that relative to conventional Cartesian image volumes elliptic-coordinate ADCIGs better resolve the reflection opening angles of steeply dipping structure, due to improved large-angle propagation and enhanced sensitivity to steep structural dips afforded by coordinate system transformations. Results from this chapter have been accepted for publication as ?.

### INTRODUCTION

Angle-domain common-image gathers (ADCIGs) are used increasingly in seismic imaging to examine migration velocity model accuracy (?). The key idea is that

migrating with the correct velocity model leads to flat angle gathers that shift neither vertically nor horizontally as a function of reflection opening angle. Migrating with an incorrect velocity, though, leads to inconsistent angle-domain reflectivity and generates residual curvature in the ADCIG volume. ADCIGs are thus an effective velocity analysis tool and have been incorporated in wave-equation-based inversion schemes to update velocity profiles (??).

Wave-equation imaging techniques generate ADCIGs in straightforward manners for both shot-profile (???) and shot-geophone (??) migration approaches. In shot-profile migration, one first generates a subsurface-offset axis at each depth step by correlating the source and receiver wavefields at a number of subsurface shifts. The second step involves computing an offset-to-angle domain transformation using, for example, post-imaging Radon-based operators (?).

Conventional ADCIG theory usually assumes horizontal wavefield shifts, largely because wavefield extrapolation and imaging are most commonly performed in Cartesian coordinates. However, a number of studies have noted that these ADCIG results degrade for steeply dipping structures, such as salt flanks (??). Although this is partially due to problems associated with inaccurate large-angle extrapolation, ADCIGs calculated using horizontal wavefield shifts become decreasingly sensitive for increasingly steep structural dips. ? demonstrate that this problem can be addressed by generating ADCIGs with vertical offset-domain common-image gathers (VODCIGs); however, this approach is less desirable computationally because it requires storing the larger wavefield volumes required to calculate the VODCIGs in memory.

The introduction of shot-profile migration in more general coordinate systems [e.g. tilted Cartesian (?) and elliptical meshes (?)] presents an opportunity to circumvent problems associated with generating ADCIGs for steeply dipping structure. In particular, migration domains can be oriented such that geologic structures with steep dips in Cartesian meshes have relatively gentle dips in generalized coordinate systems, thus improving the robustness of the ADCIG calculation. Developing an ADCIG theory capable of handling more arbitrary coordinate meshes, though, requires proper treatment of the effects of non-Cartesian geometries. For example, wavefield extrapolation

in non-Cartesian coordinate systems induces local wavenumber stretches, rotations and/or shearing (see Chapter 2). Similarly, non-uniform wavefield sampling can lead to anisotropic angle-domain stretching. These effects can be corrected using Jacobian change-of-variable transformations.

The goal of this chapter is to extend ADCIG theory to non-Cartesian geometries. I demonstrate that ADCIG theory, as developed in a differential sense (?), remains valid for arbitrary geometries provided that the corresponding derivative operators are properly specified. Non-Cartesian coordinates do, however, introduce space-domain geometric factors that can render Fourier-based offset-to-angle methods unsuitable. However, I show that ADCIGs can be calculated directly in the Fourier domain for all coordinate systems satisfying the Cauchy-Riemann differentiability criteria (?). Moreover, ADCIGs can be calculated in all situations using the slant-stack approaches discussed in ?.

I begin by reviewing how to generate subsurface offsets and ADCIGs in Cartesian coordinates. I then provide an extension to generalized coordinate systems based on Jacobian change-of-variable arguments. I examine two canonical coordinate systems, tilted Cartesian and elliptical meshes, where the reflection angle can be explicitly calculated using Fourier-based methods, and a third, polar coordinates, where it cannot. I test the generalized ADCIG theory analytically and numerically using a set of elliptical reflectors, and demonstrate how computing angle gathers in elliptical coordinates can lead to improvements relative to Cartesian coordinates, especially for steeply dipping structure.

## ADCIG THEORY

The ADCIG theory presented in this section draws from that presented in ?. In the ensuing development,  $\mathbf{x} = [x_1, x_3]$  denotes the Cartesian variables and  $\boldsymbol{\xi} = [\xi_1, \xi_3]$  represents a generalized Riemannian coordinate system. I also use a convention where the extrapolation axis is oriented in the  $x_3$  ( $\xi_3$ ) direction for Cartesian (Riemannian) coordinates. Coordinates  $x_2 = \xi_2 = 0$  are assumed throughout.

## Generating subsurface offsets axes

Shot-profile migration in Cartesian coordinates consists of completing a recursive two-step procedure. The first step involves propagating the source and receiver wavefields,  $S$  and  $R$ , from depth level  $x_3 - \Delta x_3$  to  $x_3$  using an extrapolation operator  $E_{x_3}[\cdot]$

$$\begin{aligned} E_{x_3}[S(x_3 - \Delta x_3, x_1 | \omega)] &= S(x_3, x_1 | \omega), \\ E_{x_3}^*[R(x_3 - \Delta x_3, x_1 | \omega)] &= R(x_3, x_1 | \omega), \end{aligned} \quad (4.1)$$

where  $*$  denotes the conjugate operator,  $\omega$  is angular frequency, and  $\Delta x_3$  is the depth step. A subsurface image,  $I$ , is subsequently computed at each extrapolation step by evaluating an imaging condition

$$I(x_3, x_1, h_{x_1}) = \sum_{\omega} S^*(x_3, x_1 + h_{x_1} | \omega) R(x_3, x_1 - h_{x_1} | \omega), \quad (4.2)$$

where the subsurface-offset axis,  $h_{x_1}$ , is generated by correlating the source and receiver wavefields at various relative shifts in the  $x_1$  direction. Finally, the ADCIG volume is computed using an offset-to-angle transformation operator,  $\mathbf{T}_x$

$$I(x_3, x_1, \gamma) = \mathbf{T}_x I(x_3, x_1, h_{x_1}), \quad (4.3)$$

where  $\gamma$  is the reflection opening angle shown in Figure 4.1.

Imaging in generalized coordinate systems follows the same two-step procedure. However, because of the different migration geometry in the  $\boldsymbol{\xi}$ -coordinate system, new extrapolation operators,  $E_{\xi_3}[\cdot]$ , must be used to propagate wavefields. I specify these operators using Riemannian wavefield extrapolation (RWE). I do not discuss RWE herein, and refer readers interested in additional information to Chapter 2.

The first generalized coordinate imaging step is performing wavefield extrapolation

$$\begin{aligned} E_{\xi_3}[S(\xi_3 - \Delta \xi_3, \xi_1 | \omega)] &= S(\xi_3, \xi_1 | \omega), \\ E_{\xi_3}^*[R(\xi_3 - \Delta \xi_3, \xi_1 | \omega)] &= R(\xi_3, \xi_1 | \omega), \end{aligned} \quad (4.4)$$

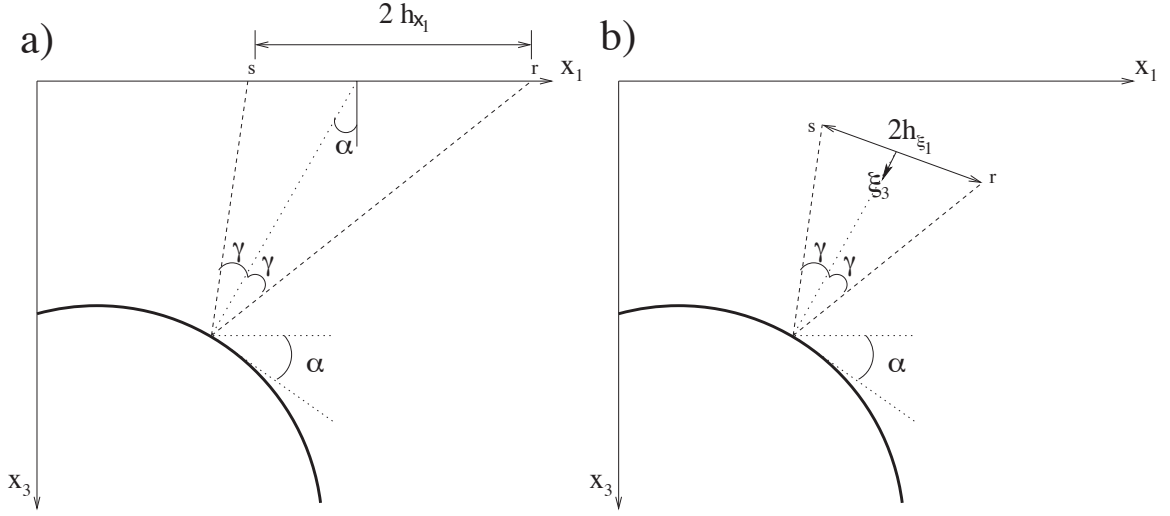


Figure 4.1: Cartoon illustrating the geometry of the ADCIG calculation. Parameter  $\gamma$  is the reflection opening angle,  $\alpha$  is geologic dip. a) Cartesian geometry using coordinates  $x_1, x_3$  and  $h_{x_1}$ . b) Generalized geometry using coordinates  $\xi_1, \xi_3$  and  $h_{\xi_1}$ . Adapted from ?. NR radcig/. Figure1

where  $\Delta\xi_3$  is the extrapolation step increment. Generalized coordinate images are then constructed by evaluating an imaging condition

$$I(\xi_3, \xi_1, h_{\xi_1}) = \sum_{\omega} S^*(\xi_3, \xi_1 + h_{\xi_1}|\omega)R(\xi_3, \xi_1 - h_{\xi_1}|\omega), \quad (4.5)$$

where  $h_{\xi_1}$  is the  $\xi$ -coordinate equivalent of Cartesian subsurface offset axis  $h_{x_1}$ . The generalized coordinate ADCIG volume is generated by applying an offset-to-angle transformation  $\mathbf{T}_{\xi}$

$$I(\xi_3, \xi_1, \gamma) = \mathbf{T}_{\xi}I(\xi_3, \xi_1, h_{\xi_1}). \quad (4.6)$$

Conventional ADCIG volumes can be recovered by sinc interpolating each  $I(\xi_3, \xi_1, \gamma)$  image computed via equation 4.6 to the final Cartesian coordinate volume.

Figure 4.2 illustrates this process using the elliptical coordinate system. Panel 4.2a shows the BP synthetic velocity model (?) with an elliptical mesh overlain. Note that

the salt flanks to the right-side of the model are nearly vertical in Cartesian coordinates. Panel 4.2b shows the velocity model in panel 4.2a interpolated to the elliptical coordinate system. Importantly, the aforementioned salt flanks in the elliptical coordinate system are nearly horizontal, which should lead to ADCIG calculations more robust than in Cartesian coordinates. However, proving this assertion requires understanding the differences, if any, between the Cartesian and generalized coordinate offset-to-angle operators,  $\mathbf{T}_x$  and  $\mathbf{T}_\xi$ , in equations 4.3 and 4.6, respectively.

## Cartesian coordinate ADCIGs

For constant velocity media in conventional Cartesian geometry, a straightforward link exists between differential changes in the travel time,  $t$ , of rays connecting the source-reflector and reflector-receiver paths to changes in the subsurface offset,  $h_{x_1}$ , and depth,  $x_3$ , coordinates. Figure 4.1a shows the geometry of these variables.

Mathematically, these relationships are

$$\begin{bmatrix} \frac{\partial t}{\partial h_{x_1}} \\ \frac{\partial t}{\partial x_3} \end{bmatrix} = 2s \cos \alpha \begin{bmatrix} \sin \gamma \\ \cos \gamma \end{bmatrix}, \quad (4.7)$$

where  $s$  is slowness,  $\alpha$  is reflector dip, and  $\gamma$  is the reflection opening angle. The right-hand-side of equations 4.7 are derived by ?. Equations 4.7 can be rewritten as

$$-\left. \frac{\partial x_3}{\partial h_{x_1}} \right|_{x_1, t} = \frac{\partial t}{\partial h_{x_1}} \bigg/ \frac{\partial t}{\partial x_3} = \tan \gamma, \quad (4.8)$$

where the negative sign derives from use of the implicit functions theory (?). ? note that Cartesian ADCIGs become pathogenically degenerate in situations where  $\frac{\partial t}{\partial x_3} \rightarrow 0$  (i.e. for steeply dipping structures where  $\alpha \rightarrow 90^\circ$  in Figure 4.1). Vertically oriented structures are, generally, not well imaged in Cartesian coordinates because of limited large-angle propagation in downward extrapolation.

Finally, because equation 4.7 has no explicit geometric-dependence, Fourier-based

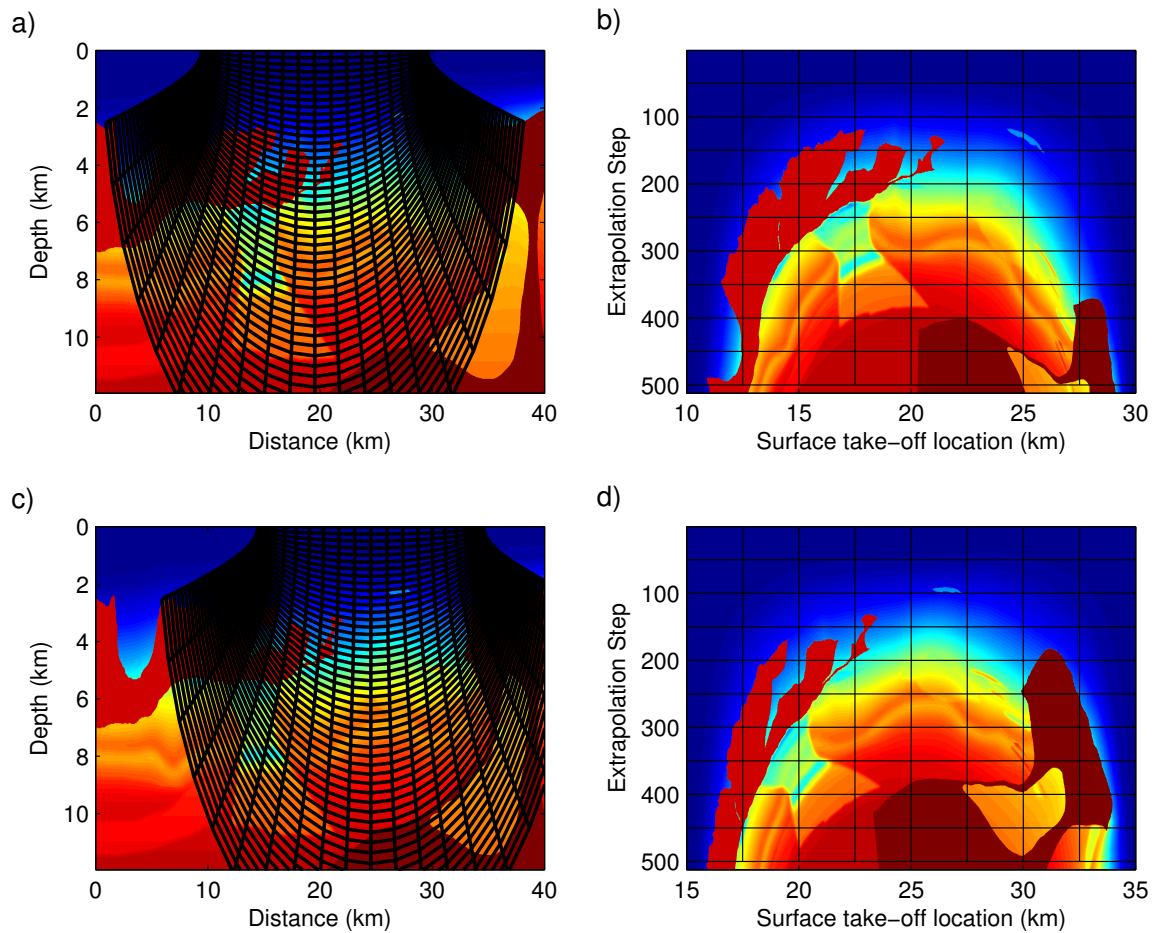


Figure 4.2: Prestack migration test in elliptical coordinates. a) Benchmark synthetic velocity model with an overlying elliptical coordinate system. b) Effective slowness model in the transformed elliptical coordinate system in a). c) Benchmark synthetic velocity model with a different overlying elliptical coordinate system. d) Effective elliptical coordinate slowness model for the coordinate system in c). **NR**

radcig/. Figure2

methods can calculate the reflection opening angle directly in the wavenumber domain

$$\tan \gamma = -\frac{k_{h_{x_1}}}{k_{x_3}}, \quad (4.9)$$

where  $k_{h_{x_1}}$  and  $k_{x_3}$  are the wavenumbers in the  $h_{x_1}$  and  $x_3$  directions, respectively.

## Generalized coordinate ADCIGs

Figure 4.1b illustrates a scenario similar to that in Figure 4.1a, but for a more general coordinate system. The reflection opening angle,  $\gamma$ , and the reflector dip,  $\alpha$ , obviously remain unchanged in the subsurface; however, the orientations of the  $h_{\xi_1}$  and  $\xi_3$  axes used to estimate  $\gamma$  now differ. The key question is, which quantities in the ADCIG calculation are affected by this change of variables?

Answering this question requires properly formulating the derivative operators,  $\frac{\partial}{\partial x_3}$  and  $\frac{\partial}{\partial h_{x_1}}$ , in equations 4.7 in the generalized coordinate system variables  $\boldsymbol{\xi} = [\xi_1, \xi_3]$  and  $\mathbf{h}_{\boldsymbol{\xi}} = [h_{\xi_1}, h_{\xi_3}]$ . Appendix E shows how these derivatives can be specified using Jacobian change-of-variable arguments. Assuming that the subsurface-offset axes are formed by uniform wavefield shifts, Appendix E derives the following expression for generalized coordinate ADCIGs:

$$-\left. \frac{\partial \xi_3}{\partial h_{\xi_1}} \right|_{\xi_1, t} = \frac{\partial t}{\partial h_{\xi_1}} \bigg/ \frac{\partial t}{\partial \xi_3} = \tan \gamma \frac{\left( \frac{\partial x_1}{\partial \xi_1} \cos \alpha - \frac{\partial x_3}{\partial \xi_1} \sin \alpha \right)}{\left( \frac{\partial x_3}{\partial \xi_3} \cos \alpha + \frac{\partial x_1}{\partial \xi_3} \sin \alpha \right)}. \quad (4.10)$$

Note that if the  $\boldsymbol{\xi}$ -coordinate system satisfies the Cauchy-Riemann differentiability criteria (?)

$$\frac{\partial x_1}{\partial \xi_1} = \frac{\partial x_3}{\partial \xi_3} \quad \text{and} \quad \frac{\partial x_3}{\partial \xi_1} = -\frac{\partial x_1}{\partial \xi_3}, \quad (4.11)$$

equation 4.10 then reduces to

$$-\left. \frac{\partial \xi_3}{\partial h_{\xi_1}} \right|_{\xi_1, t} = \tan \gamma. \quad (4.12)$$

This is the generalized coordinate equivalent of the Cartesian expression in equation 4.7. A physical meaning of the criteria in equations 4.11 is that the coordinate system must behave isotropically (i.e. dilatationally and rotationally) in the neighborhood of every grid point. Three canonical examples, two of which satisfy equations 4.11, are discussed in the following section.

Similar to Cartesian coordinates, elliptical coordinate ADCIGs become insensitive where structural dips cause  $\frac{\partial t}{\partial \xi_3} \rightarrow 0$ . However, this insensitivity can be minimized when using generalized coordinate systems, because structural dips appear at different angles in different translated meshes. Figures 4.2c-d illustrate this by showing an elliptical coordinate shifts for a shot-location different than that presented in panels 4.2a-b. Note the changes in structural dip in the right-hand-side of the elliptical coordinate panels. Thus, while ADCIGs calculated on one elliptical grid may be insensitive to certain structure locally, mesh translation ensures that ADCIGs are sensitive globally. Imaging steep dips in elliptical coordinates, though, is limited by the accuracy of wide-angle one-way wavefield extrapolation.

Finally, one may calculate reflection opening angles in the wavenumber domain for coordinate systems satisfying equations 4.11

$$\tan \gamma = -\frac{k_{h_{\xi_1}}}{k_{\xi_3}}, \quad (4.13)$$

where  $k_{h_{\xi_1}}$  and  $k_{\xi_3}$  are the wavenumbers in the  $h_{\xi_1}$  and  $\xi_3$  directions, respectively. While some non-orthogonal coordinate systems might satisfy equations 4.11, most practical applications will have orthogonal  $k_{h_{\xi_1}}$  and  $k_{\xi_3}$ .

## CANONICAL EXAMPLES

This section presents three canonical examples that illustrate the generalized ADCIG theory: tilted Cartesian, polar, and elliptical coordinate systems. Figure 4.3 presents schematic examples of these three coordinate systems.

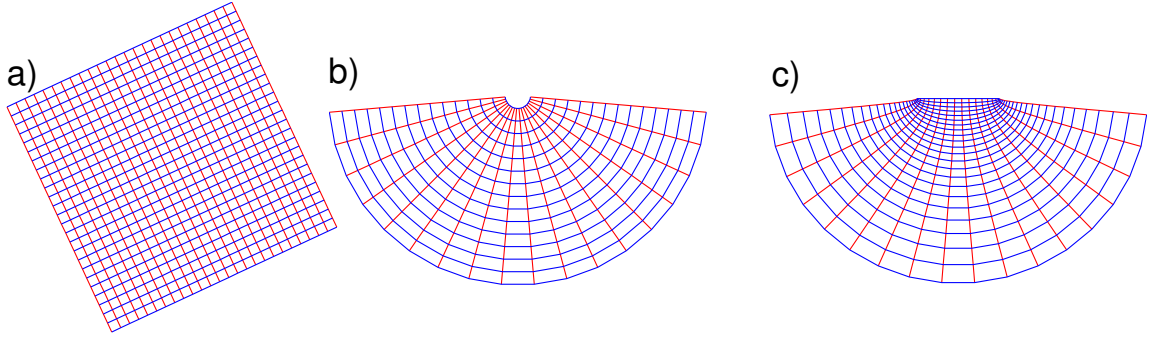


Figure 4.3: Canonical coordinate system examples. a) Tilted Cartesian coordinates. b) Polar coordinates. c) elliptical coordinates. **NR** radcig/. Figure3

## Tilted Cartesian coordinates

Tilted Cartesian coordinates are a useful generalized migration coordinate system (see Figure 4.3a). ? use this mesh in a plane-wave migration scheme where the coordinate system is oriented toward the plane-wave take-off angle to improve large-angle propagation accuracy. A tilted Cartesian mesh is defined by

$$\begin{bmatrix} x_1 \\ x_3 \end{bmatrix} = \begin{bmatrix} \cos \theta & -\sin \theta \\ \sin \theta & \cos \theta \end{bmatrix} \begin{bmatrix} \xi_1 \\ \xi_3 \end{bmatrix}, \quad (4.14)$$

where  $\theta$  is the tilt angle. The partial derivative transform matrix is

$$\begin{bmatrix} \frac{\partial x_1}{\partial \xi_1} & \frac{\partial x_1}{\partial \xi_3} \\ \frac{\partial x_3}{\partial \xi_1} & \frac{\partial x_3}{\partial \xi_3} \end{bmatrix} = \begin{bmatrix} \cos \theta & -\sin \theta \\ \sin \theta & \cos \theta \end{bmatrix}, \quad (4.15)$$

which leads to the following ADCIG equation:

$$-\left. \frac{\partial \xi_3}{\partial h_{\xi_1}} \right|_{\xi_1, t} = \tan \gamma \frac{(\cos \theta \cos \alpha + \sin \theta \sin \alpha)}{(\cos \theta \cos \alpha + \sin \theta \sin \alpha)} = \tan \gamma. \quad (4.16)$$

Thus, calculating ADCIGs in tilted Cartesian coordinates directly recovers the correct reflection opening angle. Note that setting  $\theta = 0^\circ$  recovers the Cartesian expression in equation 4.8.

## Polar coordinates

The polar coordinate system (see Figure 4.3b), where the extrapolation direction is oriented along the radial direction, is appropriate for generating 2D Green's function estimates. The polar coordinate system is defined by

$$\begin{bmatrix} x_1 \\ x_3 \end{bmatrix} = \begin{bmatrix} a \xi_3 \cos \xi_1 \\ a \xi_3 \sin \xi_1 \end{bmatrix}. \quad (4.17)$$

The partial derivative transformation matrix is

$$\begin{bmatrix} \frac{\partial x_1}{\partial \xi_1} & \frac{\partial x_1}{\partial \xi_3} \\ \frac{\partial x_3}{\partial \xi_1} & \frac{\partial x_3}{\partial \xi_3} \end{bmatrix} = \begin{bmatrix} -a \xi_3 \sin \xi_1 & a \cos \xi_1 \\ a \xi_3 \cos \xi_1 & a \sin \xi_1 \end{bmatrix}, \quad (4.18)$$

which leads to the following ADCIG equation:

$$-\left. \frac{\partial \xi_3}{\partial h_{\xi_1}} \right|_{\xi_1, t} = \xi_3 \tan \gamma \frac{(-\sin \xi_1 \cos \alpha - \cos \xi_1 \sin \alpha)}{(\sin \xi_1 \cos \alpha + \cos \xi_1 \sin \alpha)} = -\xi_3 \tan \gamma. \quad (4.19)$$

Thus, one cannot calculate ADCIGs directly with Fourier-based methods in polar coordinates because of the spatial geometric dependence on  $\xi_3$ . However, polar-coordinate ADCIGs can be calculated using slant-stack processing in the trace domain (?), because the geometric factor  $\xi_3$  is no more than a local weight applied to the velocity model used to calculate the angle gathers.

## Elliptical coordinates

Elliptical coordinates (see Figure 4.3c) are a useful coordinate system for performing 2D shot-profile migration (see Chapter 2). An elliptical mesh is defined by

$$\begin{bmatrix} x_1 \\ x_3 \end{bmatrix} = \begin{bmatrix} a \cosh \xi_3 \cos \xi_1 \\ a \sinh \xi_3 \sin \xi_1 \end{bmatrix}. \quad (4.20)$$

The partial derivative transformation matrix is

$$\begin{bmatrix} \frac{\partial x_1}{\partial \xi_1} & \frac{\partial x_1}{\partial \xi_3} \\ \frac{\partial x_3}{\partial \xi_1} & \frac{\partial x_3}{\partial \xi_3} \end{bmatrix} = a \begin{bmatrix} \cosh \xi_3 \sin \xi_1 & \sinh \xi_3 \cos \xi_1 \\ -\sinh \xi_3 \cos \xi_1 & \cosh \xi_3 \sin \xi_1 \end{bmatrix}, \quad (4.21)$$

which leads to the following ADCIG equation:

$$-\left. \frac{\partial \xi_3}{\partial h_{\xi_1}} \right|_{\xi_1, t} = \tan \gamma \frac{(\cosh \xi_3 \sin \xi_1 \cos \alpha - \sinh \xi_3 \cos \xi_1 \sin \alpha)}{(\cosh \xi_3 \sin \xi_1 \cos \alpha - \sinh \xi_3 \cos \xi_1 \sin \alpha)} = \tan \gamma. \quad (4.22)$$

Thus, calculating ADCIGs in elliptical coordinates with Fourier-based methods will directly recover the true reflection opening angle.

## NUMERICAL EXAMPLES

This section presents numerical tests of the generalized theory by comparing the ADCIG volumes for elliptical and Cartesian coordinate systems. I generated the results using a shot-profile migration algorithm altered to account for elliptical geometry by replacing the Cartesian extrapolator,  $E_{x_3}[\cdot]$ , with an elliptical coordinate operator,  $E_{\xi_3}[\cdot]$ . In both coordinate systems, the implemented extrapolation operators were accurate to roughly  $\pm 80^\circ$  (?) with respect to the extrapolation axis. The reader is referred to Chapter 3 for further implementation details on shot-profile migration in elliptical coordinates.

I calculated ADCIG image volumes for each shot-profile by following a three-step procedure: 1) generate image volume  $I(\xi_1, \xi_3, h_{\xi_1})$  by computing the image for 64 subsurface shifts in  $h_{\xi_1}$  at each point in every extrapolation step; 2) calculate ADCIG volume  $I(\xi_1, \xi_3, \gamma)$  using the procedure described in ?; and 3) output the image  $I(x_1, x_3, \gamma)$  by sinc-based interpolation of single-shot ADCIGs to the global volume. Steps 1-3 were repeated for all shot-profile sections contributing to the final image.

## Test 1: Elliptical Isochrons

The first test demonstrates the impulse response of the ADCIG imaging operator. I do this by imaging the elliptical isochron responses of two offset point sources in a constant velocity medium (see Figure 4.4). The source wavefield impulse is at time  $t = 0$  s and at  $x = -1.12$  km, while the receiver wavefield impulses are at  $t = 2.0, 2.5, 3.0,$  and  $3.5$  s and  $x = 1.12$  km for a total source-receiver offset of  $2h = 2.24$  km. Correlating these two wavefield volumes leads to four elliptical isochrons specified by

$$x_1(t, h) = \frac{vt}{4} (\cos \theta_1 + \cos \theta_2) \quad (4.23)$$

$$x_3(t, h) = \frac{vt}{4} \left( 1 - \frac{h^2}{v^2 t^2} \right) (\sin \theta_1 + \sin \theta_2), \quad (4.24)$$

where, given the source take-off angle  $\theta_1$ , the receiver take-off angle  $\theta_2$  is obtained by

$$\theta_2 = \cos^{-1} \left[ \frac{\cos \theta_1 (\phi^2 + 1) - 2\phi}{\phi^2 - 2\phi \cos \theta_1 + 1} \right]. \quad (4.25)$$

where  $\phi = 2h/vt$ . The reflection opening angle, given by  $\gamma = 90 - \frac{(\theta_1 + \theta_2)}{2}$ , is shown color-coded on the scatterplot in Figure 4.4.

Figure 4.5 shows the ADCIG volumes calculated in both (a single) elliptical and Cartesian coordinate system. To generate this image, I first calculated an elliptical coordinate (EC)  $I(\xi_1, \xi_3, h_{\xi_1})$  volume by correlating the source and receiver wavefields at 64 subsurface shifts in  $h_{\xi_1}$  at each point in every extrapolation step. I then input this volume to a Fourier-based offset-to-angle transformation operator to generate the EC ADCIG volume,  $I(\xi_1, \xi_3, \gamma)$ , which I interpolated to Cartesian coordinates to generate the desired image volume,  $I(x_1, x_3, \gamma)$ . For the ADCIG transformation, I choose to limit the maximum opening angle to  $\gamma = \pm 45^\circ$ .

Panel 4.5a presents the elliptical coordinate image extracted at  $\gamma = -24^\circ$  from the ADCIG volume  $I(x_1, x_3, \gamma)$ . The ADCIG volumes consist of elliptically shaped reflectors (panels 4.5a) that, ideally, are localized in the angle domain (panels 4.5b-c and f-h). The analytical ADCIG locations are represented by black dots. The breadth of

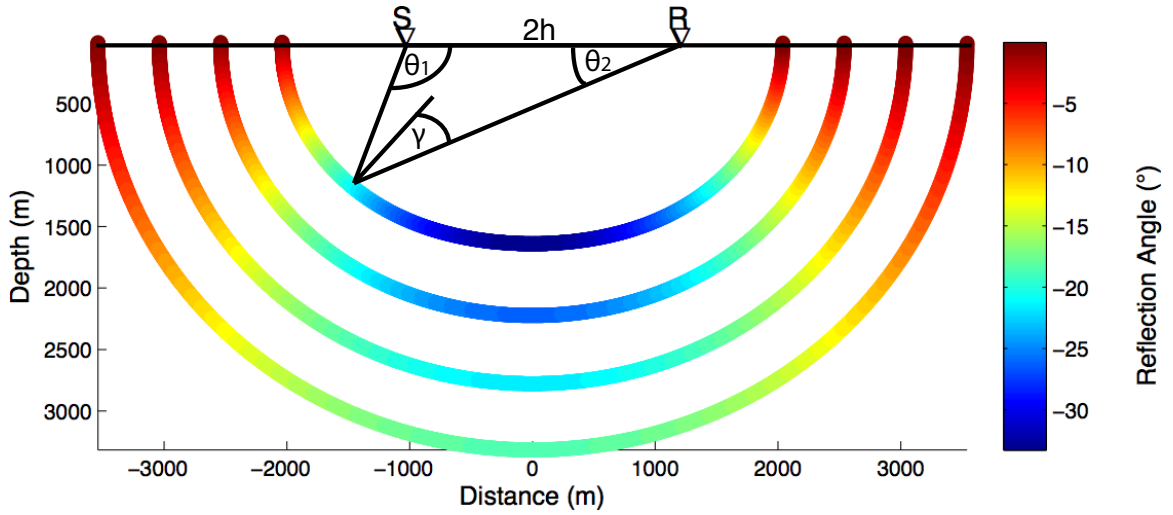


Figure 4.4: Theoretical results for an elliptical isochron for four travel times in a constant velocity medium. The elliptical surfaces are color-coded according to reflection opening angle. **NR** radcig/. Figure4

the analytic ADCIG response derives from the coarse binning in the angular domain. The analytically and numerically generated results are well matched. Figure 4.5a also shows three vertical lines indicating the locations from left to right of the three ADCIGs in panels 4.5b-d. Again, the analytic and numerical ADCIGs are well matched, though less so at shallower depths due to the increased spreading about the image focal point.

The Cartesian coordinate (CC) ADCIGs are presented in panels 4.5e-h. Panel 4.5e shows the Cartesian image again extracted at  $\gamma = -24^\circ$  in the angle domain. Panels 4.5f-h present three ADCIGs at the same locations as in panels 4.5b-d. The Cartesian image volumes are well-matched to the elliptical coordinate examples, and good agreement between the theoretical results and the wavefield volume is observed in both images. Energy is focused in the neighborhood of the correct locations. The angle gathers are not always centered relative to the true location, though, which is more noticeable at shallower depths where the Cartesian and elliptical ADCIG volumes both overestimate the reflection opening angle.

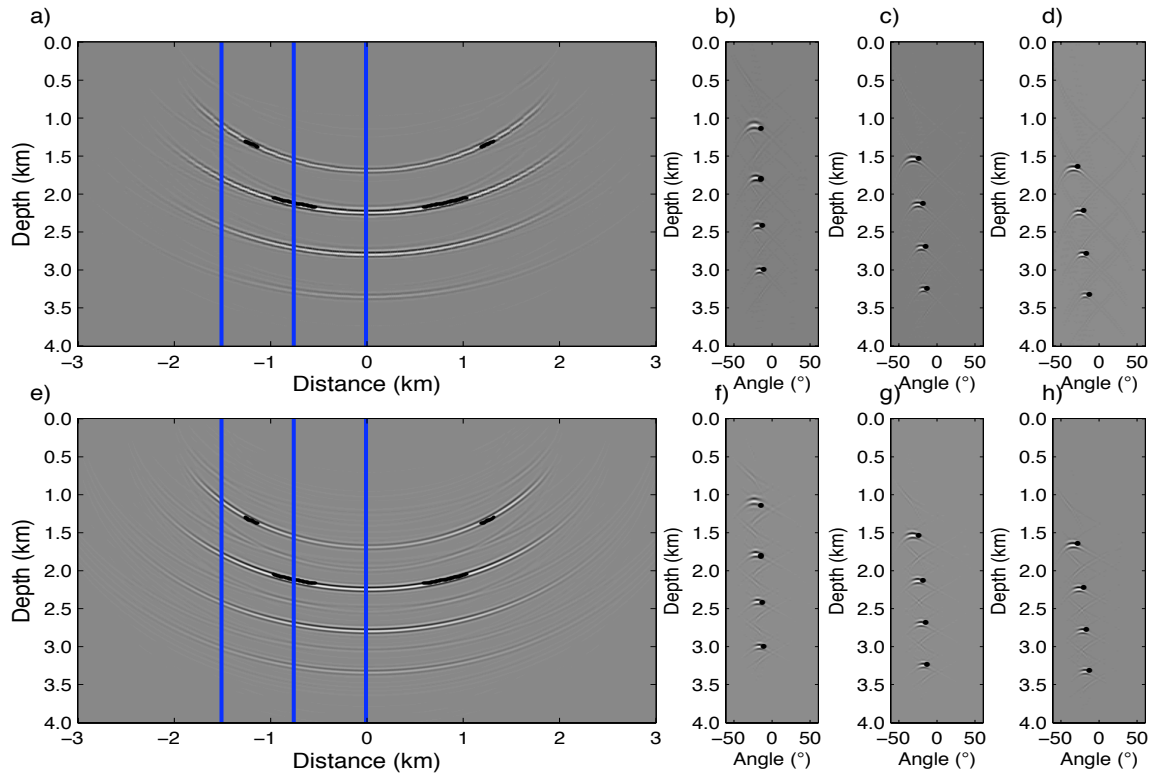


Figure 4.5: Elliptical reflector comparison tests between analytically (black bullets) and numerically generated ADCIG volumes. Panels a-d are computed in elliptical coordinates (EC), while panels e-h are in Cartesian coordinates (CC). a) EC image extracted at the  $-24^\circ$  reflection angle. b) EC angle gather at  $-1.5$  km. c) EC gather at  $0.75$  km. d) EC gather at  $0.0$  km. e) CC image extracted at the  $-24^\circ$  reflection angle. f) CC angle gather at  $-1.5$  km. g) CC gather at  $0.75$  km. h) CC gather at  $0.0$  km. **ER** radcig/. Figure5

Figure 4.6 presents the results of a test similar to that shown in Figure 4.5, but with the velocity model rescaled by 0.95. Again, the black dots show the location of the true image point (assuming a true velocity model). Note that the image points in each ADCIG remain well-focused, but shift nearer to the surface and to wider angles. Thus, imaging with an overly slow velocity model will generate, as expected, reflectors that exhibit upward curvature at wider angles.

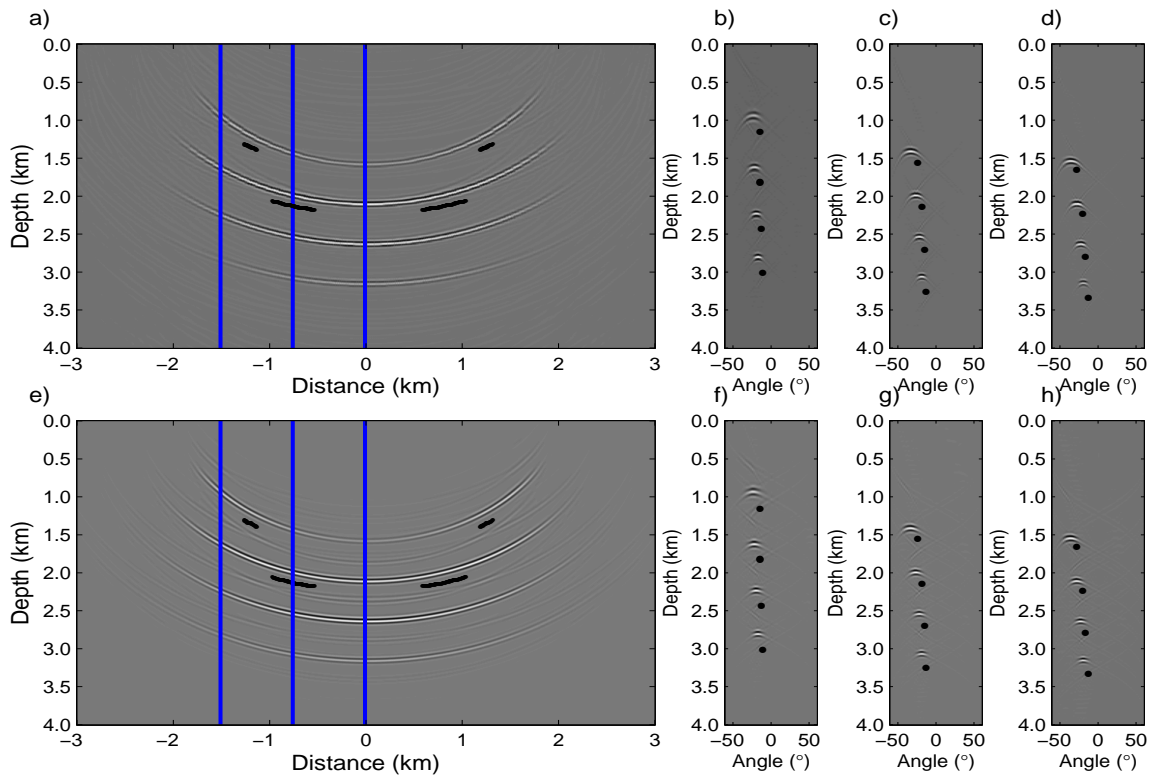


Figure 4.6: Elliptical reflector comparison tests between analytically (black bullets) and numerically generated ADCIG volumes using a velocity scaled by factor 0.95. Panels a-d are computed in elliptical coordinates (EC), while panels e-h are in Cartesian coordinates (CC). a) EC image extracted at the  $-24^\circ$  reflection angle. b) EC angle gather at  $-1.5$  km. c) EC gather at  $0.75$  km. d) EC gather at  $0.0$  km. e) CC image extracted at the  $-24^\circ$  reflection angle. f) CC angle gather at  $-1.5$  km. g) CC gather at  $0.75$  km. h) CC gather at  $0.0$  km. **ER** radcig/. Figure6

## Test 2: BP velocity model

The second test compares elliptical and Cartesian coordinate ADCIG volumes computed for the BP synthetic velocity model. Images computed in elliptical coordinates used only one coordinate system per shot. For the one-sided data set, I used a (surface) migration aperture of 12 km and located the source and farthest offset receiver (at 8 km) points 2 km in from the edges of the computational mesh. (Note that the migration aperture effectively expands during wavefield extrapolation because the coordinate mesh expands outward.) I found this initial migration geometry to produce the best results for the BP synthetic model through iterative testing. Generally, the optimal elliptical coordinate migration geometry is controlled by the velocity model.

Figure 4.7 shows slices all clipped at the 99<sup>th</sup> percentile from the corresponding elliptical and Cartesian ADCIG image volumes. Panel 4.7a shows an elliptical coordinate image with three vertical lines indicating the angle-gather locations from left to right in Figures 4.7b-d. The three panels show flat reflectors with predominantly one-sided reflectivity. This result is expected because the input migration data were not in a split-spread geometry. (This statement holds for all subsequent images calculated using this data set.) The only significant exceptions occur in panel 4.7b within salt where energy is exhibited for both positive and negative reflection angles. I attribute this to the reversal of source and receiver wavefield orientations within the salt. Note also that the curved events in the ADCIG volumes are the images of the multiple reflections off of the water bottom and top salt.

The image in panel 4.7d has a wide reflection zone between 3.75-4.25 km in depth, which occurs because the shown angle gather is a vertical slice through the nearly vertical salt flank. This creates the appearance of low-frequency noise, which is the appropriate response for a near-vertical reflector. Panel 4.7e shows the Cartesian image for the same location as panel 4.7a, while panels 4.7f-h are extracted from the same locations as panels 4.7b-d. The Cartesian angle gathers look similar to those in elliptical coordinates, except for the salt flanks to the right-hand-side of panel 4.7h.

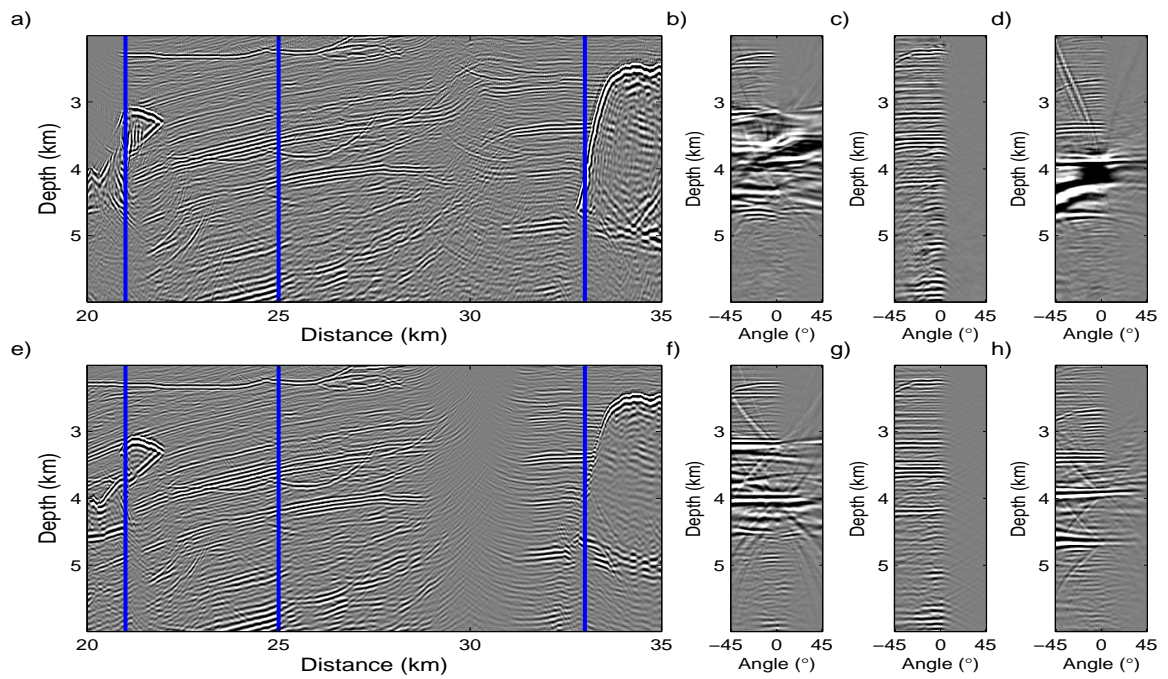


Figure 4.7: Vertical elliptical and Cartesian ADCIGs slices using the correct migration velocity model. a) elliptical coordinate image with three vertical lines showing the locations of ADCIG gathers from left to right in panels b-d. e) Cartesian coordinate image with three vertical lines showing the locations of ADCIG gathers from left to right in panels f-h. **CR** radcig/. Figure7

A final observation from Figure 4.7 is that ADCIGs calculated via subsurface correlations will generate artifacts at locations near salt-sediment interfaces - whether in an elliptical or a Cartesian coordinate system. This geologic setting leads to situations where a wavefield sample inside a salt body is correlated with another sample located in the sediment with a significantly different velocity. This significant velocity difference violates one of the theoretical ADCIG assumptions, namely that the velocity remains constant across the correlation window. Hence, one must be careful not to interpret ADCIG artifacts as signal useful for migration velocity analysis.

Figure 4.8 shows horizontal slices through the image volume that better resolve the vertical salt flank. Panel 4.8a presents the elliptical coordinate image, with three horizontal lines showing the ADCIG slice locations from top to bottom. The right-hand sides of panels 4.8b-d display the well-focused vertical salt-flank reflector. This demonstrates the robustness of the ADCIG calculation in elliptical coordinate systems. Panel 4.8e shows the Cartesian coordinate image with three horizontal lines showing the locations of the ADCIG slices. The right-hand salt-flank reflector in panel 4.8f is similarly well-resolved, largely because the structural dip is relatively low. However, the salt-flank images in panels 4.8g-h are somewhat blurred out. I attribute this to the combined effects of inaccurate large-angle extrapolation and insensitivity of the ADCIG calculation to steep structural dip.

An additional test examines how the ADCIG volumes change when introducing an incorrect migration velocity profile. Figure 4.9 presents ADCIG volumes similar to those shown in Figure 4.7 after using a migration velocity profile rescaled by 0.95. Both images are poorly focused and have residual curvature indicating an incorrect migration velocity. Because the reflectors are near vertical, though, the sensitivity of horizontal gathers is weak. This low sensitivity is greatly improved when examining the horizontal slices in Figure 4.10 taken at the same locations as in Figure 4.8. The elliptical angle gathers in panels 4.10b-d, and especially to the right-hand side in panel 4.10d, show much greater residual curvature. This indicates that the elliptical coordinate horizontal ADCIGs have greater sensitivity to velocity error for near-vertical structures than Cartesian coordinate horizontal ADCIGs. The imaging

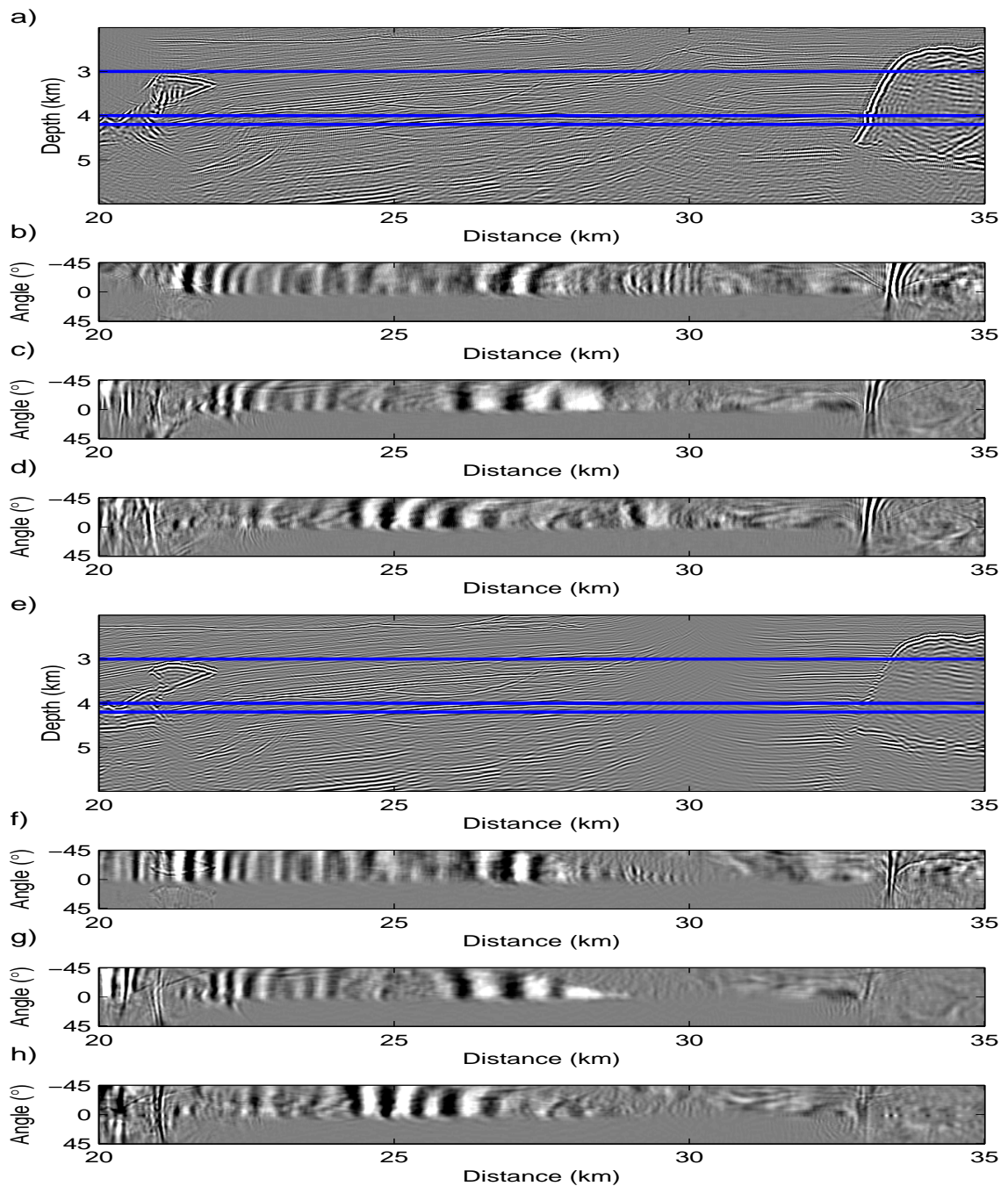


Figure 4.8: Horizontal elliptical and Cartesian ADCIGs slices using the correct migration velocity model. a) elliptical coordinate image with three horizontal lines showing the locations of horizontal ADCIG gathers from top to bottom in panels b-d. e) Cartesian coordinate image with three horizontal lines showing the locations of horizontal ADCIG gathers from top to bottom in panels f-h. **CR** radcig/. Figure8

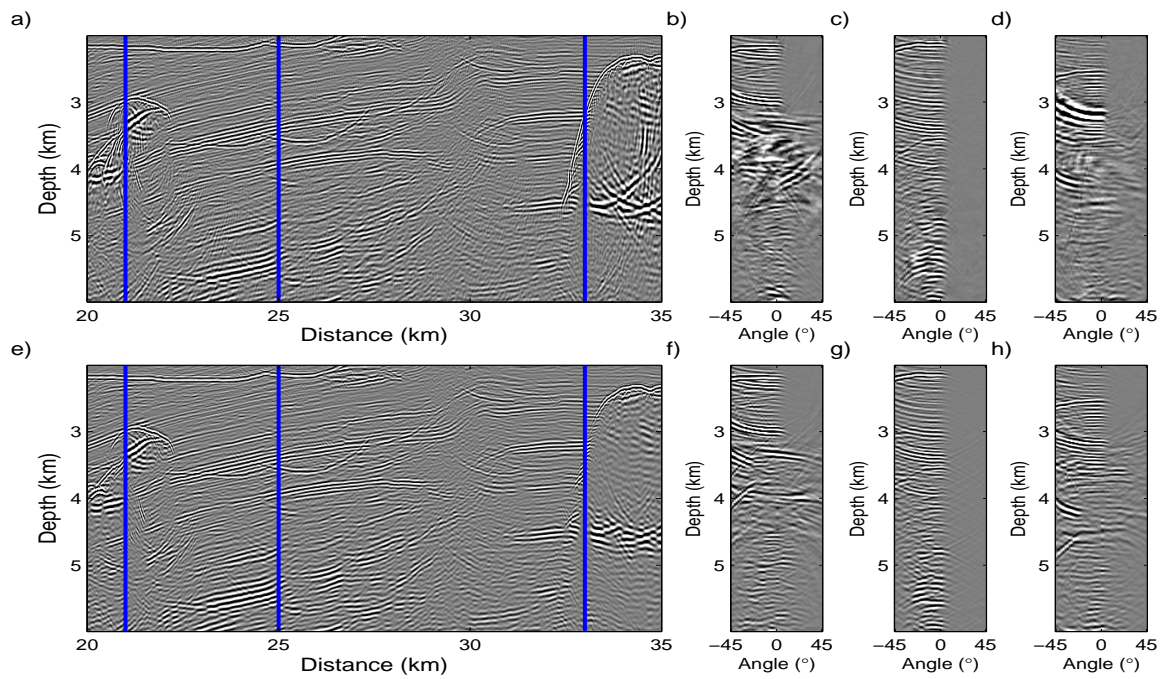


Figure 4.9: Vertical elliptical and Cartesian ADCIGs slices using an incorrect migration velocity model. a) elliptical coordinate image with three vertical lines showing the locations of vertical ADCIG gathers from left to right in panels b-d. e) Cartesian coordinate image with three vertical lines showing the locations of vertical ADCIG gathers from left to right in panels f-h. **CR** `radcig/`. Figure9

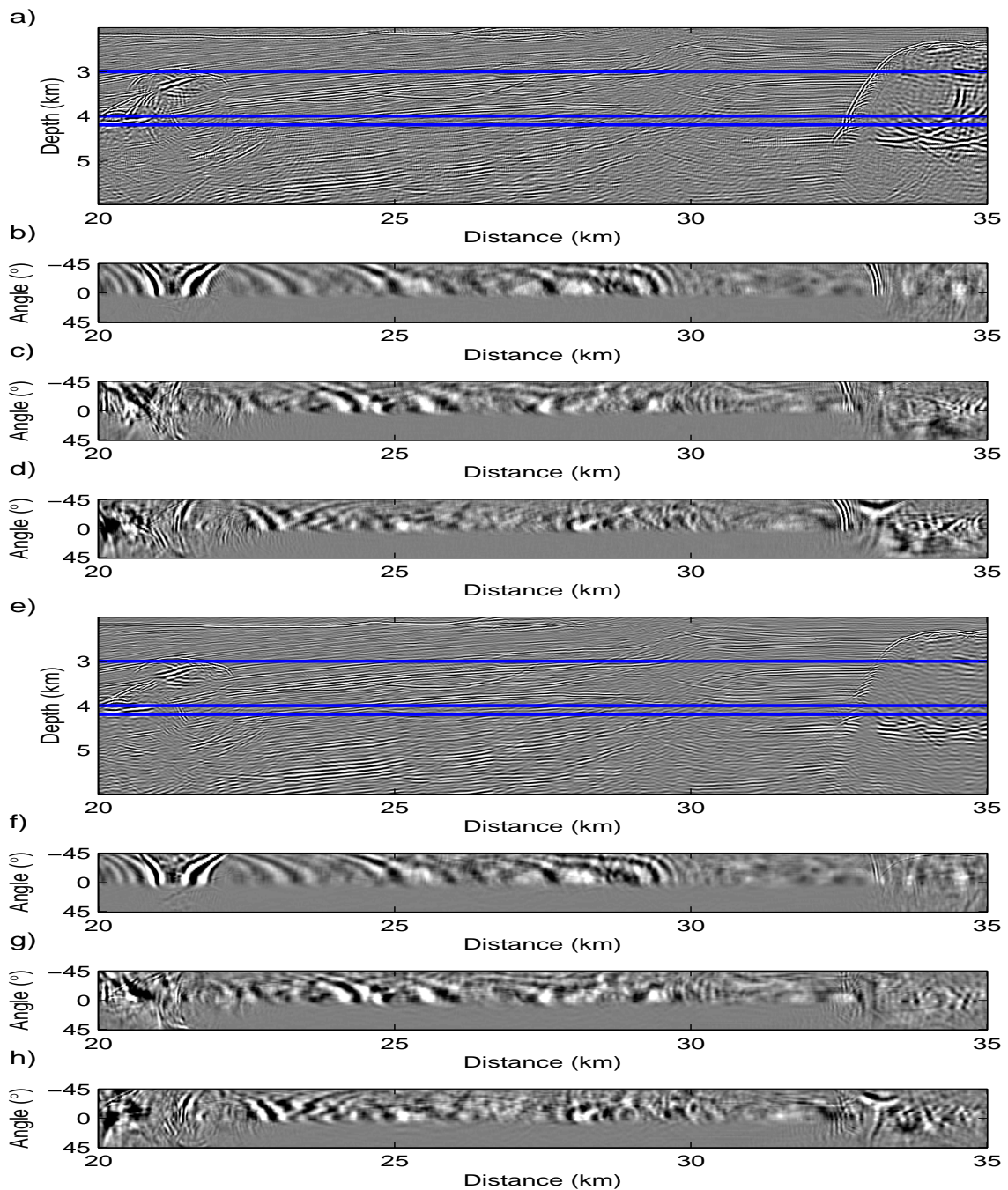


Figure 4.10: Horizontal elliptical and Cartesian ADCIGs slices using an incorrect migration velocity model. a) elliptical coordinate image with three horizontal lines showing the locations of horizontal ADCIG gathers from top to bottom in panels b-d. e) Cartesian coordinate image with three horizontal lines showing the locations of horizontal ADCIG gathers from top to bottom in panels f-h. **CR** radcig/. Figure10

enhancements afforded by elliptical coordinates should improve any migration velocity analysis approach that uses residual curvature in steeply dipping reflectors to compute velocity model updates.

## Discussion

Extending the above theory of generalized coordinate ADCIGs to 3D coordinate systems should be fairly straightforward, though more difficult to implement numerically. ? presents a theory for 3D Cartesian coordinates that specifies the differential travel-time expressions required to express the reflection opening angle,  $\gamma$ , in 3D Cartesian ADCIGs [see equation 16 in ?]. Applying Jacobian change-of-variable transformations to these equations should yield a 3D expression for reflection angle. Similar to 3D Cartesian coordinates, though, this quantity will depend on geologic dips and needs to be computed by one of the two algorithms suggested in ?.

Given that a 3D expression can be formulated, there are a number of coordinate systems well-suited to imaging steep geologic dips where 3D ADCIG volumes could be a good diagnostic tool for velocity analysis. ? discusses how a judicious choice of 3D coordinate system depends greatly on the acquisition geometry and the desired migration geometry. For example, the migration geometries employed in shot-profile migration of wide-azimuth data sets are well-matched with 3D ellipsoidal meshes that enable high-angle and turning-wave propagation in all directions. Evaluating ADCIG image focussing in such a 3D coordinate geometry would then provide information on velocity model accuracy for steeply dipping reflectors - such as salt flanks. These somewhat speculative extensions, though, are beyond the scope of this chapter and remain an active area of research.

## CONCLUSIONS

I extend the Cartesian ADCIG theory to 2D generalized coordinate systems. The generalized ADCIG expressions related the reflection opening angle to differential

travel-time operators and spatially varying weights derived from the non-Cartesian geometry. I show that these geometric expressions cancel out for coordinate systems satisfying the Cauchy-Riemann differentiability criteria, which include tilted Cartesian and elliptical meshes. The procedure for calculating ADCIGs in elliptical coordinates is very similar to that in Cartesian coordinates. I validate the approach by comparing analytically and numerically generated ADCIG volumes, and with tests on the BP synthetic data set. ADCIGs calculations are more robust when computed in elliptical coordinates than in Cartesian coordinate. I assert that this result is due to improved large-angle propagation and enhanced sensitivity to steep structural dips afforded by the coordinate transforms. Finally, the imaging advantages afforded by elliptical coordinates should improve the procedure of any migration velocity analysis approach that uses residual ADCIG curvature on steeply dipping reflectors to compute velocity model updates.

## ACKNOWLEDGMENTS

I would like to thank Biondo Biondi, Alejandro Valenciano, Antoine Guitton and Brad Artman for helpful discussions, and BP for releasing the synthetic data used in the examples. I thank Tamas Nemeth, Samuel Gray, and an anonymous reviewer for helpful comments on the early stages of this manuscript.

## Chapter 5

# Delayed-shot migration in TEC coordinates

This chapter extends the analytical RWE approach discussed in Chapter 3 to 3D coordinate systems. I formulate an inline delayed-shot migration procedure in tilted elliptical-cylindrical (TEC) coordinate systems. When inline coordinate tilt angles are well-matched to the inline source ray parameters, the TEC coordinate extension affords accurate propagation of both steep-dip and turning-wave components. I show that wavefield extrapolation in TEC coordinates is no more complicated than propagation in elliptically anisotropic media. Impulse response tests illustrate the accuracy and lack of numerical anisotropy of the implemented scheme. I apply this approach to a realistic 3D wide-azimuth synthetic derived from a field Gulf of Mexico data set. The resulting images demonstrate the imaging advantages made possible through 3D RWE implementations, including the improved imaging of steeply dipping salt flanks, potentially at a reduced computational cost. Narrow-azimuth migration results demonstrate the applicability of the approach to typical Gulf of Mexico field data.

## INTRODUCTION

Wave-equation migration (WEM) methods routinely generate accurate seismic images in areas of complex geology. One common class of WEM approaches is shot-profile migration using one-way wavefield extrapolation. The first shot-profile migration step is to specify source and receiver wavefields that consist of modeled point sources and an individual shot profile, respectively. The migration algorithm propagates these two wavefields through the velocity model and correlates them at each extrapolation step to form an image. Although this procedure generates high-quality migration results, two drawbacks make shot-profile migration a less-than-ideal strategy. The first issue is that each individual shot migration requires a large aperture to propagate energy to wide offsets. The second drawback is that one migrates each shot record individually, which can be computationally expensive for large surveys with a high shot density.

One way to make the shot-profile style of WEM more efficient is to migrate a reduced number of composite source and receiver profiles each covering a broader aperture. For example, one can image a number of shot profiles simultaneously on the same migration domain. The key idea is that one makes a computationally advantageous trade-off of a broader migration aperture for a reduced number of shots. Shot-profile migration with composite wavefields, though, leads to the mixing of information from different shots and generates image crosstalk. A number of authors address this problem using a variety of phase-encoding migration approaches (????), that minimize the deleterious crosstalk effects.

Plane-wave migration (PWM) is one technique for reducing total migration cost using composite wavefields (??????). As originally demonstrated by ?, the key idea is to synthesize from the full wavefield volume the set of composite receiver wavefields that would have been recorded were a planar source function used. Generally, the number of synthesized wavefields is fewer than the corresponding number of shot profiles. One generates PWM images by propagating the modeled planar source and composite receiver wavefields through the velocity and computing a (weighted) correlation. ? and ? demonstrate that PWM is equivalent to shot-profile migration in

the limit where one uses many plane waves with well-sampled plane-wave dip spectra. ? also prove that 3D PWM is equivalent to conical-wave migration of individual sail lines synthesized as inline composite wavefields. The approach is termed conical wave because the source wavefronts form conic sections (in constant media) for non-zero inline plane-wave ray parameters.

The migration of plane- and conical-wave data, though more efficient than shot-profile migration, is similarly restricted in accuracy by one-way wavefield extrapolation assumptions. The most common limitation is a difficulty in propagating waves at large angles and turning waves by design, both of which are important for accurately imaging salt flanks in complex geologic areas. ? circumvent this problem by implementing 3D PWM in tilted Cartesian meshes. This coordinate system effectively orients the wavefield extrapolation axis toward the plane-wave take-off vector, enabling more accurate bulk propagation of plane-wave energy. One logistical complication of performing fully 3D PWM is that it requires propagating image-space-sized data volumes on a number of meshes tilting in both the inline and cross-line directions. This leads to a number of computational issues associated with the significant memory footprint.

This chapter presents an alternate phase-encoding approach that similarly uses alternative coordinate systems. The key differences between the work herein and that of ? are two-fold. The first difference is that I phase encode only according to the inline source coordinate, leading to the inline delayed-shot migration algorithm. This leads to a straightforward coarse-grain parallelization of the migration tasks across individual sail lines, where each migration has a significantly smaller aperture than the corresponding image-space-sized PWM volumes. A second efficiency gain over PWM is a reduction in the total number of migrations, because the number of sail lines is quite often fewer than the required number of cross-line plane waves. Thus, the inline-delayed shot approach has attractive computational advantages over the 3D PWM technique.

The second difference is that I perform the migration in tilted elliptical-cylindrical (TEC) coordinates, rather than tilted Cartesian meshes. TEC coordinate systems,

formed by concatenating a set of the 2D elliptical coordinates discussed in Chapter 3 along the invariant third axis, are well-suited for migrating individual sail lines. I orient the invariant and elliptical surfaces in the inline and cross-line directions, respectively. I extrapolate the inline delay-shot synthesized wavefield volumes outward on a series of elliptical-cylindrical shells. This allows source and receiver wavefields with zero inline dip to overturn in the cross-line direction, if necessary. I introduce an extra degree of freedom that permits the coordinate system to tilt along the invariant inline axis, thus enabling the propagation of turning waves inline. Consequently, inline delayed-shot migration in TEC coordinates allows wavefields with most non-zero dips to propagate and overturn to all azimuths as appropriate.

The chapter begins by examining 3D full-plane-wave and inline delayed-shot migration theory. I then introduce the TEC coordinate geometry and develop the corresponding wavenumber that forms the basis of the TEC wavefield extrapolation operator. I discuss the finite-difference extrapolation implementation and present the 3D impulse response. I apply the technique to a 3D wide-azimuth synthetic data set derived from real Gulf of Mexico velocity model to demonstrate the imaging advantages of 3D RWE migration. I then discuss the numerical costs associated with performing inline delayed-shot migration in TEC coordinates relative to Cartesian meshes. The chapter concludes with narrow-azimuth migration results demonstrate the applicability of the approach to typical Gulf of Mexico field data.

### 3D PLANE-WAVE MIGRATION

The full plane-wave and inline delayed-shot migration theory discussed herein draws largely from ?. I restate a number of key points for completeness, though with a slightly different notation. As in previous chapters, I define Cartesian coordinates by  $\mathbf{x} = [x_1, x_2, x_3]$  and a generalized coordinate system by  $\boldsymbol{\xi} = [\xi_1, \xi_2, \xi_3]$ .

## Full plane-wave phase-encoding migration

Performing 3D plane-wave migration is similar in many respects to 3D shot-profile migration. The main differences derive from how the composite source and receiver wavefield volumes,  $\overline{S}$  and  $\overline{R}$ , are re-synthesized from individual source and receiver profiles,  $S_{jk}$  and  $R_{lm}$ , prior to imaging. The complete wavefields are generated by filtering the source and receiver profiles by a function dependent on the inline and cross-line plane-wave ray parameters,  $\mathbf{p}_\xi = [p_{\xi_1}, p_{\xi_2}]$ . These wavefields are then propagated through the migration domain to generate the full source and receiver wavefield volumes

$$\overline{S}(\boldsymbol{\xi}|\omega) = \sum_{j=1}^A \sum_{k=1}^B S_{jk}(\boldsymbol{\xi}|\omega) f(\omega) e^{i\omega[p_{\xi_1} \Delta\xi_1 (j-p) + p_{\xi_2} \Delta\xi_2 (k-q)]}, \quad (5.1)$$

$$\overline{R}(\boldsymbol{\xi}|\omega) = \sum_{l=1}^A \sum_{m=1}^B R_{lm}(\boldsymbol{\xi}|\omega) f(\omega) e^{i\omega[p_{\xi_1} \Delta\xi_1 (l-p) + p_{\xi_2} \Delta\xi_2 (m-q)]}, \quad (5.2)$$

where  $f(\omega)$  is a frequency filter to be discussed below,  $\Delta\xi_1$  and  $\Delta\xi_2$  are the inline and cross-line sampling intervals,  $p$  and  $q$  are reference spatial indices in the inline and cross-line directions,  $j$  and  $k$  are indices fixing the inline and crossline source position,  $l$  and  $m$  are indices fixing the inline and cross-line receiver position, and  $A$  and  $B$  are the number of inline and cross-line source records, respectively. The phase encoding, implemented at the surface independent of wavefield extrapolation, is valid for any generalized coordinate system. Note that the wavefield propagation throughout the migration volume in equations 5.1 and 5.2 is understood, and assumed to be governed by the wavefield propagation techniques described in Chapter 2.

An image volume  $I(\boldsymbol{\xi})$  is formed from a series of individual full plane-wave migration images,  $I^{PW}(\boldsymbol{\xi}|\mathbf{p}_\xi)$ , by correlating the composite plane-wave source and receiver wavefields and stacking the results over frequency. The plane-wave migration kernel

mixes source and receiver wavefield energy,  $S_{jk}(\boldsymbol{\xi}|\omega)$  and  $R_{lm}(\boldsymbol{\xi}|\omega)$ , according to

$$\begin{aligned}
 I(\boldsymbol{\xi}) &= \sum_{p_{\xi_1}} \sum_{p_{\xi_2}} \sum_{j,l=1}^A \sum_{k,m=1}^B I_{jklm}^{PW}(\boldsymbol{\xi}|\mathbf{p}_{\boldsymbol{\xi}}) \\
 &= \sum_{p_{\xi_1}} \sum_{p_{\xi_2}} \sum_{j,l=1}^A \sum_{k,m=1}^B \sum_{\omega} |f(\omega)|^2 S_{jk}^*(\boldsymbol{\xi}|\omega) R_{lm}(\boldsymbol{\xi}|\omega) e^{i\omega[p_{\xi_1} \Delta\xi_1(j-l) + p_{\xi_2} \Delta\xi_2(k-m)]},
 \end{aligned} \tag{5.3}$$

where \* indicates complex conjugate.

Generally, mixing wavefields of differing  $S_{jk}$  and  $R_{lm}$  indices introduces image crosstalk. A plane-wave migration image will be crosstalk-free, though, in the following limits:

$$\begin{aligned}
 \lim_{N_{p_{\xi_1}} \rightarrow \infty} \sum_{\alpha=-N_{p_{\xi_1}}}^{N_{p_{\xi_1}}} e^{i\omega\alpha\Delta p_{\xi_1}\Delta\xi_1(j-l)} &= |\omega|^{-1} \delta_{jl}, \\
 \lim_{N_{p_{\xi_2}} \rightarrow \infty} \sum_{\alpha=-N_{p_{\xi_2}}}^{N_{p_{\xi_2}}} e^{i\omega\alpha\Delta p_{\xi_2}\Delta\xi_2(k-m)} &= |\omega|^{-1} \delta_{km}.
 \end{aligned} \tag{5.4}$$

where  $N_{p_{\xi_1}}$  and  $N_{p_{\xi_2}}$  are the number of plane waves in the  $\xi_1$  and  $\xi_2$  directions. Assuming that equation 5.4 approximately is valid (i.e., for large values of  $N_{p_{\xi_1}}$  and  $N_{p_{\xi_2}}$ ), I rewrite equation 5.3 as

$$I(\boldsymbol{\xi}) \approx \sum_{j=1}^A \sum_{k=1}^B \sum_{\omega} |f(\omega)|^2 |\omega|^{-2} S_{jk}^*(\boldsymbol{\xi}|\omega) R_{jk}(\boldsymbol{\xi}|\omega), \tag{5.5}$$

which, by defining  $|f(\omega)|^2 = |\omega|^2$ , generates the following expression:

$$I(\boldsymbol{\xi}) \approx \sum_{j=1}^M \sum_{k=1}^N \sum_{\omega} S_{jk}^*(\boldsymbol{\xi}|\omega) R_{jk}(\boldsymbol{\xi}|\omega). \tag{5.6}$$

This demonstrates the equivalence between plane-wave and shot-profile migration (?).

## Inline delayed-shot migration

An alternate 3D migration formulation is to phase-encode individual sail lines for a given ray parameter,  $p_{\xi_1}$ , solely according to inline source position. This phase-encoding approach is related to conical-wave migration, which requires  $j - l = 0$  in equation 5.3. However, I choose to not make this restriction because it is realized only by straight sail lines and non-flip-flop sources (?). Rather, I present an alternative theory of inline delayed-shot migration that allows more general crossline source and receiver distribution.

Inline delayed-shot wavefields, propagated through the migration domain to generate the full source and receiver wavefield volumes, are defined by

$$\overline{S(\boldsymbol{\xi}|\omega)} = \sum_{l=1}^A \sum_{j=1}^B S_{jl}(\boldsymbol{\xi}|\omega) f(\omega) e^{i\omega[p_{\xi_1} \Delta\xi_1(j-p)]}, \quad (5.7)$$

$$\overline{R(\boldsymbol{\xi}|\omega)} = \sum_{l=1}^A \sum_{k=1}^B R_{kl}(\boldsymbol{\xi}|\omega) f(\omega) e^{i\omega[p_{\xi_1} \Delta\xi_1(k-p)]}, \quad (5.8)$$

where  $j$  and  $k$  are the source and receiver inline position, respectively,  $B$  is the number of inline records,  $l$  is the sail line index out of a total of  $A$  sail lines, and  $p$  is a reference inline index.

An image volume  $I(\boldsymbol{\xi})$  is generated from a series of inline delayed-shot migration images,  $I_l^{DS}(\boldsymbol{\xi}|p_{\xi_1})$ , formed by correlating the composite inline source and receiver wavefields and stacking the results over frequency. The inline delayed-shot migration kernel mixes source and receiver wavefield energy,  $S_{jl}(\boldsymbol{\xi}|\omega)$  and  $R_{kl}(\boldsymbol{\xi}|\omega)$ , according to

$$\begin{aligned} I(\boldsymbol{\xi}) &= \sum_{l=1}^A \sum_{p_{\xi_1}} \sum_{j=1}^B \sum_{k=1}^B I_{jkl}^{DS}(\boldsymbol{\xi}|p_{\xi_1}) \\ &= \sum_{l=1}^A \sum_{p_{\xi_1}} \sum_{j=1}^B \sum_{k=1}^B \sum_{\omega} |f(\omega)|^2 S_{jl}^*(\boldsymbol{\xi}|\omega) R_{kl}(\boldsymbol{\xi}|\omega) e^{i\omega[p_{\xi_1} \Delta\xi_1(j-k)]}, \end{aligned} \quad (5.9)$$

Similar to plane-wave migration, mixing wavefields of differing  $S_{jl}$  and  $R_{kl}$  indices will introduce crosstalk into the image volume. However, inline delayed-shot migration will be crosstalk-free in the following limit:

$$\lim_{N_{p\xi_1} \rightarrow \infty} \sum_{\alpha=-N_{p\xi_1}}^{N_{p\xi_1}} e^{i\omega\alpha\Delta p_{\xi_1}\Delta\xi_1(j-k)} = |\omega|^{-1}\delta_{jk}, \quad (5.10)$$

Defining  $|f(\omega)|^2 = |\omega|$  and using the approximation in equation 5.10, I rewrite

$$I_l^{DS}(\boldsymbol{\xi}) \approx \sum_{j=1}^B \sum_{\omega} S_{jl}^*(\boldsymbol{\xi}|\omega)R_{jl}(\boldsymbol{\xi}|\omega). \quad (5.11)$$

Stacking over all inline delayed-shot sail-line migration results yields the full image volume,

$$I(\boldsymbol{\xi}) \approx \sum_{l=1}^A I_l^{DS}(\boldsymbol{\xi}) \approx \sum_{l=1}^A \sum_{j=1}^B \sum_{\omega} S_{jl}^*(\boldsymbol{\xi}|\omega)R_{jl}(\boldsymbol{\xi}|\omega). \quad (5.12)$$

This proves the equivalence of inline delayed-shot and shot-profile migration.

## TILTED ELLIPTICAL-CYLINDRICAL COORDINATES

One question to be addressed is what coordinate system geometry optimally conforms to the impulse response of a conical wavefield? I assert that the best geometry is that of the TEC coordinate system shown in Figures 5.1 and 5.2. One advantage is that the breadth of the first extrapolation step at the surface allows multiple streamers of a single sail line to be positioned directly on a single mesh. Hence, this geometry is applicable to both narrow- and wide-azimuth acquisition. A second advantage is that one direction of large-angle propagation can be handled by coordinate system tilting, while the other is naturally handled by the ellipticity of the mesh. (Note that the geometry of another natural mesh - cylindrical polar coordinates - would not be a judicious choice for because the geometry permits migration of only single-streamer data and has singular points located on the surface at the first extrapolation step.)

I set up the migration geometry of the elliptical-cylindrical mesh as follows:

- $\xi_3 \in [0, \infty]$  is the extrapolation direction, where surfaces of constant  $\xi_3$  form concentric elliptical cylinders, shown in Figure 5.1a.
- $\xi_2 \in [0, 2\pi)$  is the crossline direction, where surfaces of constant  $\xi_2$  are folded hyperbolic planes, shown in Figure 5.1b; and
- $\xi_1 \in [-\infty, \infty]$  is the inline direction, where surfaces of constant  $\xi_1$  are 2D elliptical coordinate meshes, shown in Figure 5.1c;

The mapping relationship between the two coordinate systems, adapted from ?, is

$$\begin{bmatrix} x_1 \\ x_2 \\ x_3 \end{bmatrix} = \begin{bmatrix} \xi_1 \cos \theta - a \sinh \xi_3 \sin \xi_2 \sin \theta \\ a \cosh \xi_3 \cos \xi_2 \\ \xi_1 \sin \theta + a \sinh \xi_3 \sin \xi_2 \cos \theta \end{bmatrix}, \quad (5.13)$$

where  $\theta$  is the inline tilt angle of the coordinate system and parameter  $a$  controls the coordinate system breadth. Panels 5.2a and 5.2b show the TEC coordinate system at  $0^\circ$  and  $25^\circ$  tilt angles, respectively.

### TEC extrapolation wavenumber

A metric tensor  $g_{jk}$  can be specified from the mapping relationship given in equations 5.13:

$$[g_{jk}] = \begin{bmatrix} 1 & 0 & 0 \\ 0 & A^2 & 0 \\ 0 & 0 & A^2 \end{bmatrix}, \quad (5.14)$$

where  $A = a\sqrt{\sinh^2 \xi_3 + \sin^2 \xi_2}$ . The determinant of the metric tensor is:  $|\mathbf{g}| = A^4$ . The corresponding inverse weighted metric tensor,  $m^{jk}$  as developed in Chapter 2, is

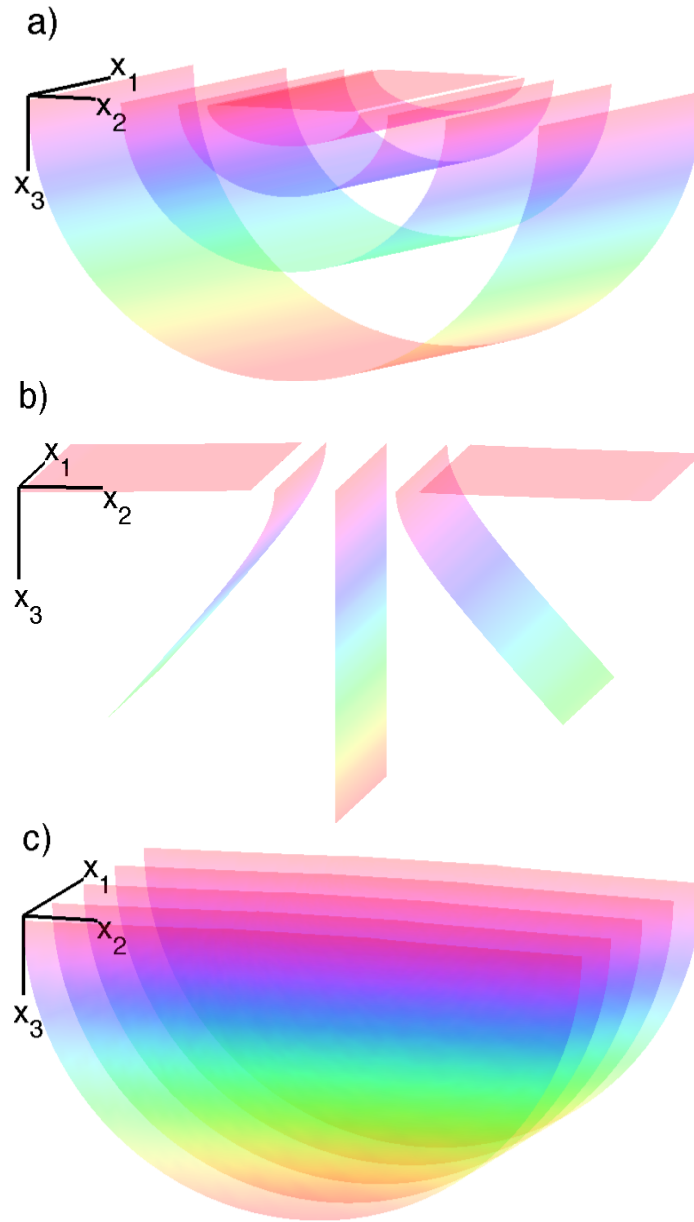


Figure 5.1: Constant surfaces of the elliptical-cylindrical coordinate system (with zero inline tilt). Cartesian coordinate axes are given by the vector diagram. a) constant  $\xi_3$  surfaces forming confocal elliptical-cylindrical shells that represent the direction of extrapolation direction. b) constant  $\xi_2$  surfaces representing folded hyperbolic planes. c) constant  $\xi_1$  surfaces representing 2D elliptical meshes. **NR** conical/. TECgeom

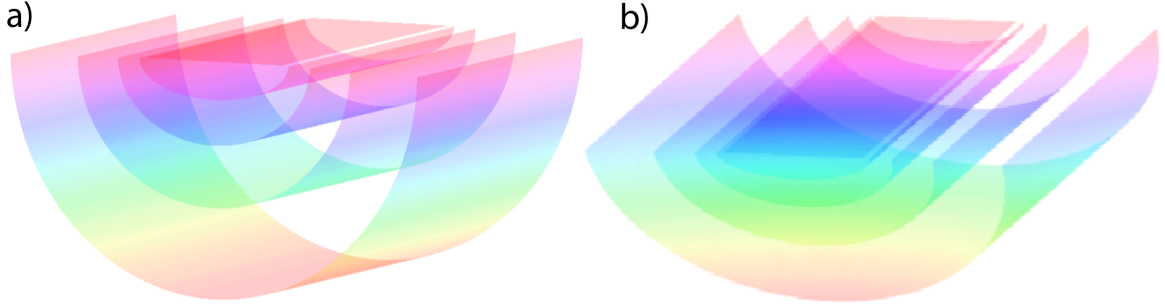


Figure 5.2: Four extrapolation steps in  $\xi_3$  of an TEC coordinate system, where the  $\xi_1$  and  $\xi_2$  coordinate axes are oriented in the inline and crossline directions, respectively. a)  $0^\circ$  tilt angle. b)  $25^\circ$  tilt angle. **NR** conical/. TEC

given by:

$$[m^{jk}] = \begin{bmatrix} A^2 & 0 & 0 \\ 0 & 1 & 0 \\ 0 & 0 & 1 \end{bmatrix}. \quad (5.15)$$

Note that even though the metric of the TEC coordinate system varies spatially, the local curvature parameters ( $n^j = \frac{\partial m^{jk}}{\partial \xi_k}$ ) remain constant:  $n^1 = n^2 = n^3 = 0$ . The corresponding extrapolation wavenumber,  $k_{\xi_3}$ , can be generated by inputting tensor  $m^{jk}$  and fields  $n^j$  into the general wavenumber expression for 3D non-orthogonal coordinate systems in equation 2.9

$$k_{\xi_3} = \pm \sqrt{A^2 s^2 \omega^2 - A^2 k_{\xi_1}^2 - k_{\xi_2}^2}, \quad (5.16)$$

where  $s$  is the slowness (reciprocal of velocity),  $k_{\xi_3}$  is the extrapolation wavenumber, and  $k_{\xi_1}$  and  $k_{\xi_2}$  are the inline and crossline wavenumbers, respectively.

The wavenumber specified in equation 5.16 is central to the inline delayed-shot migration algorithm. The first step is to extrapolate the source and receiver wavefields

$$E_{\xi_3}[S_{jl}(\xi_3, \xi_1, \xi_2|\omega)] = S_{jl}(\xi_3 + \Delta\xi_3, \xi_1, \xi_2|\omega), \quad (5.17)$$

$$E_{\xi_3}^*[R_{kl}(\xi_3, \xi_1, \xi_2|\omega)] = R_{kl}(\xi_3 + \Delta\xi_3, \xi_1, \xi_2|\omega), \quad (5.18)$$

where  $E_{\xi_3}[\cdot]$  and  $E_{\xi_3}^*[\cdot]$  are the extrapolation operator and its conjugate, respectively. The results herein were computed using the  $\omega - \xi$  finite-difference extrapolators discussed below. The second step involves summing the individual inline delayed-shot images contributions,  $I_{jk}^{DS}(\boldsymbol{\xi})$ , into the total image volume,  $I(\boldsymbol{\xi})$  according to equation 5.12.

### 3D IMPLICIT FINITE-DIFFERENCE EXTRAPOLATION

One obvious concern is whether the dispersion relationship in equation 5.16 can be implemented accurately and efficiently in a wavefield extrapolation scheme. I address this question by comparing the elliptical-cylindrical dispersion relationship to that for elliptically anisotropic media in Cartesian coordinates. By defining an effective slowness  $s_A = As$  and rewriting equation 5.16 as

$$\frac{k_{\xi_3}}{\omega s_A} = \sqrt{1 - A^2 \frac{k_{\xi_1}^2}{\omega^2 s_A^2} - \frac{k_{\xi_2}^2}{\omega^2 s_A^2}}, \quad (5.19)$$

the TEC coordinate dispersion relationship resembles that of elliptically anisotropic media (?). More specifically, extrapolation in TEC coordinates is related to a special case where the Thomsen parameters (?) obey  $\epsilon = \delta$ :

$$\left. \frac{k_{x_3}}{\omega s} \right|_{\epsilon=\delta} = \sqrt{\left. \frac{1 - (1 + 2\epsilon) \frac{k_{x_1}^2 + k_{x_2}^2}{\omega^2 s^2}}{1 - 2(\epsilon - \delta) \frac{k_{x_1}^2 + k_{x_2}^2}{\omega^2 s^2}} \right|_{\epsilon=\delta}} = \sqrt{1 - (1 + 2\epsilon) \frac{k_{x_1}^2}{\omega^2 s^2} - (1 + 2\epsilon) \frac{k_{x_2}^2}{\omega^2 s^2}}. \quad (5.20)$$

From equation 5.20 we see that equation 5.16 is no more complex than the dispersion relationship for propagating waves in elliptically anisotropic media, which is now routinely handled with finite-difference approaches (???).

A general approach to 3D implicit finite-difference propagation is to approximate the square-root by a series of rational functions (?)

$$S_{\xi_3} = \sqrt{1 - A^2 S_{\xi_1}^2 - S_{\xi_2}^2} \approx \sum_{j=1}^n \frac{a_j S_r^2}{1 - b_j S_r^2}, \quad (5.21)$$

Coeff. order $j$	Coeff. $a_j$	Coeff. $b_j$
1	0.040315157	0.873981642
2	0.457289566	0.222691983

Table 5.1: Coefficients used in 3D implicit finite-difference wavefield extrapolation.

where  $S_{\xi_j} = \frac{k_{\xi_j}}{\omega s_A}$  and  $S_r^2 = A^2 S_{\xi_1}^2 + S_{\xi_2}^2$ , for  $j = 1, 2, 3$ , and  $n$  is the order of the coefficient expansion.

An optimal set of coefficients can be found by solving an optimization problem (?),

$$E(a_j, b_j) = \min \int_0^{\sin\phi} \left[ \sqrt{1 - S_r^2} - \sum_{j=1}^n \frac{a_j S_r^2}{1 - b_j S_r^2} \right]^2 dS_r, \quad (5.22)$$

where  $\phi$  is the maximum optimization angle. I generated the following results using a 4th-order approximation and coefficients found in Table 5.1 (?).

Specifying a finite-difference extrapolator operator using the 4th-order approximation is equivalent to solving a cascade of partial differential equations (?)

$$\begin{aligned} \frac{\partial}{\partial \xi_3} U_{\xi_3 + \Delta \xi_3 / 3} &= i\omega s U_{\xi_3}, \\ \frac{\partial}{\partial \xi_3} U_{\xi_3 + 2\Delta \xi_3 / 3} &= i\omega s \left[ \frac{\frac{a_1}{\omega^2 s^2} \frac{\partial^2}{\partial \xi_1^2}}{1 + \frac{b_1}{\omega^2 s^2} \frac{\partial^2}{\partial \xi_1^2}} + \frac{\frac{a_1}{\omega^2 s_A^2} \frac{\partial^2}{\partial \xi_2^2}}{1 + \frac{b_1}{\omega^2 s_A^2} \frac{\partial^2}{\partial \xi_2^2}} \right] U_{\xi_3 + \Delta \xi_3 / 3}, \\ \frac{\partial}{\partial \xi_3} U_{\xi_3 + \Delta \xi_3} &= i\omega s \left[ \frac{\frac{a_2}{\omega^2 s^2} \frac{\partial^2}{\partial \xi_1^2}}{1 + \frac{b_2}{\omega^2 s^2} \frac{\partial^2}{\partial \xi_1^2}} + \frac{\frac{a_2}{\omega^2 s_A^2} \frac{\partial^2}{\partial \xi_2^2}}{1 + \frac{b_2}{\omega^2 s_A^2} \frac{\partial^2}{\partial \xi_2^2}} \right] U_{\xi_3 + 2\Delta \xi_3 / 3}. \end{aligned} \quad (5.23)$$

I solve these equations implicitly at each extrapolation step by a finite-difference splitting approach that alternatively advances the wavefield in the  $\xi_1$  and  $\xi_2$  directions. Splitting methods allow the direct application of the  $A$  scaling factor in equation 5.21 by introducing the original slowness model,  $\frac{s_A}{A} = s$ , for the  $\xi_1$  direction split.

One drawback to finite-difference splitting methods is that they commonly generate numerical anisotropy. To minimize these effects, I apply a Fourier-domain

phase-correction filter  $L[\cdot]$  (?)

$$L[U] = U e^{i\Delta\xi_3 k_L}, \quad (5.24)$$

where

$$k_L = \sqrt{1 - \frac{k_{\xi_1}^2}{(\omega s_1^r)^2} - \frac{k_{\xi_2}^2}{(\omega s_2^r)^2}} - \left[ 1 - \sum_{j=1}^2 \left( \frac{a_j \left(\frac{k_{\xi_1}}{\omega s_1^r}\right)^2}{1 - b_j \left(\frac{k_{\xi_1}}{\omega s_1^r}\right)^2} - \frac{a_j \left(\frac{k_{\xi_2}}{\omega s_2^r}\right)^2}{1 - b_j \left(\frac{k_{\xi_2}}{\omega s_2^r}\right)^2} \right) \right], \quad (5.25)$$

and  $s_1^r$  and  $s_2^r$  are reference slownesses chosen to be the mean value of  $s_{eff}^A$  and  $s$  defined above, respectively. Note that while this phase-shift correction is explicitly correct for  $v(\xi_3)$  media, the Li filter in  $v(\xi_3, \xi_1, \xi_2)$  media is only approximate and will introduce error.

## Impulse response tests

I conducted impulse response tests on a 500x400x400 cube in a homogeneous medium of slowness  $s = 0.0005 \text{ sm}^{-1}$ . The initial wavefield consisted of three horizontally smoothed point sources at  $t=0.5, 0.75,$  and  $1 \text{ s}$ . The impulse responses are expected to consist of three hemispherical surfaces of radii  $r=1000, 1500,$  and  $2000 \text{ m}$ .

Figures 5.3a and 5.3b show the inline and crossline responses. The three lines overlying the analytic curves show the correct impulse response locations. Note that the impulse responses are restricted at large angles both by the coordinate system boundaries and by the 50 sample cosine-taper function along the edges of the TEC mesh. Figure 5.4 shows a impulse response slice extracted at 1300 m depth. The symmetric response indicates that the numerical anisotropy from the numerical splitting is accounted for by the Li phase-correction filter.

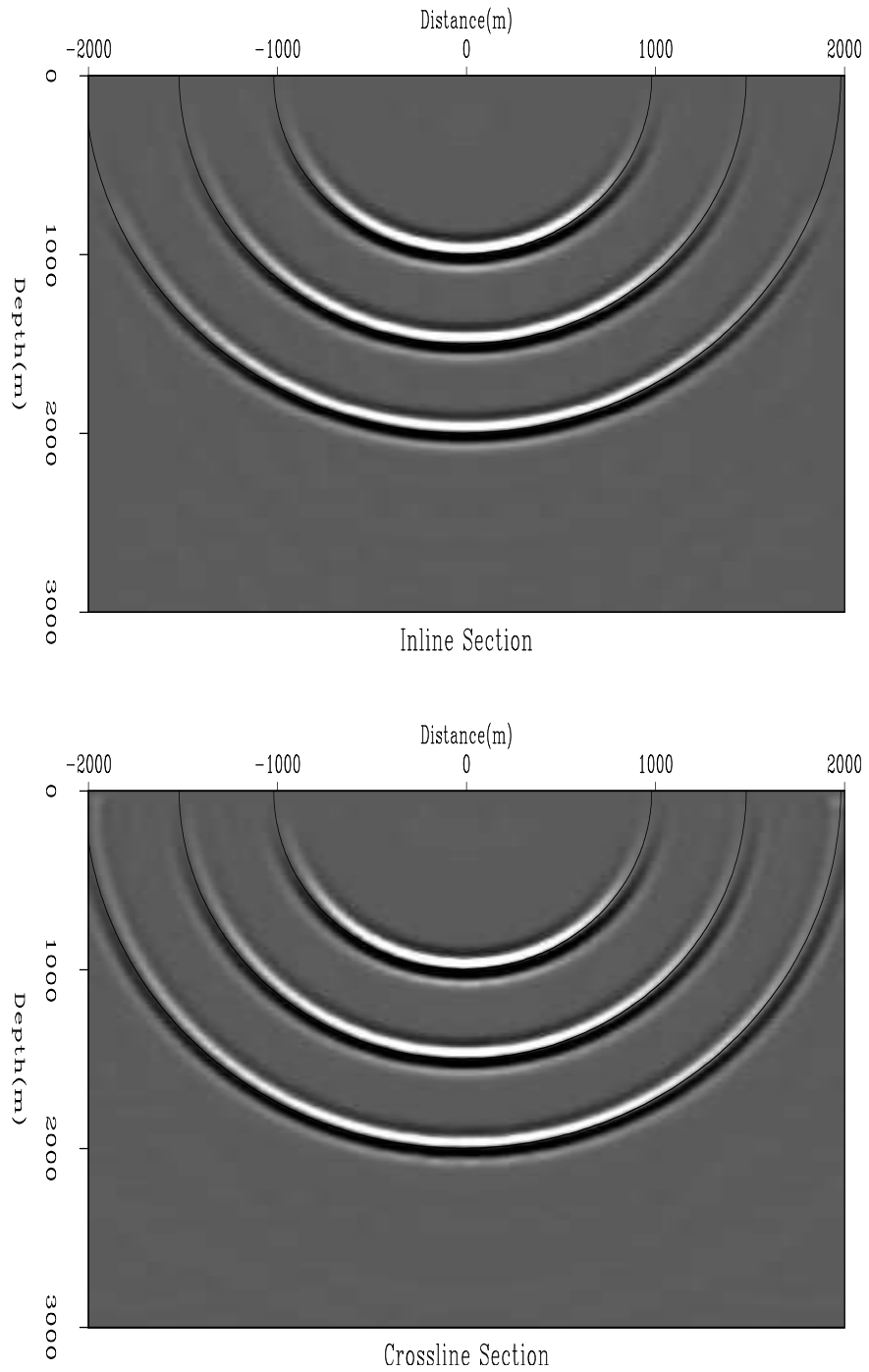
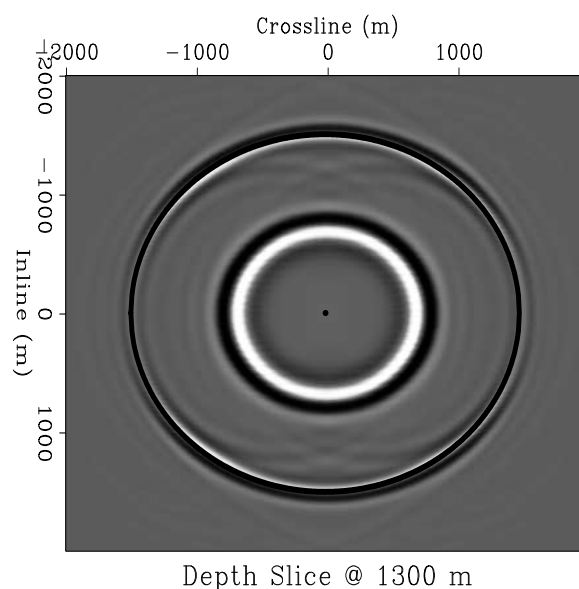


Figure 5.3: Elliptical-cylindrical-coordinate impulse-response tests. a) Inline section. b) Crossline section. **CR**  conical/.  CrossIn

Figure 5.4: Elliptical-cylindrical impulse response at 1300 m depth. Note the circular symmetry of the impulse response indicating little-to-no numerical anisotropy. **CR**

conical/. Depth1300



### 3D WIDE-AZIMUTH SYNTHETIC TESTS

This section presents the inline delayed-shot migration algorithm test results on a wide-azimuth synthetic data set generated from a realistic 3D Gulf of Mexico velocity model. Figure 5.5 presents some depth slices and sections through the model. The velocity model is comprised of typical Gulf of Mexico sedimentary profile with a velocity gradient of approximately  $0.2 \text{ s}^{-1}$ , with a number of salt bodies of complex 3D geometry characterized by smoothly varying salt tops and steep flanks below overhangs. Key imaging targets include the steep salt flanks and the on-lapping sedimentary units that comprise the likely exploration areas.

Table 5.2 summarizes the acquisition geometry of the data set. The data used for migration consisted of 72 sail lines separated 250 m apart. Each sail line consists of 100 shots sampled at a 250 m shot interval. The receiver pattern for each shot record contains 321 inline samples with a maximum offset of  $\pm 8000$  m computed at a 50 m interval, and 161 crossline samples with a maximum offset of  $\pm 4000$  m at a 50 m interval.

A total of 192 frequencies were selected for migration starting at 1.42 Hz at a

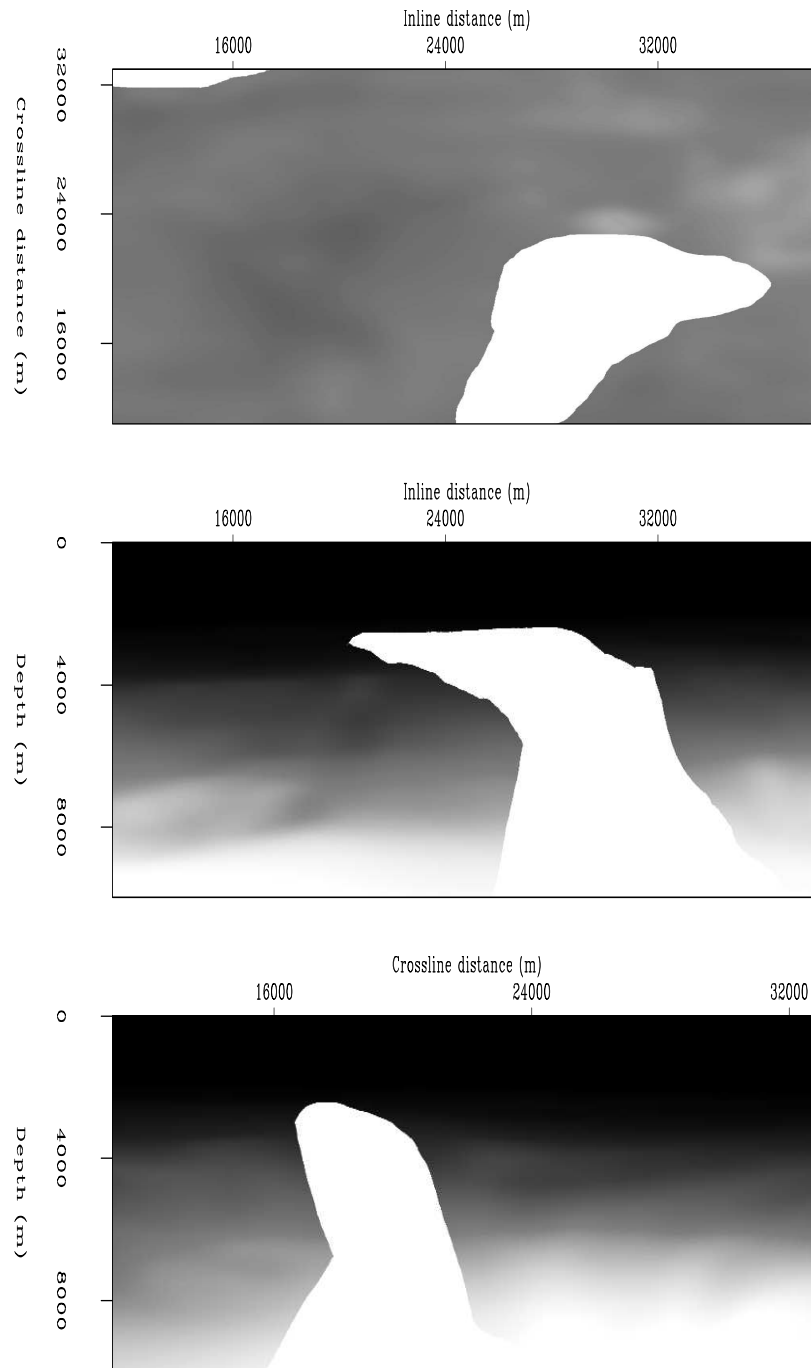


Figure 5.5: Depth section and inline crossline sections of the Gulf of Mexico velocity model through complex 3D salt bodies. Top: 3900 m depth slice. Middle: 33000 m inline section. Top: 16000 m crossline section. ER conical/. VELCUT

Source Parameter	Value	Receiver Parameter	Value
Number of sail lines	72	Max. inline offset (m)	$\pm 8000$
Sail line interval (m)	250	Max. crossline offset (m)	$\pm 4000$
Shots per sail line	100	Inline receiver interval (m)	50
Shot interval (m)	250	Crossline receiver interval (m)	50

Table 5.2: Parameters associated with the 3D synthetic data set.

sampling rate of 0.075 Hz. Filtered data from each sail line data were transformed into a plane-wave data set by phase-encoding over a range of inline ray parameters,  $p_{\xi_1}$ . I selected a total of 101 inline ray parameters between  $\pm 8.33 \times 10^{-4} \text{ s m}^{-1}$  at a sampling rate of  $8.33 \times 10^{-6} \text{ s m}^{-1}$ . Given the  $1500 \text{ m s}^{-1}$  water velocities at the surface, the maximum values correspond to a surface take-off angle of  $\pm 38.7^\circ$ .

I applied the inline delayed-shot migration technique to the plane-wave data on a sail-line by sail-line basis, which allowed for a coarse-grain computational parallelism at a scripting level. (The migration code was also OMP-enabled, which led to a second level of coarse-grain parallelism over the frequency axis.) Migration runs were conducted for Cartesian coordinate (CC) and TEC geometries with both tilting and non-tilting meshes. For CC migrations, the data volumes were zero-padded with 40 samples on each inline side and 95 samples on each crossline side. The data volume for TEC migrations were padded with 40 samples on the inline sides, but only one sample on each crossline side because the coordinate system aperture expands naturally in the crossline direction.

Figure 5.6 presents the 15400 m cross section from the 24500 m sail-line migration image (for 101 plane-waves) for the TEC (top panel) and the CC (bottom panel) geometries. The gently dipping sedimentary reflections in both sections are imaged across a 6000 m swath. The TEC migration, relative to that in CC geometry, shows a significant improvement in the vertical salt flank on the right-hand-side of the image. Although the salt-flank is weakly present in the CC image under strong clipping, it is mis-positioned due to the  $80^\circ$  limit of extrapolation operator accuracy.

Figures 5.7 and 5.8 present crossline sections from the full TEC and CC image

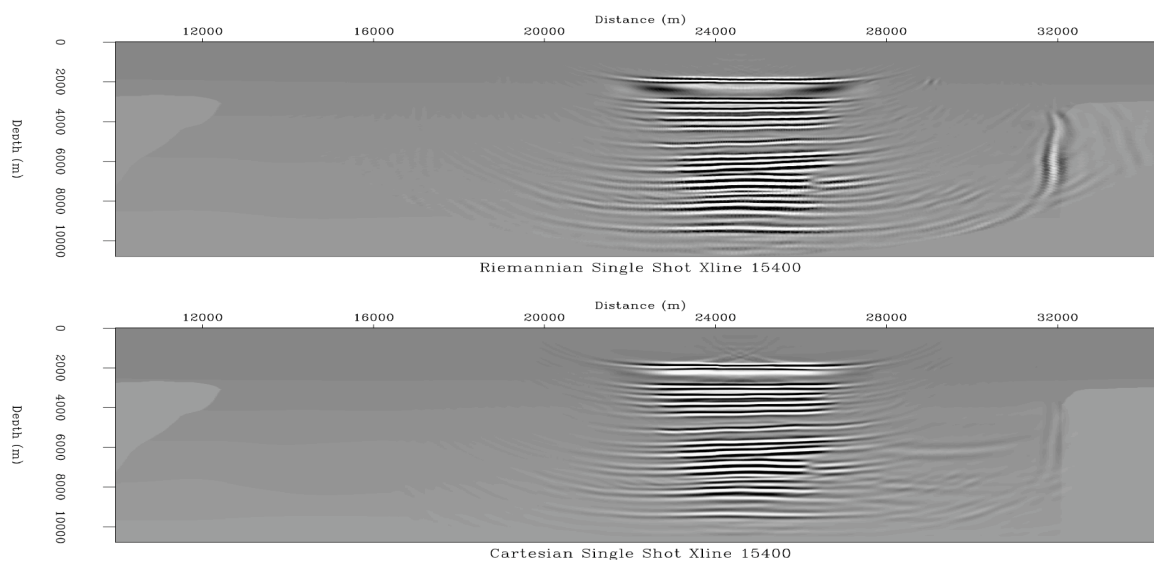


Figure 5.6: Sections for the 24500 m sail line at the 15400m crossline coordinate. Top: Elliptical-cylindrical coordinate image. Bottom: Cartesian coordinate image. NR conical/. TESTY15400

volumes. Figure 5.7 presents the EC and Cartesian crossline sections at the 33700 m inline coordinate in the upper and lower panels, respectively. The TEC image has an improved left-hand salt flank (marked A) that is more correctly positioned relative to the CC image. Similarly, the right-hand salt flank (marked B) is more accurately positioned and forms a more continuous reflector. Figure 5.8 presents the 15100 m crossline sections extracted from the two image volumes. Note the differences in the vertical right-hand salt flank (marked A) between the ECC (top panel) and CC (bottom panel) images. The TEC image exhibits a stronger reflector that is better positioned than that in the CC image (again because of the high-angle limits of the extrapolation operator).

Figure 5.9 shows the 21750 m inline section through the complete TEC (upper panel) and CC (lower panel) image volumes. The left-hand salt flank (marked A) is more accurately located and continuous in the TEC image. The right-hand salt flank (marked B), again, is more continuous in the TEC image. Another observation is that the TEC image (and in Figures 5.7-5.8) does not contain the same spatial

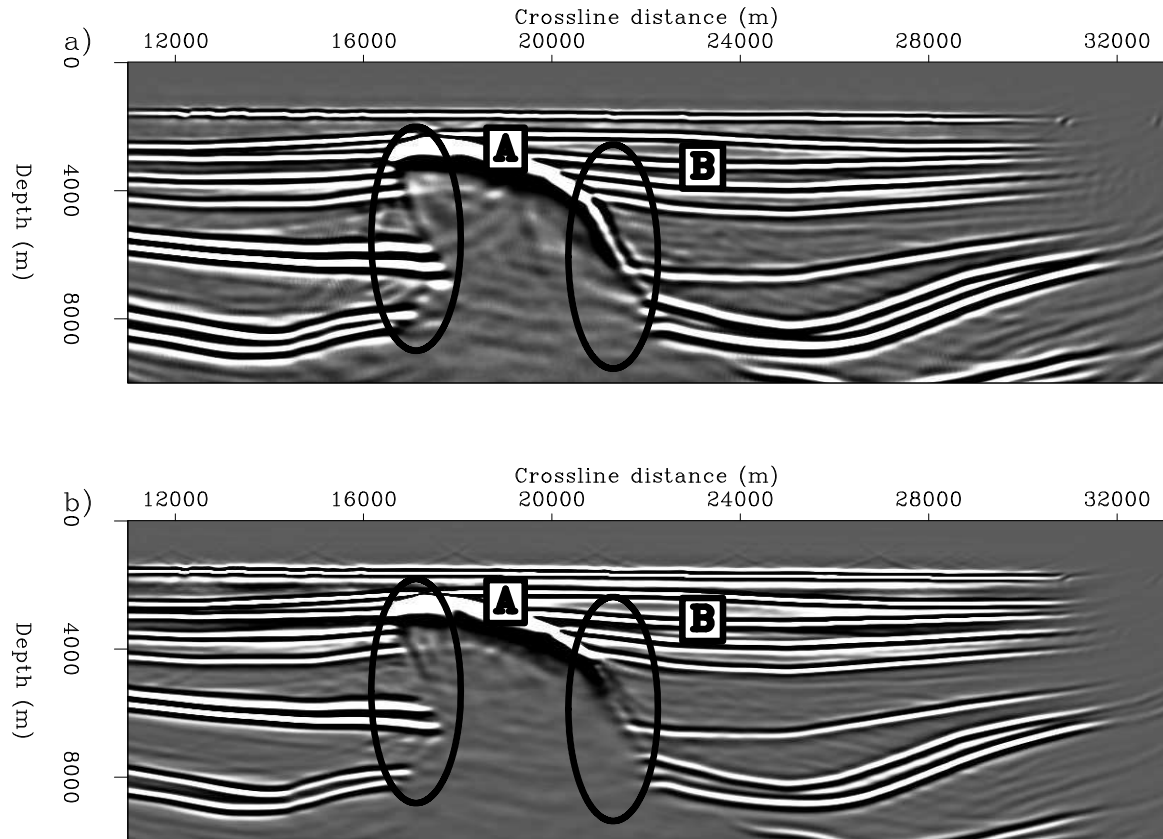


Figure 5.7: Crossline sections through the velocity model and full image volumes at inline coordinate 33700 m. Top panel: Elliptical-cylindrical coordinate image. Bottom panel: Cartesian coordinate image. The imaging improvements for the left-hand salt flank are denoted by the oval marked A. The oval marked B illustrates a more continuous and correctly placed reflector in the TEC coordinate system. **NR**  
conical/. FIG3

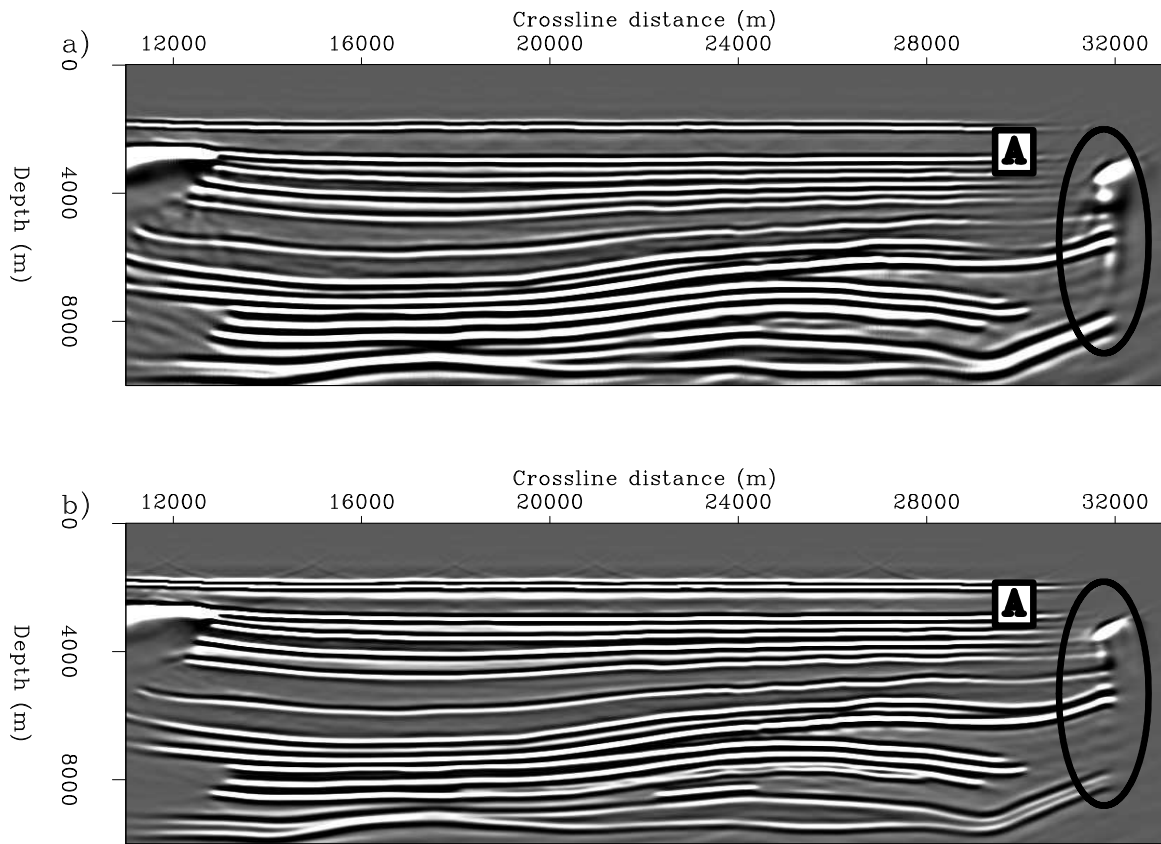


Figure 5.8: Crossline sections through the velocity model and full image volumes at inline coordinate 15100 m. Top panel: Elliptical-cylindrical coordinate image. Bottom panel: Cartesian coordinate image. The oval marked A indicates the location of the vertical salt flank that is better imaged in TEC coordinates. **NR** conical/. FIG4

frequency content as the CC images (see below).

Figure 5.10 presents slices extracted at 6150 m depth from the TEC (top panel) and CC (bottom panel) images. The images are again fairly similar, though there are slight differences that correspond to amplitude differences between the weakly imaged steep flank reflectors. Examples include the regions marked A and C that correspond to the salt flanks in Figure 5.9 and Figure 5.7, respectively. Finally, the migration algorithm has well-imaged the set of channels denoted in region B in both coordinate system images.

## Discussion

Relative computational cost is one important metric to consider when comparing the migration algorithms in different coordinate systems. In the above tests, padding in the crossline direction tended to be the most important factor in determining the migration run time. One benefit of the TEC geometry is its naturally outward-expanding mesh in the elliptical direction that effectively increases the migration aperture. Thus, TEC migrations usually require less zero-padding in the crossline direction relative to CC geometries. I performed the TEC migrations on meshes with inline-by-crossline-by-depth grids of 720x324x400. Migrations in CC geometries required a 720x512x400 mesh in order to achieve similar crossline aperture, which resulted in a fairly significant additional computational overhead.

Table 5.3 shows the comparative costs for various TEC and CC migration runs for both the shot-profile and delayed-shot migration styles. I used 72 data points in specifying each median runtime times for the four different migration runs. The test migrations indicate that the TEC geometry migrations were faster than the those in Cartesian tests (for equivalent effective aperture), with 29% and 21% computational cost reduction for the shot-profile and inline delayed-shot migration strategies, respectively.

One question worth addressing is how far can the TEC sampling be reduced before imaging artifacts become apparent? As one moves outward between successive

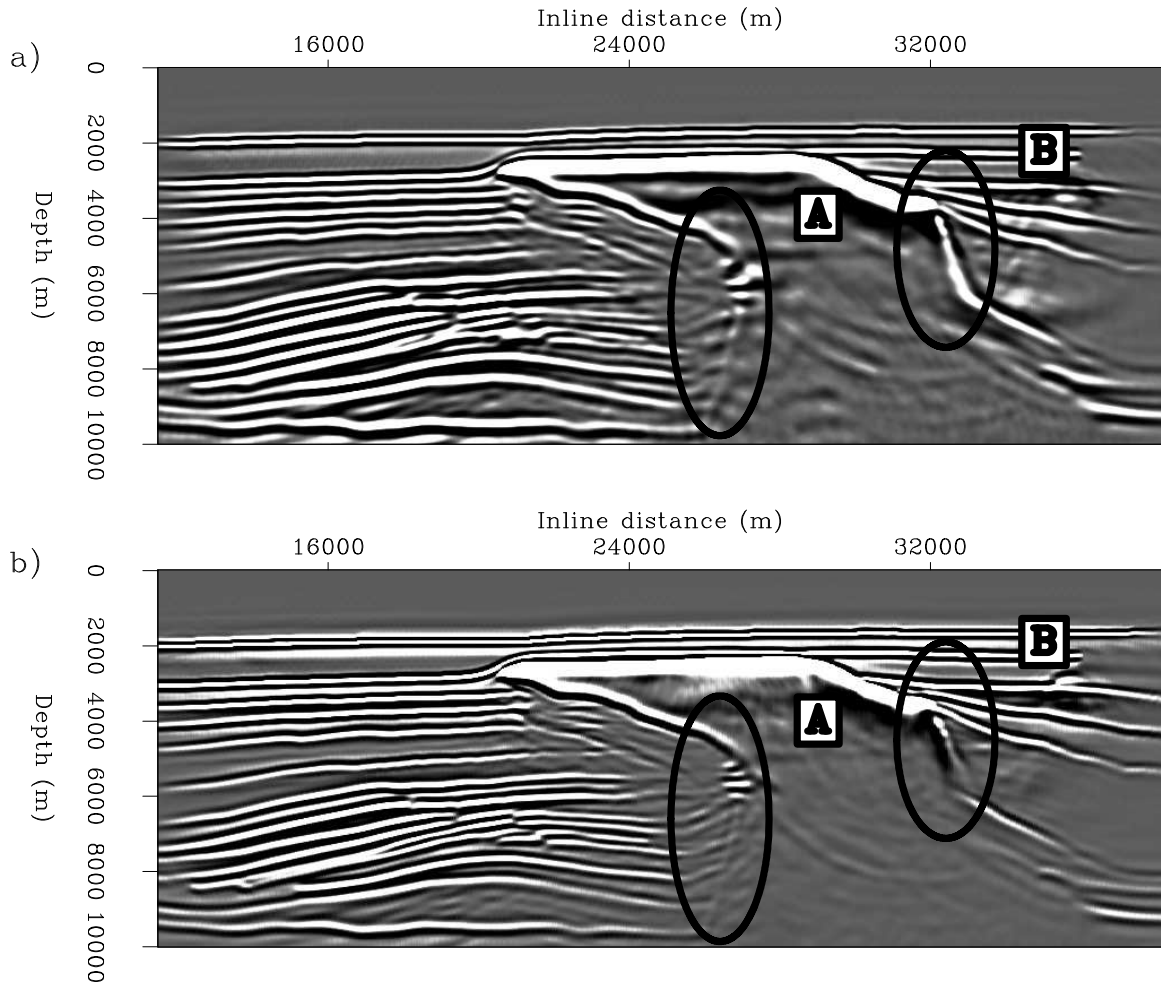


Figure 5.9: Inline sections through the velocity model and full image volumes at crossline coordinate 21750 m. Top panel: Velocity section. Middle panel: Elliptical-cylindrical coordinate image. Bottom panel: Cartesian coordinate image. The left-hand salt flank, shown in oval A, is more accurately positioned in the TEC coordinate image, while the right-hand flank, marked by oval B, is similarly more accurately positioned and continuous. **NR** conical/. FIG1

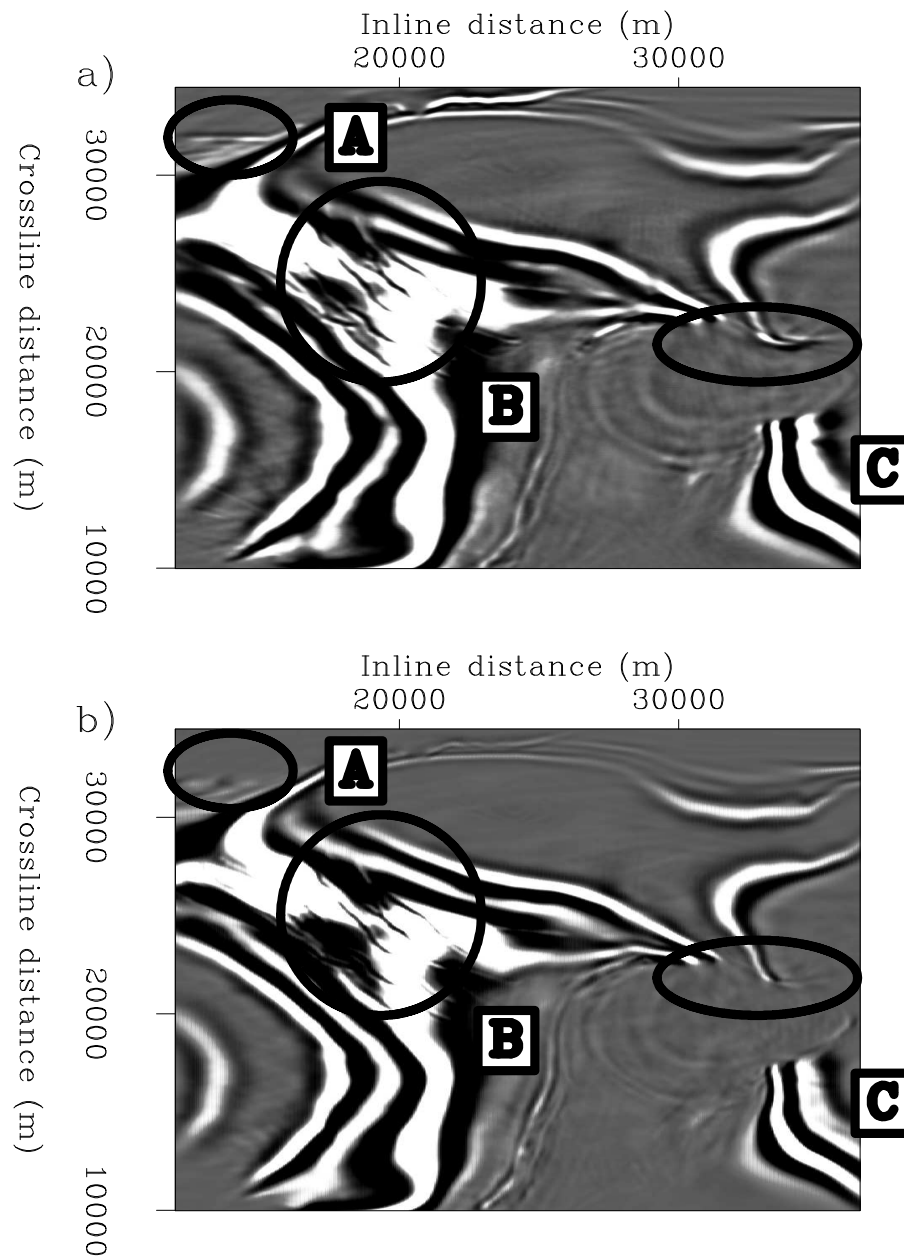


Figure 5.10: Depth slices through the velocity model and image volumes at 6150 m depth. Top panel: Elliptical-cylindrical coordinate image. Bottom panel: Cartesian coordinate image. Oval A illustrates the improved TEC image for the vertical salt flank shown in Figure 5.8. Oval B demarcates a region where some of the smaller-scale fractures are well imaged in both images. Oval C shows the region where the near-vertical flank shown in TEC coordinate image in Figure 5.7 is better imaged. NR conical/. FIG5

Migration style	Coordinate system	Mean run time (hrs)
Plane-wave	Tilted elliptical cylindrical	37.2
Plane-wave	Cartesian	45.0
Shot-profile	Tilted elliptical cylindrical	15.5
Shot-profile	Cartesian	20.0

Table 5.3: Run-time comparisons for the delayed-shot migration and shot-profile styles in the tilted elliptical-cylindrical and Cartesian coordinate systems.

extrapolation surfaces, the TEC geometry expands at increasingly larger step sizes. Fortunately, most realistic velocity models have velocity increasing with depth, causing the wavelengths of the propagated waves to lengthen. This phenomenon acts as a natural wavefield filter that, in most cases, prevents wavenumbers from aliasing (except near-surface in the grid extremities). A good rule-of-thumb is that one must ensure that the grid point of TEC coordinate system mesh does not go below one grid point for every two CC grid points in each direction; however, maintaining this relationship throughout the image volume is not a straightforward task. Additional work on the craft of 3D coordinate-system interpolation is necessary and would likely help restore some of the absent high frequency information.

An additional consideration of parameter choice is the interpolation window over which the surface wavefields are injected onto the TEC coordinate mesh. Not using a sinc-based interpolation over the near-surface depth axis can lead to significant artifacts; however, choosing too large of a window will blend information from different extrapolation steps leading to smoother and lower frequency images. Figures 5.7-5.10 show the result of a somewhat overcautious parameter choice (interpolating wavefields three additional depth steps) that led to the lower spatial wavenumber content of the TEC images relative to the CC images. I assert that this effective low-pass filtering can be reduced by interpolating only one or two additional steps in depth.

### NARROW-AZIMUTH FIELD DATA TEST

This section presents the results of applying the inline delayed-shot imaging procedure to a 3D Gulf of Mexico narrow-azimuth data set provided by ExxonMobil. The velocity model, shown in Figure 5.11, consists of typical sediment-controlled  $v(\xi_3)$  velocity structure, save for the salt body intruding in the center of the block, and offset associated with throw along the dipping fault plane observable in Figure 5.11. By agreement with ExxonMobil, the depths shown in all figures differ from the true values. Key imaging targets in this model include the steep salt flanks around the salt

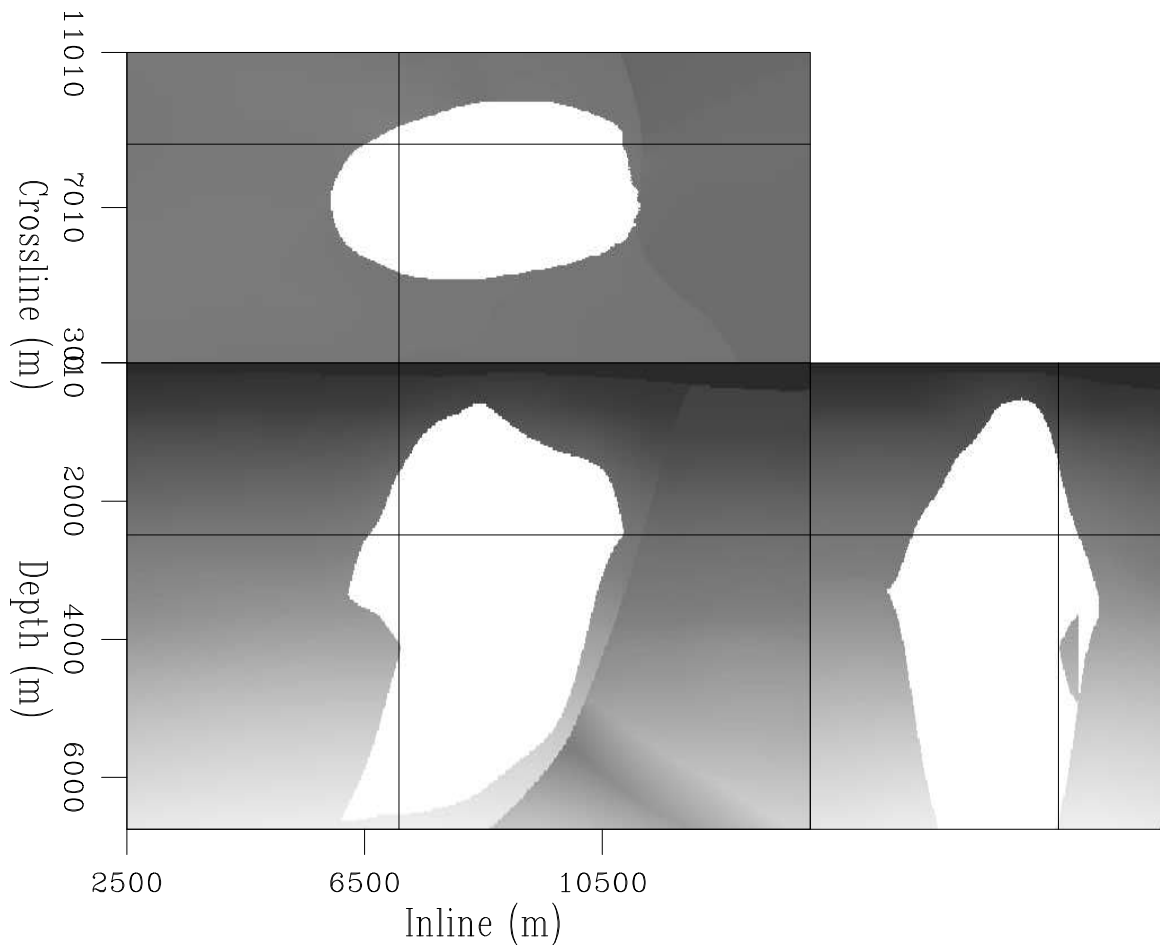


Figure 5.11: Velocity model example for Gulf of Mexico field data set. **ER**  
 conical/. XOM-VEL

Source Parameter	Value	Receiver Parameter	Value
Number of sail lines	54	Max. inline offset (m)	$\pm 3725$
Sail line interval (m)	160	Max. crossline offset (m)	$\pm 500$
Shots per sail line	300	Inline receiver interval (m)	25
Shot interval (m)	50	Crossline receiver interval (m)	80

Table 5.4: Approximate acquisition parameters associated with the 3D Gulf of Mexico field data set.

structure and the overlapping sediments. Previous imaging work in this area indicates that the sediments surrounding the salt body exhibit moderate-to-strong degrees of anisotropy. [?](#) estimated the vertical velocity and anisotropy parameters (assuming VTI media) using a joint inversion technique that combined surface seismic and borehole constraints. [?](#), using a 3D tilted Cartesian coordinate plane-wave migration algorithm for transversely isotropic (TTI) media, demonstrated that accounting for anisotropy greatly improves migrated image quality for this data set.

The migration strategy presented herein differs from that in [?](#) in a number of respects. First, I perform migration using only isotropic sediment flood velocity model. Second, I use a multi-streamer data set for imaging, rather than the more optimally regularized single-streamer data formed through azimuthal move-out preprocessing ([?](#)).

Table 5.4 summarizes the acquisition geometry of the data set. The data used for migration consisted of 54 sail lines separated roughly 160 m apart, each sail line consists of approximately 300 shots acquired every 50 m. I binned the sources in 25 m and 80 m intervals in the inline and crossline, respectively. Figure 5.12 shows the source distribution, and illustrates the sail line direction, herein chosen to be the inline direction. Figure 5.13 shows the chosen offset distribution. The receiver points fall to both positive and negative offsets, as the sail lines were acquired in two directions. The gap in offset coverage between offsets of  $\pm 2500$ - $2750$  m arises due to a corrupted data tape. Receivers were binned at 25 m in both the inline and crossline directions.

Figure 5.12: Chosen source distribution for the field data set. **CR**  
conical/. XOM-SRC

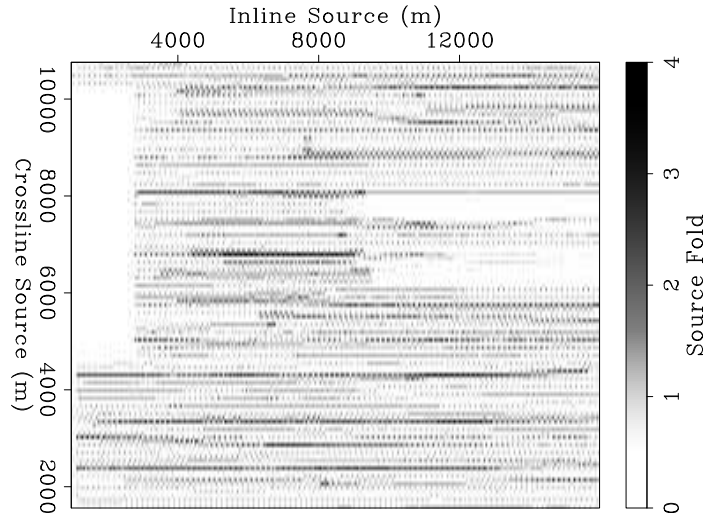
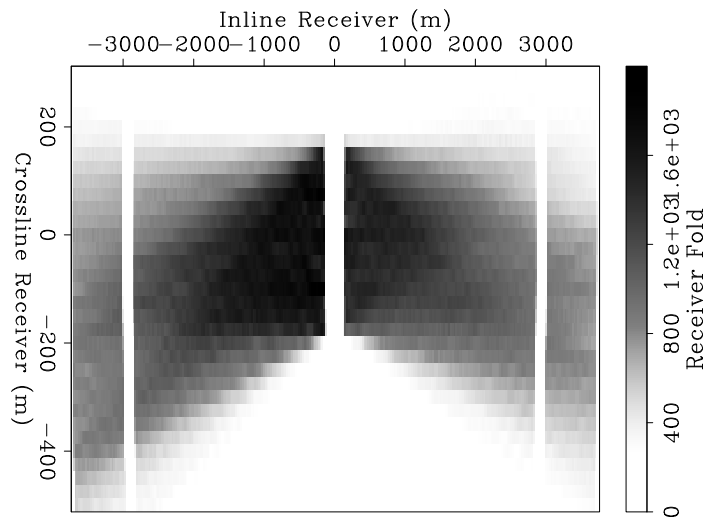


Figure 5.13: Chosen receiver distribution for the field data set. The missing data between offsets  $\pm 2500$ - $2750$  m is due to a corrupted data tape. **CR**  
conical/. XOM-RCV



I prepared the data for migration by applying an inline delay-shot phase-encoding algorithm according to the inline source position. A total of 54 plane-wave sub-volumes were generated from the total 5D shot record volume, each consisting of 41 plane-waves equally sampled between  $\pm 20^\circ$ . I chose a total of 244 frequencies between 3 Hz and 25 Hz for migration. The data were imaged on migration grids with dimensions of 800x350x300 samples. Migrations in TEC coordinates were performed using tilt angles between  $\pm 20^\circ$  at  $1^\circ$  increments, where the tilt angle was matched with the same plane-wave take-off slowness.

Figures 5.14-5.16 present comparative slices from the 3D Gulf of Mexico migration images computed in the TEC and Cartesian coordinate systems. Figure 5.14 presents an inline section taken at the constant 8750 m crossline coordinate for the TEC (top panel) and CC (bottom panel) images corresponding to the front face of Figure 5.11. The top of salt body is well-imaged in both images; however, the near-vertical salt-flanks to the right are nearly entirely absent. Oval A shows the imaging improvements in TEC coordinates for the left-hand flank. Figure 5.15 presents crossline sections for the TEC (top panel) and CC (bottom panel) images. Both images are subject to fair amounts of near-surface aliasing a sali line contribution every 160 m in the crossline direction, as well as the artifacts due to using a non-regularized data set with locations where no data are present. The outlines of the salt body reflector, though, are imaged. Oval A shows an example of an area where the TEC coordinate image is better than the Cartesian image.

Figure 5.16 presents a depth slice extracted from the TEC (top panel) and CC (bottom panel) image volumes. The annular ring, showing the location of the salt body, is apparent in both images; however, the image is sharper in the TEC image indicating improved focussing of energy. Oval A shows an example of an area where the TEC image is better than that generated in Cartesian, including two parts of the right-hand salt flank. Oval B shows the TEC coordinate image improvements in the crossline direction.

The results of the 3D field data application likely could have been improved in a number of aspects. First, a migration velocity model incorporating anisotropy

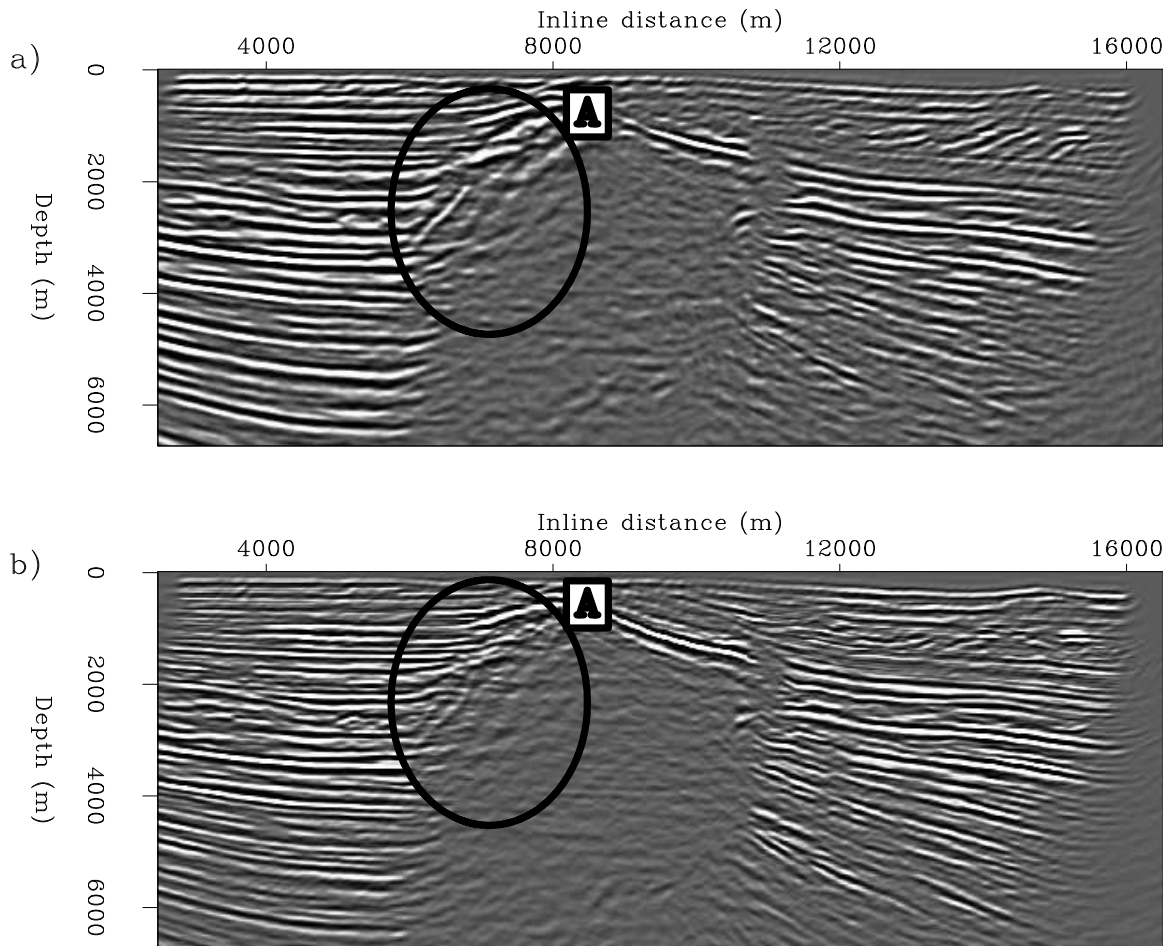


Figure 5.14: Inline sections through the migration images taken at the 8750 m crossline coordinate location. Top: TEC coordinate migration results. Bottom: Cartesian coordinate migration results. Oval A shows the imaging improvements in TEC coordinates for the left-hand flank. **CR** `conical/. RFIG1`

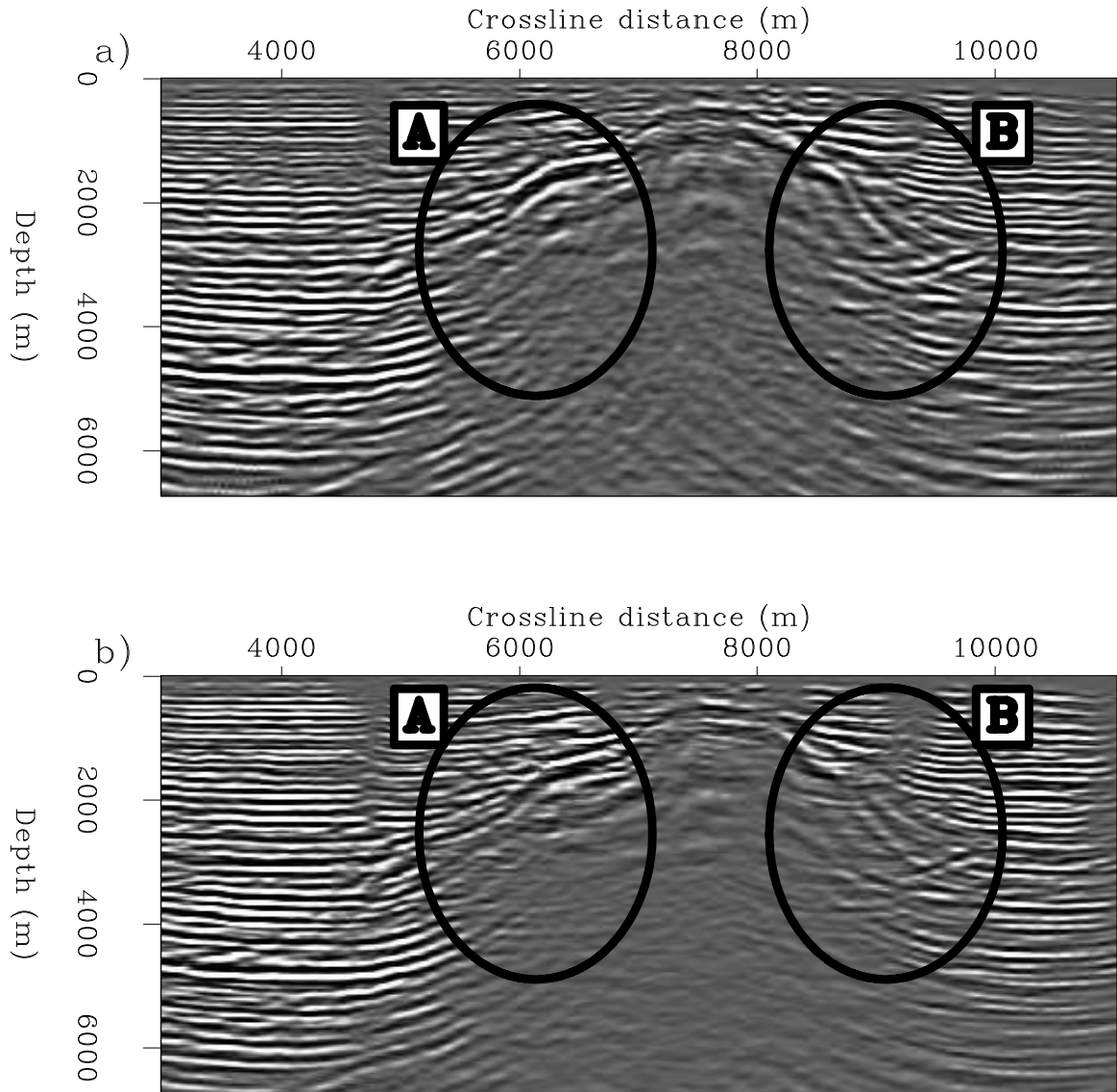


Figure 5.15: Crossline sections through the migration images taken at the 7100 m crossline coordinate location. Top: TEC coordinate migration results. Bottom: Cartesian coordinate migration results. Oval A shows an example of an area where the TEC coordinate image is better than the Cartesian image. CR conical/. RFIG3

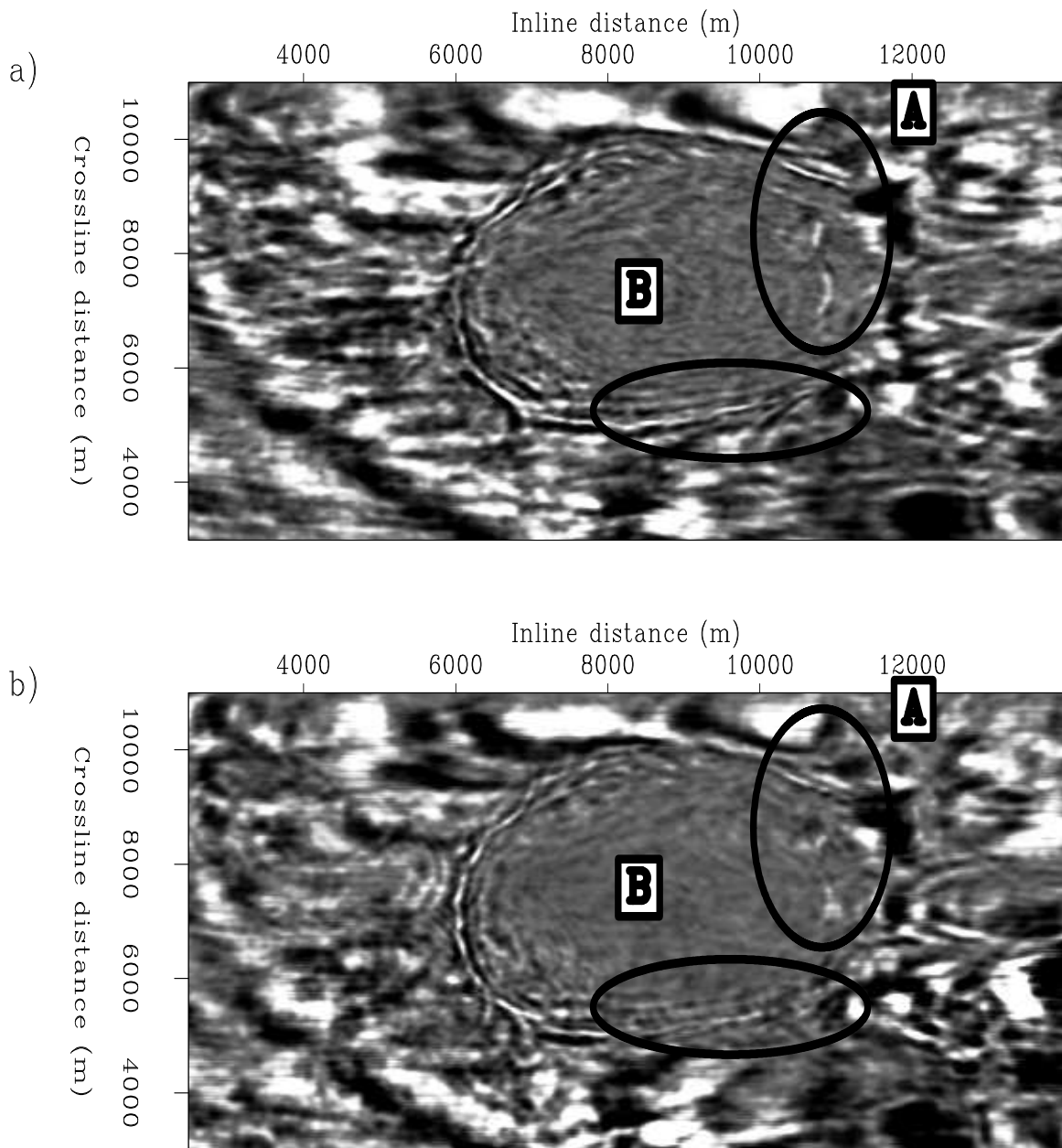


Figure 5.16: Migration results for the 3D Gulf of Mexico field data set through the sedimentary section. Top: TEC coordinate migration results. Bottom: Cartesian coordinate migration results. Oval A shows an example of an area where the TEC image is better than that generated in Cartesian, including two parts of the right-hand salt flank. Oval B shows the TEC coordinate image improvements in the crossline direction. **CR** conical/. RFIG5

information to emphasize horizontal wave propagation could have been used instead of the isotropic velocity profile. Although this would affect the vertical location of the flat-lying sedimentary reflectors, it likely would have led to more accurate horizontal propagation and imaging of waves reflecting off the target salt flanks. Second, if additional computational resources were made available, migrating the full data set (i.e. every 80 m in crossline source position rather than every 160 m) with a higher frequency content would have led to a more infilled and higher resolution image. Third, extending the generalized RWE theory to incorporate TTI anisotropy likely would have enabled a more consistent imaging of the steep salt flanks. This extension is likely to be a subject for future research.

## CONCLUSIONS

This chapter discusses an inline delayed-shot migration technique in tilted elliptical-cylindrical coordinates. I argue that migration approach, relative to the full 3D plane-wave technique, offers both lower memory requirements (due to small migration aperture), as well as a potential reduction in the number of total migrations needed (by migrating fewer sail lines than crossline plane waves). I demonstrate that the impulse response of inline-source delayed-shot wavefields are well-matched to TEC geometry, and that corresponding extrapolation wavenumber is no more complicated than that of elliptically anisotropic media. This leads to an accurate 3D finite-difference splitting algorithm that both accurately propagates wavefields and handles the associated numerical anisotropy. The 3D synthetic Gulf of Mexico data tests demonstrate the migration technique's ability to generate improved images of steeply dipping structure, relative to Cartesian coordinate migration, at reduced computational cost. Field data tests illustrate the utility of the 3D migration approach in exploration practice.

## ACKNOWLEDGMENTS

I thank Biondi Biondi, Bob Clapp, Alejandro Valenciano, Ben Witten, and Bill Curry for helpful conversations. John Etgen is greatly thanked for donating his wisdom and time on the BP research computer cluster, where the 3D synthetic imaging results were generated. I acknowledge BP for the release of the synthetic data set, and ExxonMobil for releasing the field data set.

# Appendix A

## Riemannian geometry overview

Geometry in a generalized 3D Riemannian space is described by a symmetric metric tensor,  $g_{jk} = g_{kj}$ , that relates the geometry in a general non-orthogonal coordinate system,  $\boldsymbol{\xi} = [\xi_1, \xi_2, \xi_3]$ , to an underlying Cartesian mesh,  $\boldsymbol{x} = [x_1, x_2, x_3]$  (?). In matrix form, the metric tensor is written,

$$[g_{jk}] = \begin{bmatrix} g_{11} & g_{12} & g_{13} \\ g_{21} & g_{22} & g_{23} \\ g_{31} & g_{32} & g_{33} \end{bmatrix} \quad (\text{A.1})$$

where  $g_{11}$ ,  $g_{12}$ ,  $g_{22}$ ,  $g_{13}$ ,  $g_{23}$ , and  $g_{33}$  are functions linking the two coordinate systems through,

$$\begin{aligned} g_{11} &= \frac{\partial x_k}{\partial \xi_1} \frac{\partial x_k}{\partial \xi_1}, & g_{12} &= \frac{\partial x_k}{\partial \xi_1} \frac{\partial x_k}{\partial \xi_2}, & g_{22} &= \frac{\partial x_k}{\partial \xi_2} \frac{\partial x_k}{\partial \xi_2}, \\ g_{13} &= \frac{\partial x_k}{\partial \xi_1} \frac{\partial x_k}{\partial \xi_3}, & g_{23} &= \frac{\partial x_k}{\partial \xi_2} \frac{\partial x_k}{\partial \xi_3}, & g_{33} &= \frac{\partial x_k}{\partial \xi_3} \frac{\partial x_k}{\partial \xi_3}. \end{aligned} \quad (\text{A.2})$$

The associated (or inverse) metric tensor,  $g^{jk}$ , is given by,

$$[g^{jk}] = \frac{1}{|\mathbf{g}|} \begin{bmatrix} g_{22}g_{33} - g_{23}^2 & g_{13}g_{23} - g_{12}g_{33} & g_{12}g_{23} - g_{13}g_{22} \\ g_{13}g_{23} - g_{12}g_{33} & g_{11}g_{33} - g_{13}^2 & g_{12}g_{13} - g_{11}g_{23} \\ g_{12}g_{23} - g_{13}g_{22} & g_{12}g_{13} - g_{11}g_{23} & g_{11}g_{22} - g_{12}^2 \end{bmatrix}, \quad (\text{A.3})$$

and has the following metric discriminant,  $|\mathbf{g}|$ ,

$$|\mathbf{g}| = g_{11}g_{22}g_{33} - g_{12}^2g_{33} - g_{23}^2g_{11} - g_{13}^2g_{22} + 2g_{12}g_{13}g_{23}. \quad (\text{A.4})$$

A weighted metric tensor,  $m^{jk} = \sqrt{|\mathbf{g}|} g^{jk}$ , is also used throughout the thesis.

# Appendix B

## Generalized phase-shift operators

This appendix specifies a phase-shift approximation to the extrapolation wavenumber used to propagate wavefields described in equation 2.9. The relationship between the extrapolation wavenumber  $k_{\xi_3}$ , the two other wavenumbers  $k_{\xi_1}$  and  $k_{\xi_2}$ , and the geometry variables is given by

$$k_{\xi_3} = -a_1 k_{\xi_1} - a_2 k_{\xi_2} + ia_3 \pm [a_4^2 \omega^2 - a_5^2 k_{\xi_1}^2 - a_6^2 k_{\xi_2}^2 - a_7 k_{\xi_1} k_{\xi_2} + ia_8 k_{\xi_1} + ia_9 k_{\xi_2} - a_{10}^2]^{\frac{1}{2}}, \quad (\text{B.1})$$

where the non-stationary coefficients,  $a_j$  in equation B.1, are presented in vector  $\mathbf{a}$ ,

$$\mathbf{a} = \begin{bmatrix} \frac{m^{13}}{m^{33}} & \frac{m^{23}}{m^{33}} & \frac{n^3}{2m^{33}} & \frac{\sqrt{|\mathbf{g}|^s}}{\sqrt{m^{33}}} & \sqrt{\frac{m^{11}}{m^{33}} - \left(\frac{m^{13}}{m^{33}}\right)^2} & \sqrt{\frac{m^{22}}{m^{33}} - \left(\frac{m^{23}}{m^{33}}\right)^2} & \dots \\ \dots & \left[ \frac{2m^{12}}{m^{33}} - \frac{2m^{13}m^{23}}{(m^{33})^2} \right] & \left[ \frac{n^1}{m^{33}} - \frac{m^{13}n^3}{(m^{33})^2} \right] & \left[ \frac{n^2}{m^{33}} - \frac{m^{23}n^3}{(m^{33})^2} \right] & \frac{n^3}{2m^{33}} \end{bmatrix}^{\mathbf{T}}. \quad (\text{B.2})$$

The extrapolation wavenumber defined in equations B.1 and B.2 generally cannot be implemented exactly in the Fourier domain due to a simultaneous spatial dependence (i.e. a function of both  $\boldsymbol{\xi}$  and  $\mathbf{k}_{\boldsymbol{\xi}}$ ). This can be addressed using a multi-coefficient version of the split-step Fourier approximation (?) that uses Taylor expansions to separate  $k_{\xi_3}$  into two parts:  $k_{\xi_3} \approx k_{\xi_3}^{PS} + k_{\xi_3}^{SSF}$ . Wavenumbers  $k_{\xi_3}^{PS}$  and  $k_{\xi_3}^{SSF}$  represent a pure Fourier ( $\omega - \mathbf{k}_{\boldsymbol{\xi}}$ ) domain phase-shift and a mixed ( $\omega - \boldsymbol{\xi}$ ) domain split-step

correction, respectively.

The phase-shift term is given by,

$$k_{\xi_3}^{PS} = -b_1 k_{\xi_1} - b_2 k_{\xi_2} + i b_3 \pm [b_4^2 \omega^2 - b_5^2 k_{\xi_1}^2 - b_6^2 k_{\xi_2}^2 - b_7 k_{\xi_1} k_{\xi_2} + i b_8 k_{\xi_1} + i b_9 k_{\xi_2} - b_{10}^2]^{\frac{1}{2}}, \quad (\text{B.3})$$

where  $b_j = b_j(\xi_3)$  are reference values of  $a_j = a_j(\xi_1, \xi_2, \xi_3)$ . The split-step approximation is developed by performing a Taylor expansion about each coefficient  $a_j$  and evaluating the results at stationary reference values  $b_j$ . Assuming that the stationary values of  $k_{\xi_1}$  and  $k_{\xi_2}$  are zero, the split-step correction is as follows,

$$k_{\xi_3}^{SSF} = \left. \frac{\partial k_{\xi_3}}{\partial a_3} \right|_0 (a_3 - b_3) + \left. \frac{\partial k_{\xi_3}}{\partial a_4} \right|_0 (a_4 - b_4) + \left. \frac{\partial k_{\xi_3}}{\partial a_{10}} \right|_0 (a_{10} - b_{10}), \quad (\text{B.4})$$

where “0” denotes “with respect to a reference medium”. The partial differential expressions in equation B.4 are,

$$\left. \frac{\partial k_{\xi_3}}{\partial a_3} \right|_0 = b_3, \quad \left. \frac{\partial k_{\xi_3}}{\partial a_4} \right|_0 = \frac{b_4 \omega^2}{\sqrt{b_4^2 \omega^2 - b_{10}^2}}, \quad \left. \frac{\partial k_{\xi_3}}{\partial a_{10}} \right|_0 = -\frac{b_{10}}{\sqrt{b_{10}^2 \omega^2 - b_{10}^2}}, \quad (\text{B.5})$$

resulting in the following split-step Fourier correction wavenumber,

$$k_{\xi_3}^{SSF} = i b_3 (a_3 - b_3) + \frac{b_4 \omega^2 (a_4 - b_4)}{\sqrt{b_4^2 \omega^2 - b_{10}^2}} - \frac{b_{10} (a_{10} - b_{10})}{\sqrt{b_{10}^2 \omega^2 - b_{10}^2}}. \quad (\text{B.6})$$

# Appendix C

## RWE wavenumber approximations

The extrapolation wavenumber developed in equation 2.9 is appropriate for any non-orthogonal Riemannian geometry. However, there are a number of situations where symmetry or partial orthogonality are present. Moreover, kinematic approximations can be made where one ignores all imaginary wavenumber components. These situations are discussed herein.

**3D Semi-orthogonal coordinate systems** - Semi-orthogonal coordinate systems occur where one coordinate ( $\xi_3$ ) is orthogonal to the other two coordinates ( $\xi_1$  and  $\xi_2$ ) (?). In these cases the  $m^{13}$  and  $m^{23}$  components of the weighted metric tensor are identically zero, which leads to the following extrapolation wavenumber,

$$k_{\xi_3} = ia_3 \pm [a_4^2 \omega^2 - a_5^2 k_{\xi_1}^2 - a_6^2 k_{\xi_2}^2 - a_7 k_{\xi_1} k_{\xi_2} + ia_8 k_{\xi_1} + ia_9 k_{\xi_2} - a_{10}^2]^{\frac{1}{2}}, \quad (\text{C.1})$$

where,

$$\mathbf{a} = \left[ 0 \quad 0 \quad \frac{n^3}{2m^{33}} \quad \frac{\sqrt{|\mathbf{g}|_s}}{\sqrt{m^{33}}} \quad \sqrt{\frac{m^{11}}{m^{33}}} \quad \sqrt{\frac{m^{22}}{m^{33}}} \quad \frac{2m^{12}}{m^{33}} \quad \frac{n^1}{m^{33}} \quad \frac{n^2}{m^{33}} \quad \frac{n^3}{2m^{33}} \right]^{\mathbf{T}}. \quad (\text{C.2})$$

which are identical to the coefficients recovered by ?.

**3D kinematic coordinate systems** - One approximation that reduces the computational and memory costs is to consider any term in equation 2.9 with an imaginary

number to be purely an amplitude factor. (Note that this is not purely correct because the square root of an imaginary number generally has a real component.) This 'kinematic approximation' leads to extrapolation wavenumber,

$$\hat{k}_{\xi_3} = -a_1 k_{\xi_1} - a_2 k_{\xi_2} \pm [a_4^2 \omega^2 - a_5^2 k_{\xi_1}^2 - a_6^2 k_{\xi_2}^2 - a_7 k_{\xi_1} k_{\xi_2} - a_{10}^2]^{\frac{1}{2}}, \quad (\text{C.3})$$

where,

$$\mathbf{a} = \left[ \frac{m^{13}}{m^{33}} \quad \frac{m^{23}}{m^{33}} \quad 0 \quad \frac{\sqrt{|\mathbf{g}|}s}{\sqrt{m^{33}}} \quad \sqrt{\frac{m^{11}}{m^{33}} - \left(\frac{m^{13}}{m^{33}}\right)^2} \quad \sqrt{\frac{m^{22}}{m^{33}} - \left(\frac{m^{23}}{m^{33}}\right)^2} \quad \frac{2m^{12}}{m^{33}} - \frac{2m^{13}m^{23}}{(m^{33})^2} \quad 0 \quad 0 \quad \frac{n^3}{2m^{33}} \right]^{\mathbf{T}}. \quad (\text{C.4})$$

**3D kinematic semi-orthogonal coordinate systems** - Combining the two above restrictions yields the following extrapolation wavenumber,

$$\hat{k}_{\xi_3} = \pm [a_4^2 \omega^2 - a_5^2 k_{\xi_1}^2 - a_6^2 k_{\xi_2}^2 - a_7 k_{\xi_1} k_{\xi_2} - a_{10}^2]^{\frac{1}{2}}, \quad (\text{C.5})$$

where,

$$\mathbf{a} = \left[ 0 \quad 0 \quad 0 \quad \frac{\sqrt{|\mathbf{g}|}s}{\sqrt{m^{33}}} \quad \sqrt{\frac{m^{11}}{m^{33}}} \quad \sqrt{\frac{m^{22}}{m^{33}}} \quad \frac{2m^{12}}{m^{33}} \quad 0 \quad 0 \quad \frac{n^3}{2m^{33}} \right]^{\mathbf{T}}. \quad (\text{C.6})$$

**2D non-orthogonal coordinate systems** - Two-dimensional situations are handled by identifying  $\xi_2 = 0$ . All derivatives in the associated metric tensor  $m^{jk}$  with respect coordinate  $\xi_2$  are identically zero, and the resulting 2D non-orthogonal coordinate system wavenumber is,

$$k_{\xi_3} = -a_1 k_{\xi_1} + ia_3 \pm [a_4^2 \omega^2 - a_5^2 k_{\xi_1}^2 + ia_8 k_{\xi_1} - a_{10}^2]^{\frac{1}{2}}, \quad (\text{C.7})$$

where,

$$\mathbf{a} = \left[ \frac{m^{13}}{m^{33}} \quad 0 \quad \frac{n^3}{2m^{33}} \quad \frac{\sqrt{|\mathbf{g}|}s}{\sqrt{m^{33}}} \quad \sqrt{\frac{m^{11}}{m^{33}} - \left(\frac{m^{13}}{m^{33}}\right)^2} \quad 0 \quad 0 \quad \frac{n^1}{m^{33}} - \frac{m^{13}n^3}{(m^{33})^2} \quad 0 \quad \frac{n^3}{2m^{33}} \right]^{\mathbf{T}}. \quad (\text{C.8})$$

**2D non-orthogonal kinematic coordinate systems** - Two-dimensional kinematic situations are handled through identity  $\xi_2 = 0$ . Again, all derivatives in the associated metric tensor  $m^{jk}$  with respect coordinate  $\xi_2$  are identically zero, and the 2D non-orthogonal kinematic extrapolation wavenumber is

$$\hat{k}_{\xi_3} = -a_1 k_{\xi_1} \pm [a_4^2 \omega^2 - a_5^2 k_{\xi_1}^2 - a_{10}^2]^{\frac{1}{2}}, \quad (\text{C.9})$$

where,

$$\mathbf{a} = \begin{bmatrix} \frac{m^{13}}{m^{33}} & 0 & 0 & \frac{\sqrt{|\mathbf{g}|_s}}{\sqrt{m^{33}}} & \sqrt{\frac{m^{11}}{m^{33}} - \left(\frac{m^{13}}{m^{33}}\right)^2} & 0 & 0 & 0 & 0 & \frac{n^3}{2m^{33}} \end{bmatrix}^{\mathbf{T}}. \quad (\text{C.10})$$

**2D orthogonal coordinate systems** - Two-dimensional situations are handled with  $\xi_2 = g_{13} = 0$ . Accordingly, all derivatives in the associated metric tensor  $m^{jk}$  with respect coordinate  $\xi_2$  are identically zero, and the 2D orthogonal coordinate system is represented by

$$k_{\xi_3} = ia_3 \pm [a_4^2 \omega^2 - a_5^2 k_{\xi_1}^2 + ia_8 k_{\xi_1} - a_{10}^2]^{\frac{1}{2}}, \quad (\text{C.11})$$

where,

$$\mathbf{a} = \begin{bmatrix} 0 & 0 & \frac{n_3}{2m^{33}} & \frac{\sqrt{|\mathbf{g}|_s}}{\sqrt{m^{33}}} & \sqrt{\frac{m^{11}}{m^{33}}} & 0 & 0 & \frac{n^1}{m^{33}} & 0 & \frac{n^3}{2m^{33}} \end{bmatrix}^{\mathbf{T}}. \quad (\text{C.12})$$

**2D orthogonal kinematic coordinate systems** - The above two approximations can be combined to yield the following extrapolation wavenumber for 2D orthogonal kinematic coordinate systems,

$$\hat{k}_{\xi_3} = \pm [a_4^2 \omega^2 - a_5^2 k_{\xi_1}^2 - a_{10}^2]^{\frac{1}{2}}, \quad (\text{C.13})$$

where,

$$\mathbf{a} = \begin{bmatrix} 0 & 0 & 0 & \frac{\sqrt{|\mathbf{g}|_s}}{\sqrt{m^{33}}} & \sqrt{\frac{m^{11}}{m^{33}}} & 0 & 0 & 0 & 0 & \frac{n^3}{2m^{33}} \end{bmatrix}^{\mathbf{T}}. \quad (\text{C.14})$$

# Appendix D

## Elliptic coordinate systems

Exploring constant coordinate surfaces provides additional insight into some characteristics of the elliptic coordinate system. As illustrated by the following trigonometric identities, curves of constant  $\xi_1$  represent hyperbolas

$$\frac{x_1^2}{a^2 \cos^2 \xi_1} - \frac{x_3^2}{a^2 \sin^2 \xi_1} = \cosh^2 \xi_3 - \sinh^2 \xi_3 = 1, \quad (\text{D.1})$$

while curves of constant  $\xi_3$  form ellipses

$$\frac{x_1^2}{a^2 \cosh^2 \xi_3} + \frac{x_3^2}{a^2 \sinh^2 \xi_3} = \cos^2 \xi_1 + \sin^2 \xi_1 = 1. \quad (\text{D.2})$$

Thus, outward extrapolation in the  $\xi_3$  direction would step a wavefield through a family of elliptic surfaces defined by equation D.2.

Equation D.1 may also be used to derive an expression that defines the local extrapolation axis angle,  $\theta(\boldsymbol{\xi})$ , relative to vertical reference. Taking the total derivative of equation D.1,

$$\frac{2 x_1 dx_1}{a^2 \cosh^2 \xi_3} + \frac{2 x_3 dx_3}{a^2 \sinh^2 \xi_3} = 0, \quad (\text{D.3})$$

and further manipulating the result yields the local extrapolation axis angle  $\theta(\boldsymbol{\xi})$

$$\tan \theta = \frac{dx_1}{dx_3} = \frac{x_3 \cos^2 \xi_1}{x_1 \sin^2 \xi_1} = \tanh \xi_3 \cot \xi_1. \quad (\text{D.4})$$

# Appendix E

## ADCIG coordinate transform

This appendix addresses how to express operators  $\frac{\partial}{\partial x_3}$  and  $\frac{\partial}{\partial h_{x_1}}$  in generalized coordinate systems to derive equation 4.10. I first assume that generalized coordinate systems are related to the Cartesian variables through a bijection (i.e., one-to-one mapping)

$$x_1 = f(\xi_1, \xi_3) \quad \text{and} \quad x_3 = g(\xi_1, \xi_3) \quad (\text{E.1})$$

with a non-vanishing Jacobian of coordinate transformation,  $J_{\xi}$ . The bijection between a generalized and Cartesian coordinate system allows us to rewrite the left-hand-sides of equations 4.7 as (?)

$$\frac{\partial t}{\partial x_1} = \frac{1}{J_{\xi}} \frac{\partial(t, x_3)}{\partial(\xi_1, \xi_3)} \quad \text{and} \quad \frac{\partial t}{\partial x_3} = \frac{1}{J_{\xi}} \frac{\partial(x_1, t)}{\partial(\xi_1, \xi_3)}. \quad (\text{E.2})$$

Expanding the Jacobian notation leads to

$$\left[ \begin{array}{c} \frac{\partial t}{\partial \xi_1} \frac{\partial x_3}{\partial \xi_3} - \frac{\partial t}{\partial \xi_3} \frac{\partial x_3}{\partial \xi_1} \\ \frac{\partial t}{\partial \xi_3} \frac{\partial x_1}{\partial \xi_1} - \frac{\partial t}{\partial \xi_1} \frac{\partial x_1}{\partial \xi_3} \end{array} \right] = 2 J_{\xi} s \cos \gamma \left[ \begin{array}{c} \sin \alpha \\ \cos \alpha \end{array} \right]. \quad (\text{E.3})$$

The right-hand-sides of equations E.3 are analogous to those derived by ?. Cross-multiplying the expressions by factors  $\frac{\partial x_1}{\partial \xi_3}$  and  $\frac{\partial x_3}{\partial \xi_3}$

$$\begin{bmatrix} \frac{\partial x_1}{\partial \xi_3} \left( \frac{\partial t}{\partial \xi_1} \frac{\partial x_3}{\partial \xi_3} - \frac{\partial t}{\partial \xi_3} \frac{\partial x_3}{\partial \xi_1} \right) \\ \frac{\partial x_3}{\partial \xi_3} \left( \frac{\partial t}{\partial \xi_3} \frac{\partial x_1}{\partial \xi_1} - \frac{\partial t}{\partial \xi_1} \frac{\partial x_1}{\partial \xi_3} \right) \end{bmatrix} = 2 J_{\boldsymbol{\xi}} s \cos \gamma \begin{bmatrix} \frac{\partial x_1}{\partial \xi_3} \sin \alpha \\ \frac{\partial x_3}{\partial \xi_3} \cos \alpha \end{bmatrix} \quad (\text{E.4})$$

and adding the two expressions results in

$$\frac{\partial t}{\partial \xi_3} \left( \frac{\partial x_3}{\partial \xi_3} \frac{\partial x_1}{\partial \xi_1} - \frac{\partial x_1}{\partial \xi_3} \frac{\partial x_3}{\partial \xi_1} \right) = 2 J_{\boldsymbol{\xi}} s \cos \gamma \left( \frac{\partial x_1}{\partial \xi_3} \sin \alpha + \frac{\partial x_3}{\partial \xi_3} \cos \alpha \right). \quad (\text{E.5})$$

A similar argument can be used to construct the equations for the subsurface-offset axis. The bijection between the generalized coordinate and Cartesian subsurface-offset axes allows for the left-hand-side of equations 4.7 to be rewritten as

$$\frac{\partial t}{\partial h_{x_1}} = \frac{1}{J_{\mathbf{h}}} \frac{\partial(t, h_{x_3})}{\partial(h_{\xi_1}, h_{\xi_3})} \quad \text{and} \quad \frac{\partial t}{\partial h_{x_3}} = \frac{1}{J_{\mathbf{h}}} \frac{\partial(h_{x_1}, t)}{\partial(h_{\xi_1}, h_{\xi_3})}, \quad (\text{E.6})$$

where  $J_{\mathbf{h}}$  is the subsurface-offset Jacobian of transformation. Expanding the Jacobian notation leads to

$$\begin{bmatrix} \frac{\partial t}{\partial h_{\xi_1}} \frac{\partial h_{x_3}}{\partial h_{\xi_3}} - \frac{\partial t}{\partial h_{\xi_3}} \frac{\partial h_{x_3}}{\partial h_{\xi_1}} \\ \frac{\partial t}{\partial h_{\xi_3}} \frac{\partial h_{x_1}}{\partial h_{\xi_1}} - \frac{\partial t}{\partial h_{\xi_1}} \frac{\partial h_{x_1}}{\partial h_{\xi_3}} \end{bmatrix} = 2 J_{\mathbf{h}} s \sin \gamma \begin{bmatrix} \cos \alpha \\ \sin \alpha \end{bmatrix}. \quad (\text{E.7})$$

The right-hand-side of equations E.7 are again analogous to those given by ?. Cross-multiplying the expressions by factors  $\frac{\partial h_{x_1}}{\partial h_{\xi_1}}$  and  $\frac{\partial h_{x_3}}{\partial h_{\xi_1}}$

$$\begin{bmatrix} \frac{\partial h_{x_1}}{\partial h_{\xi_1}} \left( \frac{\partial t}{\partial h_{\xi_1}} \frac{\partial h_{x_3}}{\partial h_{\xi_3}} - \frac{\partial t}{\partial h_{\xi_3}} \frac{\partial h_{x_3}}{\partial h_{\xi_1}} \right) \\ \frac{\partial h_{x_3}}{\partial h_{\xi_1}} \left( \frac{\partial t}{\partial h_{\xi_3}} \frac{\partial h_{x_1}}{\partial h_{\xi_1}} - \frac{\partial t}{\partial h_{\xi_1}} \frac{\partial h_{x_1}}{\partial h_{\xi_3}} \right) \end{bmatrix} = 2 J_{\mathbf{h}} s \sin \gamma \begin{bmatrix} \frac{\partial h_{x_1}}{\partial h_{\xi_1}} \cos \alpha \\ \frac{\partial h_{x_3}}{\partial h_{\xi_1}} \sin \alpha \end{bmatrix}, \quad (\text{E.8})$$

and subtracting the two expressions above yields

$$\frac{\partial t}{\partial h_{\xi_1}} \left( \frac{\partial h_{x_1}}{\partial h_{\xi_1}} \frac{\partial h_{x_3}}{\partial h_{\xi_3}} - \frac{\partial h_{x_1}}{\partial h_{\xi_3}} \frac{\partial h_{x_3}}{\partial h_{\xi_1}} \right) = 2 J_{\mathbf{h}} s \sin \gamma \left( \frac{\partial h_{x_1}}{\partial h_{\xi_1}} \cos \alpha - \frac{\partial h_{x_3}}{\partial h_{\xi_1}} \sin \alpha \right). \quad (\text{E.9})$$

An expression for ADCIGs can be obtained by dividing equation E.9 by equation E.5

$$\frac{\frac{\partial t}{\partial h_{\xi_1}} \left( \frac{\partial h_{x_1}}{\partial h_{\xi_1}} \frac{\partial h_{x_3}}{\partial h_{\xi_3}} - \frac{\partial h_{x_1}}{\partial h_{\xi_3}} \frac{\partial h_{x_3}}{\partial h_{\xi_1}} \right)}{\frac{\partial t}{\partial \xi_3} \left( \frac{\partial x_3}{\partial \xi_3} \frac{\partial x_1}{\partial \xi_1} - \frac{\partial x_1}{\partial \xi_3} \frac{\partial x_3}{\partial \xi_1} \right)} = \tan \gamma \frac{J_{\mathbf{h}} \left( \frac{\partial h_{x_1}}{\partial h_{\xi_1}} \cos \alpha - \frac{\partial h_{x_3}}{\partial h_{\xi_1}} \sin \alpha \right)}{J_{\boldsymbol{\xi}} \left( \frac{\partial x_3}{\partial \xi_3} \cos \alpha + \frac{\partial x_1}{\partial \xi_3} \sin \alpha \right)}. \quad (\text{E.10})$$

One question arising from the geometric factors in equation E.10 is what do the terms  $\frac{\partial h_{x_1}}{\partial h_{\xi_1}}$ ,  $\frac{\partial h_{x_3}}{\partial h_{\xi_1}}$ ,  $\frac{\partial h_{x_1}}{\partial h_{\xi_3}}$  and  $\frac{\partial h_{x_3}}{\partial h_{\xi_3}}$  represent? I assume that the subsurface offset axes are generated by uniform wavefield shifting such that the following equations are valid:

$$\begin{bmatrix} h_{x_1} \\ h_{x_3} \\ h_{\xi_1} \\ h_{\xi_1} \end{bmatrix} = \begin{bmatrix} x_1 \\ x_3 \\ \xi_1 \\ \xi_3 \end{bmatrix} \quad \text{such that} \quad \begin{bmatrix} \frac{\partial h_{x_1}}{\partial h_{\xi_1}} \\ \frac{\partial h_{x_3}}{\partial h_{\xi_1}} \\ \frac{\partial h_{x_1}}{\partial h_{\xi_3}} \\ \frac{\partial h_{x_3}}{\partial h_{\xi_3}} \end{bmatrix} = \begin{bmatrix} \frac{\partial x_1}{\partial \xi_1} \\ \frac{\partial x_3}{\partial \xi_1} \\ \frac{\partial x_1}{\partial \xi_3} \\ \frac{\partial x_3}{\partial \xi_3} \end{bmatrix}. \quad (\text{E.11})$$

If the subsurface offset axes were generated by anything other than uniform shifting (e.g.  $h_{x_1} = x_1^2$ ), then the assumptions behind equations E.11 would not be honored.

Using these identities in equation E.5 reduces equation E.10 to

$$-\left. \frac{\partial \xi_3}{\partial h_{\xi_1}} \right|_{\xi_1, t} = \frac{\partial t}{\partial h_{\xi_1}} \bigg/ \frac{\partial t}{\partial \xi_3} = \tan \gamma \frac{\left( \frac{\partial x_1}{\partial \xi_1} \cos \alpha - \frac{\partial x_3}{\partial \xi_1} \sin \alpha \right)}{\left( \frac{\partial x_3}{\partial \xi_3} \cos \alpha + \frac{\partial x_1}{\partial \xi_3} \sin \alpha \right)}, \quad (\text{E.12})$$

where the two Jacobian transformations are equivalent (i.e.  $J_{\boldsymbol{\xi}} = J_{\mathbf{h}}$ ). This completes the derivation of equation 4.10.